1-28-2015

GLUCOSE/ OXYGEN-BASED BIOFUEL CELL FOR BIOMEDICAL APPLICATIONS: ELECTRODE DESIGNS INTEGRATING CARBON COMPOSITE

Claudia W. Narvaez Villarrubia

Claudia Wuillma Narváez Villarrubia
Candidate

Department of Chemical and Biological Engineering
Department

This dissertation is approved, and it is acceptable in quality and form for publication:

Approved by the Dissertation Committee:

Plamen B. Atanassov , Chairperson

Andrew P. Shreve

Andrew J. Schuler

Gautam Gupta

Sofia Babanova

GLUCOSE/ OXYGEN-BASED BIOFUEL CELL FOR BIOMEDICAL APPLICATIONS: ELECTRODE DESIGNS INTEGRATING CARBON COMPOSITE NANOMATERIALS

by

CLAUDIA WUILLMA NARVAEZ VILLARRUBIA

M.S. Chemical Engineering, University of New Mexico, 2011
B.S. Chemical Engineering, University of New Mexico, 2009

DISSERTATION

Submitted in Partial Fulfillment of the
Requirements for the Degree of

Doctor of Philosophy
Engineering

The University of New Mexico
Albuquerque, New Mexico
December, 2014

DEDICATION

I dedicated this work to my dear family for giving me the support and inspiration I needed to come this far.

ACKOWLEDGEMENT

I would like to thank my father, Miguel Narváez, for his words of wisdom and encouragement. I would like to thank my mother, Basilica Villarrubia, as well, for being the most caring and giving person I ever met and the woman I admire the most. Both gave me the tools and support I need to achieve my goals and dreams. I would like to thank my little brother, Rubén. He is a true life warrior and thought me to never give up. Also, I would like to thank my older siblings, for the support and life lessons they thought me. I greatly appreciate my each member of my family for their immeasurable love, their encouragement and support.

This work couldn't be possible without the support, guidance and inspiration I received from my adviser, Prof. Plamen Atanassov. I'm enormously thankful for every lesson he gave me, the support I received from him during critical moments in my life, for the opportunity to work and learn from his work and for being engaged with his research group.

I would like to thank the members of my dissertation committee, Prof. Andrew Shreve, Prof. Andrew Schuler, Dr. Gautam Gupta and Prof. Sofia Babanova for their invaluable contribution and their recommendations in the development of this dissertation. My gratitude is extended to the MURI Program for the funding to pursue this research.

Also, I'm very grateful for the collaboration of Dr. Kateryna Artyushkova with the XPS-analysis on the anode design. I would like to thank my coworkers from Prof. Atanassov's lab at the University of New Mexico for their invaluable friendship.

I would like to thank my dear friends for their friendship, for making my days enjoyable even though I'm away from my family, and for giving me a smile every time I share with them.

To Moises and Laetitia, my dear editors, I would like to thank from the bottom of my heart for the time they invested in this work and the support over these last years.

Glucose/Oxygen-Based Biofuel Cell Integrating for Biomedical Applications: Electrodes Designs Integrating Carbon Composite Nanomaterials

by

Claudia Wuillma Narváez Villarrubia
M.S. Chemical Engineering, University of New Mexico, 2011
B.S. Chemical Engineering, University of New Mexico, 2009

ABSTRACT

The relevance of this research is based on the need to develop biofuel cells as an alternative technology for powering implantable and/or extracorporeal medical devices. To accomplish this, processes occurring in nature are mimicked on the surface of bioelectrodes by enzymatic systems. In this research, various 'hot' topics, at different stages of the development of the technology, are revised in order to: accomplish understanding of the principles governing the normal operation of a glucose/O_2 fuel cell, overcome obstacles to advance over the current technological limitations, and propose designs at the nanostructural catalytic layer scale as well as assembly platforms for practical cell operation. This research opens the possibilities to optimize electrode designs based on carbon composite nanomaterials, reagentless enzymatic systems and state-of-the-art enzymatic-stabilization procedures. The design and use of composite nanoarchitectural structures to achieve increased current density generation, cofactor and enzyme stability is a major accomplishment of this research. The technology herein can serve as a departing foundation to engineer electrode designs that meet the criteria required for reagentless biofuel cells for implantable and extracorporeal applications.

TABLE OF CONTENTS

DEDICATION……..…….iv

ACKNOWLEDGEMENTS……..…...v

ABSTRACT……..….vi

LIST OF FIGURES…….…….……xiv

LIST OF TABLES……xxi

Chapter 1 Introduction……..……..…….....1

1.1. Types of Biofuel Cells…….…….....2

1.1.1. Cells-based fuel Cells……..……2

1.1.2. Organelle-Based Fuel Cell…….……..4

1.1.3. Enzyme-based Fuel Cell……..4

1.2. Fuel Cells -Performance…….…….…..6

1.3. Glucose/Oxygen Cell -Performance……..…….…..…12

1.4. Principles and Design Aspects of Enzymatic Fuel Cells……..……...14

1.4.1. Mechanisms of Electron Transfer ……....15

1.4.2. Enzymes……17

1.4.2.1. Enzymatic systems for Bioanode Design……18

1.4.2.2. Enzymatic systems for Biocathode Design……22

1.4.3. Bioelectrodes Materials……...….25

1.4.3.1. Carbon Nanotubes ……..……...….26

1.4.3.2. Toray Paper……..…….……28

1.4.3.3. Nonconductive Bioelectrode Design Materials……..……..….29

1.4.3.4. EFC for Extracorporeal Application-Assembly of Bioelectrodes to Paper-Based 2D-Microfuidic System for Cell Design……..…..…….……..…..30

1.5. EFCs as Power Sources for Biomedical Devices……30

1.6. Statement and Objectives of the Research……...…….…….…..34

Chapter 2. Experimental Methods - Physical and Electrochemical …..…….……...38

2.1. Electrochemical Techniques for Electrodes Characterization……...…….38

2.1.1. Open Circuit Potential…….……....39

2.1.2. Cyclic Voltammetry……..……...……39

2.1.3. Chronoamperometry……..……...…….…..40

2.1.4. Chronopotentiometry……..……...…..…42

2.2. Physical Surface Characterization Techniques …….…...43

2.2.1. Scanning Electron Microscopy (SEM)…….... 43

2.2.2. Energy Disperse Spectroscopy (EDS) ……44

2.2.3. X-Ray Photoelectron Spectroscopy (XPS) ……44

Chapter 3. Biofuel Cell Anodes Integrating NAD^+-Dependent Enzymes and Multi-walled Carbon Nanotube Papers…….……..46

3.1. Introduction……...……46

3.2. Experimental Methods…….……49

3.2.1. Apparatus……..……..49

3.2.2. Chemicals……49

3.2.3. Electrode Design……50

3.2.4. Open Circuit Potential ……..……..50

3.2.5. Cyclic Voltammetry……..……..……51

3.2.6. Michaelis-Menten Analysis…….……...51

3.2.7. Polarization Curves in the Electrolytic Cell ……...……51

3.2.8. Stabilization Study of BEP-MG-GDH Anode……..…..…52

3.3. Results……..52

3.4. Conclusion……..…57

Chapter 4. NAD^+/NADH Tethering on MWNTs-Bucky Papers for NAD^+-Dependent Glucose Dehydrogenase-Based Anodes…….…....58

4.1. Introduction…….…..58

4.2. Experimental Methods……..61

4.2.1. Apparatus……..…..…61

4.2.2. Chemicals ……..……61

4.2.3. Anode Design Procedure……..…....62

4.2.4. X-Ray Photoelectron Spectroscopy……...…….....62

4.2.5. Chronoamperometry……..…63

4.2.6. Chronopotentiometry……...…..64

4.2.7. Michaelis-Menten Analysis……..…64

4.2.8. Stability Study ……..…….……64

4.3. Results……..…64

4.3.1. Bioanode Design…….…...…64

4.3.2. XPS Analysis…….66

4.3.3. Polarization Curves for BEP-MG-GDH/Chitosan/CNTs and CMN-MG-GDH/Chitosan/CNTs anodes.....…71

4.3.4. Storage Stability Study on CMN-MG-GDH anode ……...……...….75

4.3.5. Michaelis-Menten Analysis on GDH/Tethered NAD^+-CMN catalytic Surfaces…….....75

4.3.6. Stability Study at Continuous Working Conditions of GDH and Tethered NAD^+-CMN anodes…….……76

4.4. Conclusion……..…79

Chapter 5. Design of Gas-Diffusion Cathodes Integrating Carbon Nanotube Modified-Toray Paper and Bilirubin Oxidase……...……...….82

5.1. Introduction…….……..82

5.2. Experimental Methods……...….86

5.2.1. Apparatus……..……..…86

5.2.2. Materials…….……..87

5.2.3. Metal catalyst deposition……..……..…….88

5.2.4. Carbon Nanotube Growth by Chemical Vapor Deposition……..…….89

5.2.5. Dual-Layer Assembly and BOx-Enzyme Entrapment……....89

5.2.6. Stability of BOx by Electrochemical Characterization…….....….90

5.2.7. Paper-Based Cathode Microfluidic System Ensemble……...91

5.3. Results……..…….....92

5.3.1. Metal seed deposition……...92

5.3.2. Carbon nanotube growth……..…..93

5.3.3. PH-dependence study…….94

5.3.4. Time-dependence study…….....96

5.4. Conclusion…….…….….97

Chapter 6. Tailored Catalytic Layer for Enzyme Structure Stabilization……..……...99

6.1. Introduction……..…….……99

6.2. Experimental Methods……..……..……101

6.2.1. Apparatus……...101

6.2.2. Materials…….……...101

6.2.3. Bilirrubin Oxidase Enzyme Immobilization for ORR……...……102

6.3. Results…….…….……..….104

6.4. Conclusion……..…….……110

Chapter 7. Nanomaterial-Based Bioanode and Gas-diffusional Biocathode Encapsulated in Polydimethylsiloxane…….……..111

7.1. Introduction…….……115

7.2. Experimental Methods……115

7.2.1. Apparatus……115

7.2.3. Bioanode Fabrication……116

7.2.4. Biocathodes Fabrication……117

7.2.5. Electrochemical Characterization……117

7.3. Results……118

7.3.1. Bioanode Evaluation……119

7.3.2. Bilirubin as Orienting Agent for Bilirubin Oxidase……122

7.3.3. Biocathode Material Evaluation. CMN and HCBP Electrodes……123

7.3.4. Performance of Biocathodes Encapsulated in Polymer……124

7.5. Conclusion……126

Chapter 8. Outlook……128

8.1. Limitations of noble metal catalysts……128

8.2 Considering Applications……129

8.3. Precedents of Implanted BFCs……129

8.4. In vitro and In vivo Studies……131

8.5. Biocompatibility Criteria……134

8.6. Considering the Microfluidic Systems……135

8.7. Conclusion……136

Chapter 9. Conclusion……137

9.1. Enhanced enzyme stability and decrease of limitations of the bioanodic systems – The development of a reagentless NAD^+/NADH-dependent GDH-based anode……137

9.2. Enhanced biocathodic enzyme stability and mitigation of system limitations……..….139

9.3. Integrate the bio-electrodes into a biocompatible polymeric matrix……..….140

Future Outlook…….……141

References……....142

LIST OF FIGURES

Figure 1.1 Enzymatic biofuel cells that use methanol as fuel.....1

Figure 1.2. Graph of the performance of ideal and actual fuel cell voltage/ current……..8

Figure 1.3. Plot of the Tafel equation representing the current on a logarithmic scale in function of its overpotential η and $\beta = 0.5$…….……...9

Figure 1.4. Polarization curves of the glucose-based anode governed by different enzymatic systems and mechanism of electron transfer…….....13

Figure 1.5. Polarization curves of oxygen-based cathode governed by different multicopper oxidase enzymes governed by direct electron transfer mechanism……...…13

Figure 1.6. Polarization curve for glucose/oxygen fuel cell employing enzymatic system undergoing direct and mediated electron transfer mechanisms……...…..…14

Figure1.7. Mechanisms of electron-transfer …….……16

Figure 1.8. Three groups of enzymes based on location of enzyme active centre..…..……18

Figure 1.9. NAD^+ reduction reaction to NADH……...……..……...19

Figure 1.10. Potential of redox couples for dehydrogenase enzymes where NADH/NAD+ is shown to have a potential of -0.584 V at pH 8…….....20

Figure 1.11. Multicopper Cluster Center- Oxygen Interaction….....23

Figure 1.12. a) Laccase-electrode surface interaction, b) Intramolecular electron transfer in Laccase ……..……..…….…….....24

Figure 1.13. a) Schematic structure of a graphene sheet, b) Armchair, c) zigzag, d) chiral configurations in a SWNT……...……...…27

Figure 1.14. Poly(dimethyl siloxane) (PDMS)……...…29

Figure 1.15. Paper-based microfluidic system. A) Image of experimental flow rate study; B) Schematic of fan and relevant parameters to determine volumetric flow rate, q; C) Computational simulation of flow rate driven by capillary action showing velocity of liquid flow; D) Schematic of gas-diffusional cathode assembled on a paper-based microfluidic system ……...…30

Figure 1.16. A) Schematic of Cellobiose dehydrogenase/Bilirubin oxidase EFC integrated in contact lens (M. Falk et al. Biosensors and Bioelectronics 2012, 37,38–45), B) Contact lens sensor tested for continous glucose monitoring on an eye-PDMS model….....32

Figure 2.1. a) Plot of potential vs. time showing a triangular waveform in a CV, b) Cyclic Voltammogram for a reversible redox reaction…….....40

Figure 2.2. a) Stepped potential in chronoamperometry, b) Faradic current and exponential decay of current as a function of time……..……...…….40

Figure 2.3. a) Potenstiostatic Polaryzation Curve, working potential of the electrode is found when current approaches steady state behavior, b) Chronoamperometric curve, current vs. time, at a constant potential, the change in current measured is due to the change of the concentration of the reactant in the cell by aliquots added……..…..41

Figure 2.4. a) Chronopotentiometric curve, potential as a function of time at a constant applied current, b) Red and Ox species concentration with respect to the distance to the working electrode surface ……43

Figure 3.1. Glucose dehydrogenase/ multi-walled carbon nanotube (MWNTs) paper – based anode…….…….48

Figure 3.2. A) Plain BEP in blank 2 solution OCP~ 0.11 V (grey line) and 0.1M glucose OCP of -0.042 V(black line), B) BEP-MG in blank 1 OCP ~ 0.56 V (light grey line), in blank 2 solution OCP~ 0.45V (grey line) and 0.1M glucose OCP of 0.36 V (black line), C) BEP-MG-GDH in blank 2 solution OCP of 0.06 V (grey line) and BEP-MG-GDH in 0.1M glucose OCP of -0.18 V (black curve). BEP-MG-GDH shows the most thermodynamically favorable OCP in presence of its substrate compared to BEP-MG-ADH and BEP-MG-LDH (not shown)……..…….……...52

Figure 3.3. a) and b) Plain BEP. c) and d) BEP with MG and GDH in Chitosan-CNTs matrix……..…53

Figure 3.4. Cyclic voltammograms for BEP-MG-GDH, BEP-MG-ADH and BEP-MG-LDH anodes in electrolytic cell setup in NAD+ 1 mM, KCl 0.1M in PB 0.1M, pH 7.5 (dotted line), and biofuel (glucose, ethanol and lactate respectively) 0.1 M, NAD+ 1 mM, KCl 0.1M in PB 0.1M, pH 7.5 (full line)……..…….……...54

Figure 3.5. A) Michelis-Menten curves performed in the electrolytic cell setup show the activity of the dehydrogenases enzymes. GDH (-■- for 4mg,- ►-) shows the best performance in equivalent conditions with respect to LDH (-◆-) and ADH (-●-): biofuel 0.1M, NAD^+ 1mM, KCl 0.1M in PB 0.1M at pH 7.5. B) Potenstiostatic polarization curves for 3 mg (-

▲-) and 4 mg (-■-)GDH- based bioanode and its respective blanks (plain BEP, BEP-MG, BEP-GDH, blank solutions 1 and 2) show the 3 and 4 mg GDH bioanode has the better performance……..…….55

Figure 3.6. Stability study shows the GDH-based anode maintains ~80% of its initial activity at 15 days of storage at 4ºC in dry conditions……..…….56

Figure 4.1. PBSE interaction with MWNTs surface and NAD^+ linked to PBSE which interacts by pi-stacking interaction with the MWNTs surface……..…….……60

Figure 4.2. SEM images of a) plain BEP paper, b) plain CMN paper in high magnification. SEM images in low magnification of c) plain CMN paper and d) bioanode with polymerized MG and GDH deposited on the surface (CMN-MG-GDH)……..65

Figure 4.3. Nitrogen 1s (a-d) and sulfur 2p (2-f) spectra obtained by XPS analysis of references – MG (a and e), PBSE (b), NAD+ (d) and CMN-MG-PBSE-NAD^+-GDH in Chitosan/CNTs (CMN full set) (d and f)……..…….69

Figure 4.4. Stability of CMN full set within the first 24 hours of continuous operation. a) S/N and P/N ratio; b) N speciation and c) S speciation as a function of time……..70

Figure 4.5. A) Potentiostatic and B) galvanostatic polarization curves performed on BEP-MG-GDH/Chitosan/CNTs and CMN-MG-GDH/Chitosan/CNTs in an electrolytic cells. C) Potentiostatic and D) galvanostatic polarization curves performed in 270º paper-based fan cell……..……72

Figure 4.6. A) Stability study for CMN-MG-GDH/Chitosan/CNTs bioanode showing the current density as a function of time at 0.35V obtained from the potentiostatic polarization curves at 0.35V (inset). B) Michaelis-Menten curves for CMN-MG-PBSE-NAD^+-GDH//Chitosan/CNTs bioanode at 4ºC and 25ºC where the current generated is analyzed as a function of concentration……....75

Figure 4.7. A) Open circuit potential of CMN-MG-PBSE-NAD^+-GDH/Chitosan/CNTs in absence (light grey line) and presence of substrate (grey line) at day 1 and in the presence of substrate at day 2 in an electrolytic cell. B) Potentiostatic polarization curves performed on CMN-MG-PBSE-NAD^+-GDH/Chitosan/CNTs in an electrolytic cell in the absence (-■-) and presence of substrate (0.1M glucose, 0.1 KCl in 0.1M PB) at day 1: measurements taken at 300 seconds intervals (-●-) and at 1 hour interval after OCP, potentiostatic polarization by chronoamperometry and depolarization (-■-, staring after 7 hours of working conditions); at day 2: intervals of 600 seconds (-◇-)……....78

Figure 5.1. Schematic of a gas-diffusion cathode, three phase interface conceptual design for oxygen reduction at the catalytic layer…...……..…….83

Figure 5.2. Hydrolysis and condensation of TMOS-silica precursor in aqueous solution……....85

Figure 5.3. Stack cell assembly for Ni-seed electrodeposition, isometric and side views……88

Figure 5.4. SEM images of metal-seeds deposited on carbon fibers of TP with lower and higher resolution on the left and right, respectively. A) Ni seed deposition at pH4. B) Ni and Co seed deposition at pH7……..……....…92

Figure 5.5. (A) (B) SEM image of plain TP (C) SEM images of TP-CNT-BOx cathode, (D)and TP-CNTBOx-TMOS cathode……...…….93

Figure 5.6. PH-dependency study performance points at 0.3 V for the TP-XC35-CNT-BOx-TMOS cathode in phosphate buffer pH range 5 to 8……..…95

Figure 5.7. Stability study with respect to time, performance points at 0.3 V for the cathode with and without silica in phosphate buffer at pH 7.5……..…….……..…..97

Figure 6.1. PBSE tethered attached to the enzyme by covalent bond and to the MWNT by π-π interaction to the MWNT…….……100

Figure 6.2. Polarization curves of biocathodes stored at 37°C……..…….106

Figure 6.3. Open circuit potential measurements as function of time for biocathodes stored at 4°C in humid conditions……..107

Figure 6.4. SEM Images of HCBP-PBSE-BOx and HCBP-PBSE-BOx-TMOS, and HCBP-CNTs-BOx and HCBP-CNTs-BOx-TMOS …….…….…..107

Figure 6.5. Cyclic voltammetry (CV) of HCBP-based biocathodes using a scan rate of 20mVs^{-1}, CV was performed at the 360th of storage at 4 °C in humid conditions.…….108

Figure 6.6. Current density at 0.25V, measured as function of time for biocathodes stored at 4°C in humid conditions……..109

Figure 7.1. A) Bilirubin molecular structure, B) PBSE tether bonded to enzyme and interacting with the MWNTs wall by π-π interaction……114

Figure 7.2. SEM images of CMN and HCBP…….……..……119

Figure 7.3. Electrochemical characterization of reagentless CMN-based anode integrated into a PDMS matrix (PDMS-CMN-MG-PBSE.NAD-GDH-PDMS)……..……...…..121

Figure 7.4. Current density at 0.3V as function of time for biocathodes utilizing DMSO and ethanol as solvents for bilirubin and PBSE…….....122

Figure7.5. Polarization curves of HCBP and CMN-based biocathodes integrating bilirubin as an orienting agent for BOx enzyme and silica-gel formed by CVD……....123

Figure 7.6. Polarization curves of HCBP-based biocathodes between 0.5 and 0.3V (left) ……..……..……125

Figure 8.1. Schematic representation of the FC implanted and tested in a dog as early as in the late 60s.……130

Figure 8.2 From bioelectrodes to a biocompatible biofuel cell implanted in the abdominal cavity of a rat……..……132

Figure 8.3. Experimental setup of a GOx/BOx microscale EFC implanted into a grape, the two electrodes are drawn with lines to highlight their positions……....133

Figure 9.1. A) Polarization curves of a single cell, 2-cells, and 3-cells stack in series using 0.1M glucose in 0.1M PB, 50mM NAD+, 0.1 M KCl, pH 7……..……...…...…141

LIST OF TABLES

Table 3.1. Michelis-Menten data from chronoamperometric measurements for GDH, ADH and LDH based anodes……..……56

Table 4.1. Elemental quantification of carbon, oxygen, nitrogen and sulfur on plain BEP, plain CMN, BEP-MG, CMN-MG, BEP-MG-PBSE-NAD^+, CMN-MG-PBSE-NAD^+, BEP-MG-PBSE-NAD^+-GDH/Chitosan/CNTs (BEP full set) and CMN-MG-PBSE-NAD^+-GDH/Chitosan/CNTs (CMN full set)……67

Table 4.2. CMN-MG-PBSE-NAD^+-GDH/Chitosan/CNTs at 4ºC and 25ºC, Michaelis-Menten parameters obtained by chronoamperometry at 50mV……..76

Table 5.1. Performance of XC-TP-BOx-TMOS at different pH at 0.3V and 0 V……..……95

Chapter 1. Introduction

Biofuel cells (BFCs) are power devices that harvest electric energy from the oxidoreduction reactions of organic compounds.[1-5] In literature, these are classified as a) devices that utilize redox proteins and enzymes, microorganisms or mitochondria, in order to assimilate a biofuel and generate electric power or b) fuel cells (FCs) that convert organic and/or inorganic substrates, which are defined as biofuels and bio-oxidants, employing inorganic catalysts.[6] The first type of BFCs, denominated as "biological fuel cell", is the subject of this research that aims to integrate these devices into the biomedical field.

Biological fuel cells and conventional fuel cells work mostly through the same principles. Despite of their similarities, BFCs emerge as a response to the demand of electrical power devices that can operate in near- neutral pH, physiological condition, and ambient conditions where conventional fuel cells fail. In these systems, the biofuel is oxidized on the bioanode releasing electrons that move to the biocathode through an external circuit generating electric energy (Figure 1.1). Simultaneously, protons generated at the anode traverse the electrolyte towards the biocathode due to a proton driving force. Electrons combine with oxygen and protons at the cathode surface to produce water. BFCs are viewed as a potential green technology for environmental and biomedical applications.

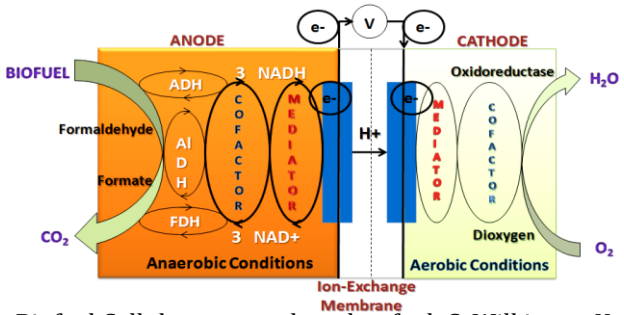

Figure 1.1. Enzymatic Biofuel Cell that use methanol as fuel, *S. Wilkinson, University of Florida.*

In order to design practical and applicable BFCs for powering or for use in biomedical applications, several technologies have to be developed. This research considers the applications of BFCs for powering biomedical devices (BMDs) that can be used in different parts of the body, covering different needs, and having different applications, including: 1) micro- and nanoelectrodes to transfer the signal between nerves and muscles; 2) implanted and extracorporeal sensors to monitor specific parameters in the body; 3) power sources for implants requiring long lasting energy sources ; 4) data communication devices between the body and a unit located externally; 5) sensing systems to provide trigger mechanisms for implants or drug delivery systems and so forth. Thus, we need to discuss existing classifications of those biodevices to decide what types of BFC design are feasible to be used for power generation. Different types of BFCs based on different biocatalysts, namely whole living cells, organelles, or isolated redox proteins and enzymes, have their own advantages and disadvantages, as described below.

1.1. Types of Biofuel Cells

1.1.1. Cells-based fuel Cells

Microbial fuel cells (MFCs) utilize whole microorganisms to create the bio-electrodes, granting a high stability and long lifetime to the constructed biodevices.[7, 8] By employing whole microorganisms as catalysts, the FC is capable of fully oxidizing different organic fuels, such as sugars, fatty acids, and alcohols. This gives MFCs an advantage over other types of BFCs, having higher theoretical efficiency. However, due to the different physiological conditions in which bacteria grow, the limitations vary; these depend on the pH of the solution and temperature, among other growth factors. These factors can contribute to low current and power

densities of the device. Additionally, MFCs suffer from slow mass transport of the fuel across the cell membranes and a low electron/electrode surface interaction due to biofilm formation on the electrode surface.[5] Moreover, a whole cell is significantly larger than organelles or isolated proteins, making MFCs rather large with low current and power densities. A major issue for utilizing MFCs to power biomedical devices is the high risk of infection, resulting in MFCs generally being disregarded from biomedical applications.

Recently, Han *et al*. proposed to utilize an MFC implanted in the human colon.[8] Because of the large number of anaerobic microorganisms naturally present in the intestinal mucosa and, at the same time, many aerobic microorganisms in the lumen flowing with fecal matter, the risk of infection would not be a major concern. Specifically, a tubular MFC was designed, with a microbial anode intended to adhere to the colon mucosa and a Pt-containing cathode intended to be located in the center of the lumen. The rather large MFC (with a volume of 125 mL for each compartment) was investigated in a fluid designed to simulate the intestinal fluid. The biodevice generated stable power for 2 months with an open circuit voltage (OCV) of 552 mV and a maximum power density of 73 mWm^{-2}. The power output was limited by the cathode, which was attributed to the small surface area of the electrode and the low O_2 concentration.

Instead of utilizing bacterial cells, Justin *et al.* proposed a new innovative approach employing white blood cells to generate current.[9] The authors called the new biodevice a "metabolic biofuel cell," which describes the nature of the power production very well - metabolic conversion of the substrate from living cells that are not microorganisms. The white blood cells were isolated from human blood and used as bioreactors at the anode. The two-chamber BFC separated by a Nafion proton exchange membrane was designed by combining the bioanode with a carbon fiber electrode placed in the cathodic compartment, containing potassium

ferricyanide. Although the obtained current densities were rather low, with power output between 0.9 and 1.6 $mWcm^{-2}$, the research shows the possibility of using human cells and fluids to generate power. Such a design would overcome many of the problems connected with BFCs operating *in vivo*. The same group of researchers theorize how such a BFC could be used for powering neural implants.[10]

1.1.2. Organelle-Based Fuel Cell

As an alternative to employing whole cells in the design of BFCs, Minteer along with her coworkers have explored the possibility of utilizing mitochondria as biocatalysts.[11, 12] Mitochondria offer a compromise between the high efficiency of MFCs and the high volumetric catalytic activity of EFCs. The organelle contains all of the enzymes needed for certain fuel oxidation. Moreover, researchers have shown that pyruvate, succinate, and fatty acids can be utilized as fuel with experimental evidence indicating the possibility of utilizing amino acids as well.[11] Reported mitochondrial FCs have shown better performance (~ 0.2 $mWcm^{-2}$) compared to MFCs (~ 0.001–0.1 $mWcm^{-2}$),[12] which can be attributed to several factors. First, mitochondrial FCs have lower fuel transport limitations when compared to MFCs because the lack of a cell membrane in the mitochondrial-based biodevice allows for small diffusion lengths. Second, usage of mitochondria allows for a higher load of biocatalysts on the electrode surfaces. Third, mitochondria do not form biofilms that interfere in the electrode-active site-electrolytic solution interaction, which can decrease the actual efficiency of MFCs.

1.1.3. Enzyme-based Fuel Cell

Enzymes are, in general, exceptional catalysts with a high substrate specificity, and due to the smaller size of enzymes compared to whole cells and organelles, enzymes can, theoretically, be utilized to create FCs with higher power density compared to other types of BFCs. Indeed,

enzymatic FCs (EFCs) with a power density over 1 $mWcm^{-2}$ with an OCV close to 1 V have been reported in the literature.[13]

EFCs are the most promising, when considering biocompatibility, selectivity, efficiency, and sensitivity criteria. In addition, EFCs could be employed to power nano- and microelectronic portable devices, drug delivery systems, biosensors, and implantable biomedical devices.[14-16] The high selectivity of enzymes makes their utilization in FC applications, as natural catalysts, very beneficial by eliminating problems of cross-reactions and poisoning of the electrodes. This allows for membraneless, single-compartment FCs and casings to be designed, while still mitigating voltage loss that otherwise could arise. Enzymes can potentially be produced at a low cost and can perform at neutral pH, and room temperature, ideal for non-implantable devices, and physiological conditions for implantable biomedical devices (BMDs). However, it should be noted when comparing EFCs to other types of BFCs, the efficiency of these devices is limited by incomplete fuel oxidation and shorter lifetime because of limited enzyme stability.

Due to the many advantages compared to other catalysts, as new enzymes and ways to implement them in electrode designs have emerged, the research interest in EFCs has grown significantly. For example, in 2004 Calabrese Barton et al. published a thorough comparison of the strengths and weaknesses of BFCs, listing possible applications.[14] In the same year, the advances in miniature BFCs were reviewed by Heller.[15] In 2008, Armstrong et al. published a detailed account of the use of enzymes in FC technology.[17] Significant progress has been made in the last decade, and when considering mainly the implantable applications, the use of sugar/O_2 BFCs has received increased attention. Therefore, this research focuses in the design and development of glucose/O_2-based EFCs for potential biomedical applications.

1.2. Fuel Cells -Performance

Cell operation and performance can be explained by a practical thermodynamics analysis relating the biofuel cell design and its performance variables. Once the ideal performance of the biofuel cell has been determined, the losses of the cell can be calculated and deducted from the ideal performance to describe the real operation. As in conventional fuels cells, the real operation performance of the biofuel cell is subject to the conditions during operation.[18]

The ideal performance of a conventional FC depends on the electrochemical reactions that occur with different fuels and oxygen. In this way, low-temperature fuel cells, which work with hydrogen as the fuel, require noble metals working as electrocatalysts to lower the activation energy of the reactions and achieve practical reaction rates at the anode and cathode. High-temperature fuel cells however have relaxed requirements for catalysts and fuel sources.

As an example, in a Proton Exchange Membrane Cell in acid media, the anode and cathode reaction for hydrogen is as follows:

Anode reaction: $H_2 \longrightarrow 2\,H^+ + 2e^-$

Cathode Reaction: $\frac{1}{2}\,O_2 + 2\,H^+ + 2e^- \longrightarrow H_2O$

Overall Reaction: $H_2 + \frac{1}{2}\,O_2 \longrightarrow H_2O$

The Nernst equation defines the ideal performance of a FC as the potential at zero current. The Nernst equation relates the maximum ideal potential ($E_{0,\ cell}$) of the cell and the equilibrium potential ($E_{\ cell}$) of reactants and products at non-standard temperatures and pressures. By knowing the ideal potential at standard conditions ($E°_{0,cell}$), the ideal potential at

other temperatures and pressures (E_{cell}) can be determined through the use of the equations below.

$$E_{cell} = E_{0,cell} + \frac{RT}{2F} ln\left(P_{H_2} * \left(P_{O_2}\text{^}0.5\right)\right) \quad \text{Eq. 1}$$

with $$E_{0,cell} = E^{o}_{0,cell} - k(T - 298K) \quad \text{Eq. 2}$$

where P is the gas pressure, R is the universal gas constant, T is the absolute temperature, F is Faraday's constant, E_{cell} is the equilibrium or reversible overall potential of the cell, and $E°_{0,cell}$ is the potential at 1 atm and 298K or open circuit voltage.

The total Gibbs free energy change (ΔG) due to a change in potential is equal to $nF\Delta E$ *or* $nFE_{0,cell}$. The change in Gibbs free energy due to changes in the potential for the cathodic and anodic reactions, for the example above H_2/O_2, is:

$$\Delta G = \Delta G_o - RT\, ln\left(P_{H_2} * \left(P_{O_2}\text{^}0.5\right)\right) \quad \text{Eq. 3}$$

The maximum theoretical cell potential is known as the thermodynamic or reversible open circuit potential ($E_{0,cell}$), the open circuit voltage (OCV) or the electromotive force (EMF).

$$E_{o,cell} = \frac{-\Delta G_f}{nF} \quad \text{Eq. 4}$$

Here, n is the number of electrons exchanged in the reaction and ΔG_f is the Gibbs free energy of formation of anodic and cathodic species. Following the example above, for the H_2/O_2 fuel cell, the ideal standard potential ($E°$, *cell*) is 1.23 volts when the product is liquid water (n = 2). The change in energy will represent the change of the potential force for the reaction of hydrogen and oxygen. The change in Gibbs free energy of the cell increases as the temperature decreases and the ideal potential of the cell is proportional to the change in the Gibbs free energy.

$$E_{0,cell} = EMF = \frac{-\Delta G_f}{2F} = 1.23\,V\,(@298\,\mathrm{K}) \qquad \text{Eq. 5}$$

However, the ideal condition described so far does not demonstrate the behavior of an actual fuel cell; the standard Nernst potential ($E°_{,cell}$) refers to the ideal cell potential at standard conditions neglecting the losses at which a real fuel cell is subjected to.

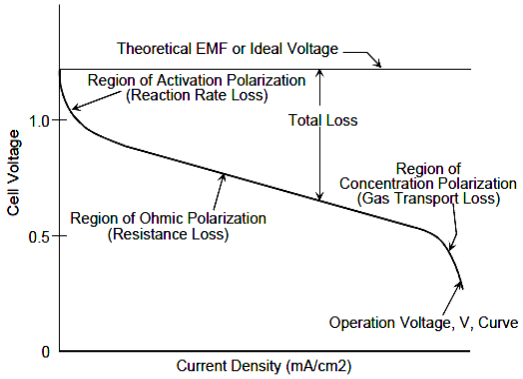

Figure 1.2. Graph of the performance of ideal and actual fuel cell voltage/ current

As the graph above shows, the actual cell potential is lower than its ideal equilibrium potential due to effects of irreversible losses. The losses produce a fuel cell voltage (V) that is lower than its ideal potential E_{cell} ($V = E°_{cell}$ - *Losses*). The losses, known as polarization overpotential or polarization overvoltage (η), are produced from three different sources and affect the cell performance at certain current densities regimes (represented in Figure 1.2). At low current densities, the activation or kinetic overpotentials (η_{act}) are observed due to slow rates of reaction or slow reaction kinetics taking place on the surface of the electrode. A portion of the potential generated is lost in driving the reaction. The activation overpotentials are described by the Tafel equation:

$$\eta_{act} = \beta \ln\left(\frac{i}{i_o}\right) \qquad \text{Eq. 6}$$

where i_0 is known as the exchange current density and corresponds to a dynamic equilibrium. This depends on the concentration of electroactive species and the free energy of reaction at the rest potential with respect to reactants and products. Also, i is the overall current density (i_a+i_c) and β is the Tafel slope obtained by plotting the logarithmic form of the Tafel equation for the reactions in the cathode (a) and anode (b):

$$ln(i_a) = ln\, i_o + \left(\frac{(1-\beta)nF}{RT}\right)\eta \quad \text{(a)} \qquad ln(i_c) = ln\, i_o + \left(\frac{n\beta F}{RT}\right)\eta \quad \text{(b)} \qquad \text{Eq. 7}$$

β is a constant of asymmetry parameter, this expresses the symmetry of the logarithmic current density curve with respect to the overpotential of the electrodes (Figure 1.3).

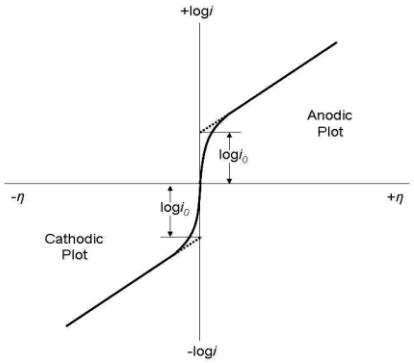

Figure 1.3. Plot of the Tafel equation representing the current on a logarithmic scale in function of its overpotential η and β = 0.5

For slow reactions, β has a high value describing a high drop of potential. This is a function of the temperature and the electrons transferred:

$$\beta = \frac{RT}{n\alpha F} \qquad \text{Eq. 7 (c)}$$

Here, α is the charge transfer coefficient, F is the Faraday constant, R is the ideal gas constant, T the absolute temperature and n is the number of electrons transferred in the oxidation of reduction reaction.

The ohmic or resistive overpotential (η_{ohm}) is observed at intermediate current densities because the electrolyte and the electrode material follow Ohm's law. The ohmic overpotential is linearly proportional to the current densities. The voltage drop is a consequence of electric resistance of the electrode materials and the flow of ions in the electrolyte solution.

$$\eta_{iR} = iR \qquad \text{Eq. 8}$$

where i is the electric current and R is the total resistance of the cell, which includes the electronic and ionic resistances. Decreasing the separation of the electrodes and enhancing the ionic conductivity of the electrolyte in solution help to decrease the ohmic losses.

At high current densities (Figure 1.2), the limiting factor is the concentration or mass transport overpotential (η_{conc}). The concentrations of the reactants decrease while the oxidoreduction reactions are taking place on the electrode surface. This produces the inability to maintain the sufficient concentration of the fuel close the electrode surface due to slow mass diffusion; the electrode starves. This could be due to the small pore size of the electrode material limiting the accessibility of the reactants to approach the reaction sites, or due to the slow diffusion of the reactants and products to or from the electrode surface or reaction site respectively through the electrolytes in solution. Generally, the concentration overpotential is affected mostly by the diffusion of the reactants or products to or from the reaction sites. The concentration overpotential is defined as:

$$\eta_{conc} = \frac{RT}{nF} ln\left(\frac{C_S}{C_B}\right) \qquad \text{Eq. 9}$$

where C_S is the surface concentration on the electrode and C_B is the bulk concentration. According to Fick's First Law and Faraday's Law, the equation above can be written as the

Nernst equation:

$$\eta_{conc} = \frac{RT}{nF} ln\left(\frac{i_{lim} - i}{i_{lim}}\right) \quad \text{Eq. 10}$$

Where i_{lim} is the limiting current defined in terms of the diffusion coefficient. Rearranging (D), the Nernst diffusion layer (δ), and the bulk concentration (C_S), i_{lim} yields,

$$i_{lim} = nFD\left(\frac{C_S}{\delta}\right) \quad \text{Eq. 11}$$

Then, the overall fuel cell overpotential turns to be:

$$\eta_{total} = \eta_{act} + \eta_{iR} + \eta_{conc} \quad \text{Eq. 12}$$

The activation and concentration overpotentials can exist at both cathode and anode electrodes in a fuel cell. These values can then be added for each electrode to give a total overpotential for the cathode, $\eta_{total,c}$,and a total overpotential for the anode, $\eta_{total,a}$.

$$\eta_{total,c} = \eta_{act,c} + \eta_{conc,c} \quad \text{(a)} \qquad \eta_{total,a} = \eta_{act,a} + \eta_{conc,a} \quad \text{(b)} \quad \text{Eq. 13}$$

These effects of polarization shift the potential of the electrode (E_c and E_a) to new values, V_c and V_a, for cathode and anode respectively:

$$V_c = E_c + \eta_{total,c} \quad \text{(a)} \qquad V_a = E_a + \eta_{total,a} \quad \text{(b)} \quad \text{Eq. 14}$$

Finally, for the overall cell, the cell voltage, accounting for overpotential or losses, is given by the following equation

$$V_{cell} = V_c - V_a - \eta_{iR} \quad \text{Eq. 15}$$

The power output of the fuel cell is then defined as the product of the current density and the overall fuel cell voltage as follows:

$$P = i \cdot V_{cell} \qquad \text{Eq. 16}$$

1.3. Glucose/Oxygen Cell -Performance

Enzymatic biofuel cells have the advantage of generating a higher power density; in theory, this range is between 1.65 to 4.1 $mWcm^{-2}$.[12] However, their performance is limited by incomplete oxidation of fuel and low lifetimes. For example, the partial oxidation of glucose by a dehydrogenase would release 2 of 24 electrons decreasing as well the theoretical energy density by 1/12.[19] To oxidize glucose to carbon dioxide, the anode should contain the enzymes responsible for the oxidation of glucose to pyruvate found in the glycolitic pathway, in addition to the enzymes found in the Krebs cycle for complete oxidation of pyruvate.[12, 19, 20] The complete oxidation of glucose gives $\Delta G^{o'}$=-686,000 cal mol^{-1} or -2,870 $kJmol^{-1}$ at standard biological conditions (1 M glucose, 1atm, pH 7, 298 K).[21] In the electrochemical cell, the two half-cell equations are for the first step of glucose oxidation are:

Anode Reaction:	$C_6H_{12}O_6 + H_2O \longrightarrow C_6H_{12}O_7 + 2H^+ + 2e^-$		E^o_a= -0.63 V
Cathode Reaction:	$O_2 + 2H^+ + 2e^- \longrightarrow H_2O$		E^o_c = 0.59 V
Overall reaction:	$C_6H_{12}O_6 + O_2 \longrightarrow C_6H_{12}O_7$		ΔE^o_{cell}= 1.22 V

The potential of the glucose/O_2 cell will be the difference in electrochemical potential of the anode and cathode redox potentials. At standard conditions, the glucose/O_2 fuel cell can produce 1.22 V of potential since the thermodynamic potential of the glucose oxidation is -0.63 V and the O_2 reduction is 0.59 V (figure 1.6).[14, 22] However, the overall performance of the cell is determined by the catalytic properties of the enzymes being employed as biological catalyst for

glucose oxidation at the anode and the O_2 reduction at the cathode. These systems will determine the mechanism of reaction and, finally, the potential of the electrodes according to the experimental conditions (as depicted in figures 1.4 and 1.5, respectively). According to the theoretical finding for enzymatic systems on the electrodes, the cell could reach potentials of 0.75V when anodic enzymatic systems show Direct Etectron Transfer (DET) mechanism (blue curve, figure 1.6) and 0.5V for Mediated electron Transfer (MET) mechanisms (pink curve, figure 1.6). The theoretical potentials shown in figure 1.5 are considered for systems subject to ohmic losses, mass transfer losses and kinetic losses from the substrate redox reactions and the mediators used (i.e. Poly-MG).

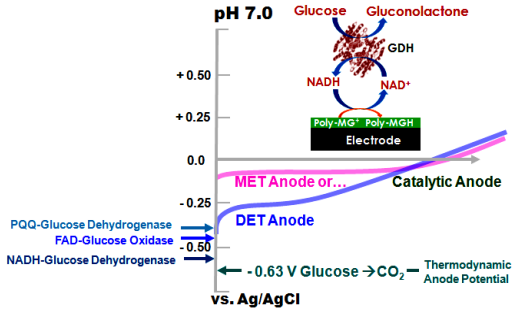

Figure 1.4. Polarization curves of the glucose-based anode governed by different enzymatic systems and mechanism of electron transfer (Image source: *Bio-electrochemical Interface: The Case for Enzymatic Biofuel Cells, September 12, 2013 -Presentation, Prof. Atanassov, UNM*).

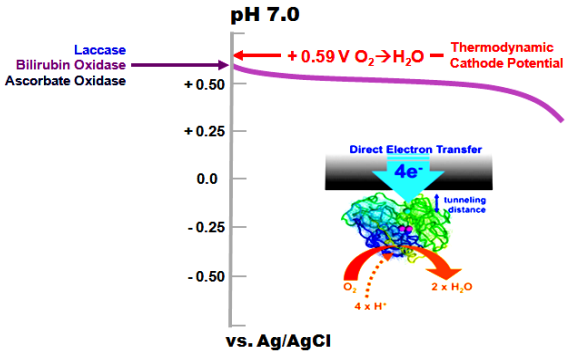

Figure 1.5. Polarization curves of oxygen-based cathode governed by different multicopper oxidase enzymes governed by direct electron transfer mechanism (Image source: *Bio-electrochemical Interface: The Case for Enzymatic Biofuel Cells, September 12, 2013 -Presentation, Prof. Atanassov, UNM*).

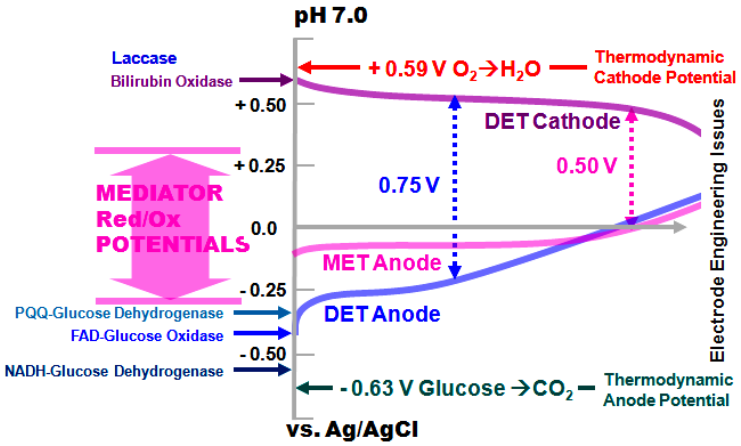

Figure 1.6. Polarization curve for glucose/oxygen fuel cell employing enzymatic system undergoing direct and mediated electron transfer mechanisms (Image source: *Bio-electrochemical Interface: The Case for Enzymatic Biofuel Cells, September 12, 2013 -Presentation, Prof. Atanassov, UNM*).

1.4. Principles and Design Aspects of Enzymatic Fuel Cells

As stated for FCs, the power output of a BFC is determined by the actual cell voltage and the current density of the biofuel cell.[18, 23] For an EFC, the cell voltage is governed by the thermodynamic potentials of the enzymes at the cathode and the anode, and the mechanism of electron transfer between the electrode surface and the enzymes.[2, 23] Similarly to conventional FCs, the oxidation of the biofuel is catalyzed in the anode and the reduction is catalyzed in the cathode but by action of oxidoreductases enzymes. The enzymes transfer the electrons of the oxidoreduction reactions by interacting with the electrode surface directly or by use of mediators.

Many aspects should be considered in the design of an EFC, where the most suitable design is dependent on the intended application.[14, 24-26] Some medical products that could potentially benefit from incorporation with EFCs are: a) cochlear and retina implants, functional electrical stimulation and intracranial pressure sensor implants, glaucoma and sphincter sensors, as well as artificial sphincters within implantable medical device application, and b) transdermal-

patch sensors and drug delivery systems, contact lens sensors and drug delivery systems and super-vision contact lenses within extracorporeal medical device applications. Each of these applications imposes different demands on the BMD. For example, brain fluid has different characteristics (fuel concentration, pH, temperature, free O_2 content, etc.) compared to blood, saliva, tears, urine, and other physiological fluids. Which enzymes are chosen is determined by the biofuel and bio-oxidant available in the host organism, which then is combined with a suitable electrode material. In order for the biodevice to function, an electrical connection between the biocatalyst (redox enzyme) and the electrode surface must be achieved. Furthermore, systems for mass transport of a substrate from the body fluid to the electrodes, as well as size and shape of the BFC, must be considered based on the requirements of the intended BMDs, be it intravascular, extravascular, transcutaneous, and so forth.

1.4.1. Mechanisms of Electron Transfer

In order for an EFC to operate, the enzyme needs to be electrically connected to the electrode surface. The electron transfer (ET) between enzymes and electrodes has been reviewed in detail by Schuhmann and coworkers[27] and Willner and coworkers[28] among others. Electronic connection can be achieved through mediated and direct electron transfer mechanisms (MET and DET mechanisms respectively).[29]

In the first case, the catalytic site is often "buried" deeply within the protein matrix so consequently, the active center is insulated. In this case, exogenous mediators help to overcome this barrier. These redox species, either in solution or immobilized in redox polymers attached to the electrode surface, shuttle electrons between the enzyme and the electrode and vice versa (Figure 1.7.b). Pioneering work in this research field applied to BFCs was performed by Heller *et al* with significant contributions regarding mechanisms to electrically connect to the redox site of

different enzymes by employing redox hydrogels.[30, 31] In order to facilitate the electrical connection between enzymes and electrodes, Heller and his coworkers attached enzymes to ferrocene groups;[32] additionally, they were the first to utilize osmium (Os)-based redox polymers to efficiently "wire" enzymes to electrodes.[33-36] By utilizing this design to create EFCs, a significantly higher power output as well as a simpler construction can be achieved by immobilizing the mediator on the electrode surface together with the enzyme.[37] The development of these electrodes has had important impact on both enzyme-based biosensors[38] and BFCs.[39] Although the use of mediators is necessary for these kinds of enzymes, it usually generates losses of electrode potential.

In the case of DET, the active center of the enzyme is directly electrically connected to the electrode surface. DET transfer requires that the distance of the active site of the enzyme and the surface of the electrode is short enough for electron tunneling (Figure 1.7.a). The specifics of different DET-based BFCs was recently reviewed by Shleev and his coworkers.[40] However, only a minority of known redox enzymes are capable of DET.[41]

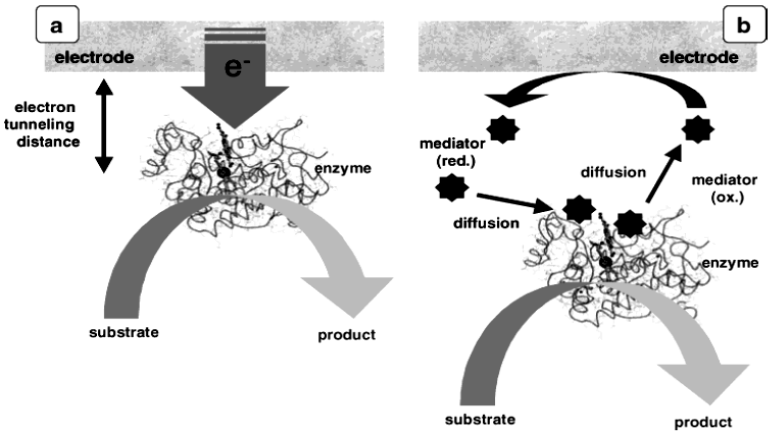

Figure1.7. Mechanisms of electron-transfer. (a) Direct electron transfer (tunneling mechanism) from electrode surface to the active site of an enzyme. (b) Electron transfer via redox mediator (Calabrese *Barton et al. Chemical Reviews, 2004, 104, 4867).*

These two approaches have different advantages and disadvantages. MET-based biodevices usually have very efficient ET between the enzyme and the electrode surface leading to comparatively larger current output. However, to facilitate the wiring of enzymes, the redox potential of the redox polymer needs to be slightly positive toward the anodic enzyme in order to create the bioanode and vice versa, slightly negative to create the biocathode, which translates to a small voltage loss for MET based devices compared to DET-based BFCs.

1.4.2. Enzymes

Due to the abundance of sugars and O_2 available in the host organism and due to the generally non-toxic by-products of their reaction, sugar-oxidizing and O_2-reducing enzymes are attractive biocatalysts for designing EFCs intended for biomedical applications.

Enzymes used in biofuel cells are biocatalyst proteins that accelerate oxidoreduction reactions. They can be categorized in three groups based in the location of the active site of the enzyme (Figure 1.8) and the method of electron transfer between the active site and the electrode surface.[42] Enzymes with diffusive active center (Figure 1.8.a) are generally nicotinamide adenine dinucleotide ($NADH/NAD^+$ or $NAD(P)H/NAD(P)^+$) dependent enzymes- these have redox centers weakly bound to the protein enzyme (*e.g.* glucose and alcohol dehydrogenase).[30] Enzymes with active sites closer to the shell of the structure have better interaction with the electrode surface (Figure 1.8.b, *e.g.* oxygen reduction multicopper oxidases such as laccase and bilirubin oxidase and peroxidases such as cytochrome c peroxidase). The aforementioned class of enzymes may interact with the electrode surface by a DET mechanism. On the other hand, enzymes with the active site "buried" deeply into the shell have no interaction directly with the electrode and the ET mechanism is mediated (example in =Figure 1.8.c).

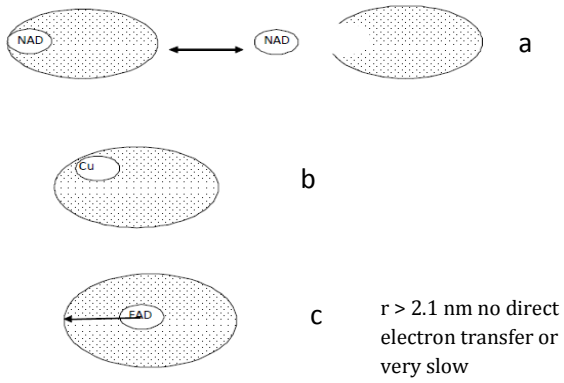

Figure 1.8. Three groups of enzymes based on location of enzyme active centre *(* E. H. Yu and K. Scott*. Energies* 2010*, 3,* 23.*)*

1.4.2.1. Enzymatic systems for Bioanode Design

The most usual choice for anodic enzyme has been glucose oxidase (GOx),[43] which, when under mediated ET conditions, can effectively electro-oxidize glucose. The enzyme carries the flavin adenine dinucleotide cofactor (FAD) buried deep within the enzyme structure, which makes DET difficult. Although DET with GOx have been reported in many different studies (e.g. refs.[13, 44-50]) there is an ongoing debate as to whether the true DET mechanism is realized or whether bio-electrocatalytic currents are observed due to naturally mediated glucose oxidation by free FAD, which has diffused out from the active centers of some partly denatured enzyme molecules. A problem with using GOx in BMDs is the fact that O_2 is the natural electron acceptor, and the enzyme produces hydrogen peroxide (H_2O_2) in the presence of O_2, which is toxic, and hence requires additional modifications of biodevices for their operation in vivo, making the implementation of this enzyme difficult for implantable devices, specifically. In addition to the undesired biocompatibility issues, hydrogen peroxide can both reduce and oxidize, and thus can create parasitic (crossover) currents, particularly in a long-term, continuous operation of a biodevice.

Alternatives to GOx are the pyrroloquinoline quinone (PQQ)-dependent GDH [46, 51, 52 46] and cellobiose dehydrogenase (CDH)[53-55]. PQQ-dependent GDH enzymes contain the PQQ-cofactor as part of the enzymatic structure and CDDH holds FAD and heme domains within its structure. Both enzymes have been utilized to create DET based bioanodes.[54] However, the downside with utilizing CDH is the fact that glucose is not the natural substrate of the enzyme; thus, the catalytic efficiency is significantly reduced compared to GOx-based biodevices. Also, PQQ-dependent GDH has demonstrated small current generation when compared to NADH/NAD^+-dependent enzymes.

Also to avoid the influence of O_2 on bioanodes, NADH-dependent glucose dehydrogenase (GDH) can be used. So far, no reports of DET based bio-electrocatalysis for this enzyme exist, and the ET in GDH based bioanodes are generally performed using nicotinamide adenine dinucleotide (NAD^+) cofactor.[56, 57] To facilitate this, different catalysts for the oxidation of NADH can be used as free mediators (in solution) or polymerized on the surface of the electrode.[58-61]

The oxidation of the glucose substrate is coupled to the reduction of the NAD^+ cofactor to NADH. The reoxidation of NADH to NAD^+ is necessary to perpetuate the reaction.

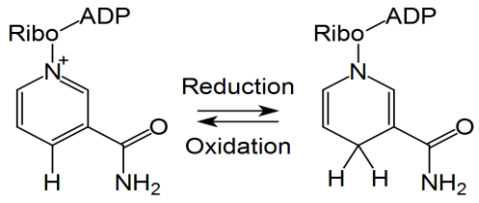

Figure 1.9. NAD^+ reduction reaction to NADH

NADH/NAD$^+$ is a two electron, one-proton redox couple that undergoes a radical mechanism of oxidation. The initiation of the reaction through this mechanism, which is the formation of the first cation-radical complex, is the limiting step of the reaction (see below). [62-69]

$$NADH \xrightarrow{-e^-} NADH^{*+} \xrightleftharpoons{-H^+} NAD^* \xrightarrow{-e^-} NAD^+$$

The excitation step forms a hybrid that later could derive into an alpha or beta form of the molecule. The formation of either of the forms is determined by the interaction of the intermediate structure with the enzyme. The inclination to generate those forms is related to the characteristics of the active site, it is different for different dehydrogenases.[70] As a result, NADH needs to further transfer the charge to the electrode to release the electron and conduct work. This process occurs at large overpotential, as large as 1 V in an energetic scale (Figure 1.10). The successful oxidation of this cofactor offers the opportunity for using any of the NADH dependent dehydrogenases and, in this way, a larger range of biofuels.

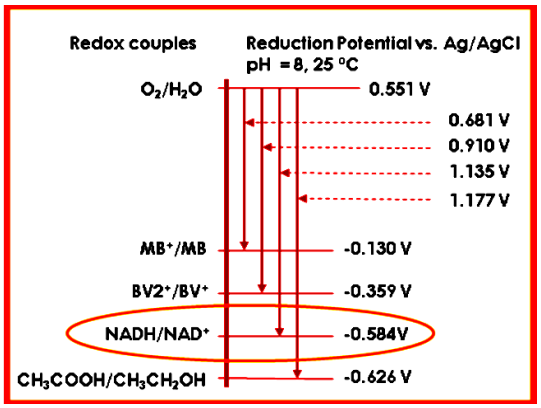

Figure 1.10. Potential of redox couples for dehydrogenase enzymes where NADH/NAD+ is shown to have a potential of -0.584 V at pH 8 *(M. J. Cooney and B. Y. Liaw. P.S. Wang and J. B. Kim Editors. Biomolecular Catalysis: Nanoscale Science and Technology. 2008)*

The oxidation of NADH can be performed by using a catalyst to improve the kinetics of the reaction accelerating the first step of the radical mechanism mentioned above, shuttling the electron transferred from the electrode to the NADH substrate.[58-61, 71] The mediator must undergo

a two-electron process as well in order to accomplish a catalytic reaction[72] and simultaneously approach controlled-diffusion reaction rates. Additionally, to accomplish a satisfactory electrode design, the mediator must be immobilized on the electrode surface by undergoing an irreversible process that confers long-term stability and stability in presence of NADH. Moreover, the selectivity of the catalyst is prevailing; it should be selective for NADH to make NAD^+ available for the enzyme without having parallel reactions with other components of the solution.[57, 73-77]

In previous research good mediators for NADH oxidation, which included phenothiazine and phenoxazine derivatives, characterized as *ortho*- or *para*-quinones, were identified.[58-61, 78] It was observed that phenothiazine mediators had good catalytic activity due to the properties of the organic heterocyclic structures with C-C double bonds; single and double bonds alternating along the structure. The structure allows for good interaction with the electrode surface. Tse and Kuwana achieved the decrease of the NADH reaction overpotential to 0.4V using monolayer-modified-surface glassy carbon electrodes.[79] These electrodes were created by treating the glassy carbon surface with cyanuric chloride and later modified with dopamine, or 3,4-dihydroxybenzylamine.

Other studies have demonstrated that Meldola's blue and toluidine blue can be used in an electrochemical sensor for NADH on carbon electrodes[80, 81]. Pessoa et al immobilized Meldola's blue and toluidine in silica oxide matrices and bulk zirconium phosphate.[81] More studies have suggested the use of methylene blue and methylene green (MG), phenothiazine dyes, as possible mediators for this reaction. Dai et al showed successful immobilization of MG on glassy carbon for NADH sensing as well.[78] The contribution from Karyakin et al, Svoboda et al and Rincon et al in the electroanalysis and structural studies performed on MG were determinants in choosing

this mediator in the research presented here.[58, 60, 61, 82, 83] Rincon et al showed electrocatalytic activity of the polymerized MG (PMG) on glassy carbon with a potential as low as 50 mV (vs Ag/AgCl) toward the oxidation of NADH.[83] Later, MG was successfully polymerized on single multiwalled carbon nanocomposite materials.[84]

Considering all the factors mentioned above, this research focused in creating electrodes that could accomplish both oxidation of NADH and glucose by using MG as mediator. Additionally, this research had considered the fact that NAD^+/NADH has not been successfully immobilized on an electrode surface, but rather needed to be fed externally to the cell, limiting the utility of such enzymes in BMD applications. As a consequence, this research also aimed to integrate the cofactor into the bioanode design along with the enzymatic system to develop a reagentless glucose bioanode.

1.4.2.2. Enzymatic systems for Biocathode Design

Multi-copper oxidases (MCOs), such as laccase (Lc), ceruloplasmin, and bilirubin, as well as ascorbate oxidases (BOx and AOx, respectively) have been extensively investigated as cathodic biocatalysts for DET based FCs.[40, 85] Also, Heller and his coworkers have employed these enzymes in MET-based approaches and demonstrated the ability to create powerful biocathodes by "wiring" Lc or BOx using electrically conducting Os-containing hydrogels.[86, 87]

These MCOs have a catalytic center consisting of four copper atoms;[88, 89] a T1 Cu site, which accepts electrons from the substrate and from the electrode surface and a T2/T3 cluster, where O_2 is reduced directly to water (Figure 1.11). In the active site of the enzymes, the T1 Cu is the primary electron acceptor, located at approximately 6.5 Å deep in the enzyme structure allowing electron tunneling and DET. The T2/T3 cluster is located at 12 Å from the electrode

surface and was proven to be the site where the molecular oxygen is attached by hydrogen bonding. The enzyme stores electrons that travel from the anode by getting completely reduced; this state contains four electrons that can be transferred to oxygen.

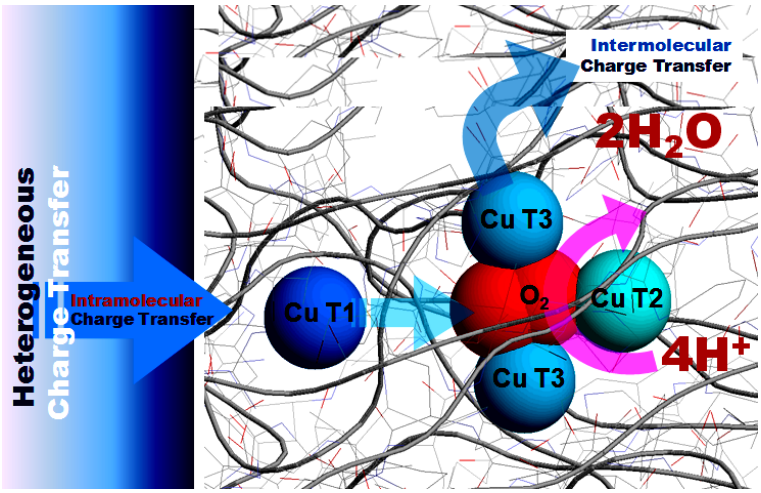

Figure 1.11. Multicopper Cluster Center- Oxygen Interaction (*Image source: Multicopper Oxidases-Presentation, Plamen Atanassov*).

The reduction reaction starts when oxygen is bonded to the fully reduced Cu trinuclear cluster in presence of protons. The reduction of oxygen is initiated by reducing the T1 Cu and subsequently tunneling the electron down a His-Cis-His tripeptide to the trinuclear Cu cluster (Figure 1.12.b, Hopping ET). [90, 91] At least one of the two electrons from the T1 Cu is tunneled toward the T3 Cu in the trinuclear cluster. T2 Cu is necessary for the oxidation of this reduced T3 Cu allowing it to act as a two electron acceptor. It is believed that T2 Cu participates in the transfer of one of the electrons required to reduce T3 Cu, leading to the stabilization of the intermediary complex generated when oxygen is attached to the trinuclear cluster.[88] It was suggested also that alkaline values of pH promote the formation of a T2-OH complex (Figure 1.12.b, Non-hopping ET), inhibiting the oxygen reduction since T3 Cu cannot accept an electron until the OH group is dissociated from the cluster.[92] High redox potential Lc and BOx, with

redox potential up to 780 mV[76] and 670 mV[77] vs. NHE, respectively, can be used to create efficient biocathodes with current densities up to a few $mAcm^{-2}$.

Recent studies are developing procedures to minimize the ET distance between the active site of BOx and the electrode surface. The T1 Cu site is oriented towards the electrode surface utilizing bilirubin, the natural substrate, or molecular analogues. Later, the oriented enzyme is tethered to the electrode surface ensuring minimum active site-electrode distance. Results have shown that T1Cu orientation and tethering of the enzyme leads to improved enzyme-electrode communication, facilitating ET, reflected as increased current generation. [93]

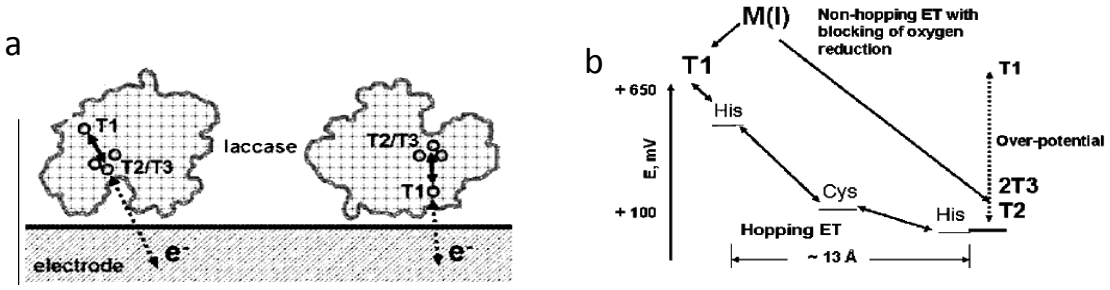

Figure 1.12. a) Laccase-electrode surface interaction, b) Intramolecular electron transfer in Laccase (*Ivnitski, D.; Atanassov, P. Electroanalysis, 2004, 16, 1182*)

The characteristics and interactions of the different components found in biological media must be considered when selecting enzymes for cathode design. Laccase has optimum activity in acidic media, and it is inhibited by chloride ions, whereas BOx is chloride-resistant and very active at neutral pH at the cost of having a slightly lower redox potential, namely 100 mV lower compared to Laccase.[94, 95] For EFCs intended to be used for biomedical devices, given the fact that the host's blood and sweat contain high chloride concentrations and shows a neutral pH, makes BOx the natural choice. However, as noted by Heller and his coworkers, deactivation of the BOx enzyme occurs in the presence of urate, a compound present in serum.[96, 97]Even

though BOx may present limitations for implantable applications, for extracorporeal biomedical applications, BOx could be feasibly employed.

Despite their similarity, these MCOs show different redox potentials. Theoretically, the potential difference is due to the absence of covalent bonds between copper and histidine groups, where the hydrogen bonds vary with the distance of the coordinating histidine groups affecting the tripeptide bridge and the coppers' stability in the intermediary structure. The redox properties of these oxidases were studied in order to gain an understanding of the changes on the conformation of the active site, and the arrangement of the monolayer enzyme immobilized on the electrode surface.

1.4.3. Bioelectrodes Materials

The development of new nanomaterials sets the foundation for the design of efficient and stable EFCs.[3, 98, 99] Different strategies have been developed to incorporate or immobilize enzymes on different nanostructured electrodes based on mesoporous materials, nanoparticles, nanotubes, and nanocomposites.[100] Ideally, electrodes should have a high electrical conductivity, provide stabilizing interactions with enzymes, have a high surface-to-volume ratio to allow for a high enzyme load, and contain sufficiently large pore size to facilitate efficient mass transport of fuel(s) and oxidant(s).[2, 14, 44, 84, 101]

Electrodes made from spectrographic graphite are attractive to use due to the low cost, naturally high porosity, and uncomplicated use of the material.[102] Electrodes with a high surface roughness can also be created through their modification with metal or carbon nanoparticles, such as gold nanoparticles (AuNPs)[103] or Ketjen black (KB)[104], respectively, and utilization of carbon nanotubes (CNTs)[105].

The development of composite carbon nanomaterials, such as single- and multi-wall CNTs (SWNTs and MWNTs, respectively) has had a large impact on the development of EFCs. CNTs have many attractive properties, such as high electrical conductivity, thermal, and chemical stability, as well as high mechanical strength, while displaying favorable interactions with enzymes.[44, 46, 106-109] CNT-based "bucky papers" are commercially available[109, 110] and other carbon-fiber papers, such as "Toray papers", have also been employed as an electrode material, displaying an enhanced ET due to their high conductivity and porosity.[48, 111] This research introduces the design of a novel enzyme-electrode-electrolyte interface intended to enhance electron transfer of bioelectrodes envisioned to be used in biomedical applications.

1.4.3.1. Carbon Nanotubes

Carbon nanotubes (CNTs) belong to the fullerenes structural group. The structure of a SWNT can be compared to the structure of a graphene sheet rolled into a cylinder along a (*m,n*) lattice vector in the plane (with diameter ~ 1nm and length/diameter ratio ~$132X10^6$/1).[109, 112, 113] The (*m,n*) vector indicates the two directions of the hexagonal ring lattice. The *n* and *m* indices determine the chirality and the conductive properties of the nanotube; the angle formed between the hexagonal rings and the tube axis determines the band gap that gives the structure its metal or semiconductor behavior (Figure 1.13). When *m*=0, the nanotube has a zig-zag configuration (Figure 1.13.a). When *n*=*m*, the nanotube has an armchair configuration, its structure is quasi-metallic (Figure 1.13.b). In any other *n,m* correlation, the nanotube has a chiral configuration and metallic behavior (Figure 1.13.c). In theory, a metallic SWNT is able to transport a current density approximate to $4x10^9$ Acm^{-2}.[114] The chemical bonding between the carbons of the

nanotube is composed of hybrid sp^2 bonds. CNTs form "ropes", they align themselves; this is due to Van der Waals (VdW) interactions between the orbitals of the grapheme structure.

The commercially available SWNTs are synthesized by Chemical Vapor Deposition (CVD). One of the CVD synthesis procedures use methane as a source of carbon and iron oxide nanoparticles or other metal catalysts supported on alumina as catalyst.[112] The synthesis is performed in a high temperature chamber (~1000ºC).

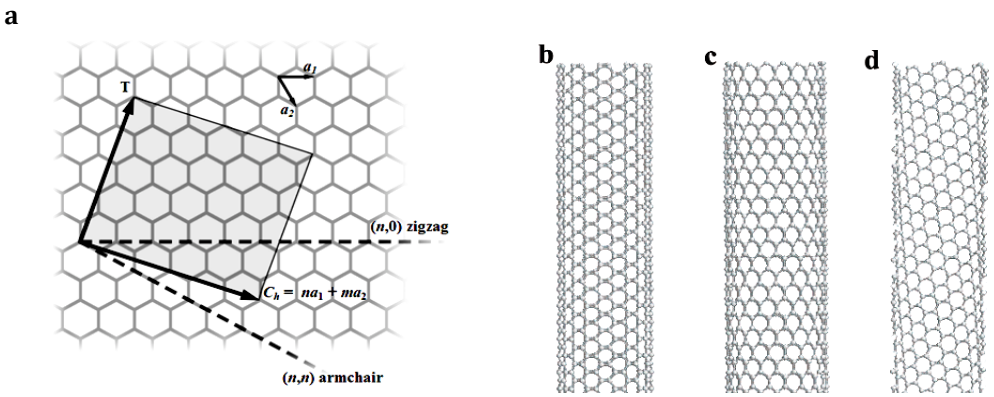

Figure 1.13. a) Schematic structure of a graphene sheet (the two basis vectors a_1 and a_2 are shown) and b) Armchair, c) zigzag, d) chiral configurations in a SWNT (Dai, H. *Acc. Chem.* Res. 2002, *35*, 1035).

MWNTs, similarly to SWNTs, are fullerenes species with structures similar to multiple rolled graphite sheets in cylindrical shapes. A MWNT consists of a structure with concentric tubes; it has a higher diameter and length than SWNTs. The distance between its layers is approximately 3.4 Å. Because of its size, the external curvature of a SWNT could be approximate 10º while a MWNT has a curvature ~ 67º when compared to an adjacent tangent. The conductivity observed in MWNTs is higher than SWNTs due to the interaction of concentric layers by sp^2 bonds, π-configuration, that make the electrons transfer easier. Also, the difference of curvature allows the MWNTs to be used for enzyme immobilization with the tethering agent

capable for π-π interaction. The research introduced here made use of MWNTs- based "bucky" paper composites for the bioelectrode design.

1.4.3.2. Toray Paper

Toray paper (TP) is a material with high electrical and thermal conductivity, high strength and permeability, and minimal electrochemical corrosion. This material is made from a combination of carbon fibers with Teflon polymer. The high surface area of the composite material has the characteristics needed to be used as a gas diffusion layer in fuel cell design; it was used in phosphoric acid fuel cells (PAPC), in polymer electrolyte fuel cells (PEFC) and is expected to be applied in other fuel and biofuel cell designs. Its manufacturer reports the material has very low resistivity ~80 mΩ in plane and ~4.7-5.8 mΩ through the plane.[115] The resistivity measurements vary according to the teflon content of the paper, which varies from 5% to 60% wt. The teflon percentage in the material also affects the gas permeability; the higher the percentage of the teflon in the composite the lower the gas permeability. In higher teflon percentage TP, the conductivity through the plane is not affected; this makes the material desirable to be used for enzymatic biofuel design. The high content of teflon makes the TP surface hydrophobic and could interact better with the enzymes that also have hydrophobic characteristics. The TP surface could provide better enzyme-material interaction and increase enzyme loading on the surface while an adsorption immobilization technique is applied.

1.4.3.3. Nonconductive Bioelectrode Design Materials

Operation *in vivo* or *in situ* compared to *in vitro* poses many additional difficulties. First, *in vivo* conditions can be harsh; the host's organism has an aggressive immune system in which BFCs will be subjected to a multitude of different proteins and cells present in the blood and

secreted fluids that will interact with the implanted or extracorporeal EFC.[116] Biocompatibility is a major issue for long-term utilization of the EFC. For example, EFCs placed into a blood vessel or over the skin tissue could be recognized by the body as a foreign element, which can trigger an inflammation reaction. Physiological fluids are also complex liquids containing a multitude of low-molecular-weight compounds, which can affect the performance of the BFC. In order to avoid this, the materials used in the BFC design should be bio-inert and biocompatible to preferably avoid triggering the host's immune system. In this research, poly(dimethy siloxane) (PDMS, Siglard ®) is used (Fig. 1.14) and manufacturer procedure for synthesis is used .

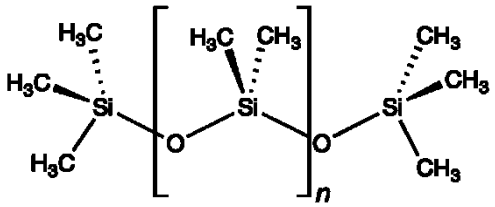

Figure 1.14. Poly(dimethyl siloxane) (PDMS)

1.4.3.4. EFC for Extracorporeal Application-Assembly of Bioelectrodes to Paper-Based 2D-Microfuidic System for Cell Design

A self maintained microfluidic system, driven by capillary flow is used in this project. Both bioelectrodes were assembled and characterized on a quasi-two dimensional microfluidic system fabricated from filter paper.[117-121] The device consisted of a specific 'fan'-shape device of a 2 cm × 9.5 cm rectangle appended to a 270°-circular section 15 cm in diameter (figure 1.15). This microfluidic system facilitates supplying the cell with fuel or electrolytic solution with no externally supplied energy.

Bioelectrodes were assembled to the upper part of a rectangular zone of the paper-'fan' (figure1.15.D). Lamination of anode was achieved with regular scotch tape and the cathode gas-

diffusion layer was exposed to air (figure1.15.D). Carbon yarn and carbon and silver inks were used to establish the connection of the electrodes to the potentiostat. The electrolyte flow was driven by capillary action maintained by the evaporation process on the semicircular section the device depicted in figure1.15.C. The volumetric flow rate was found by evaluating the parameter of the shape of the device, q (figure 1.15.B).[117-119] The quasi-two dimensional microfluidic system serves also as mechanical support and as an electrode separator medium.

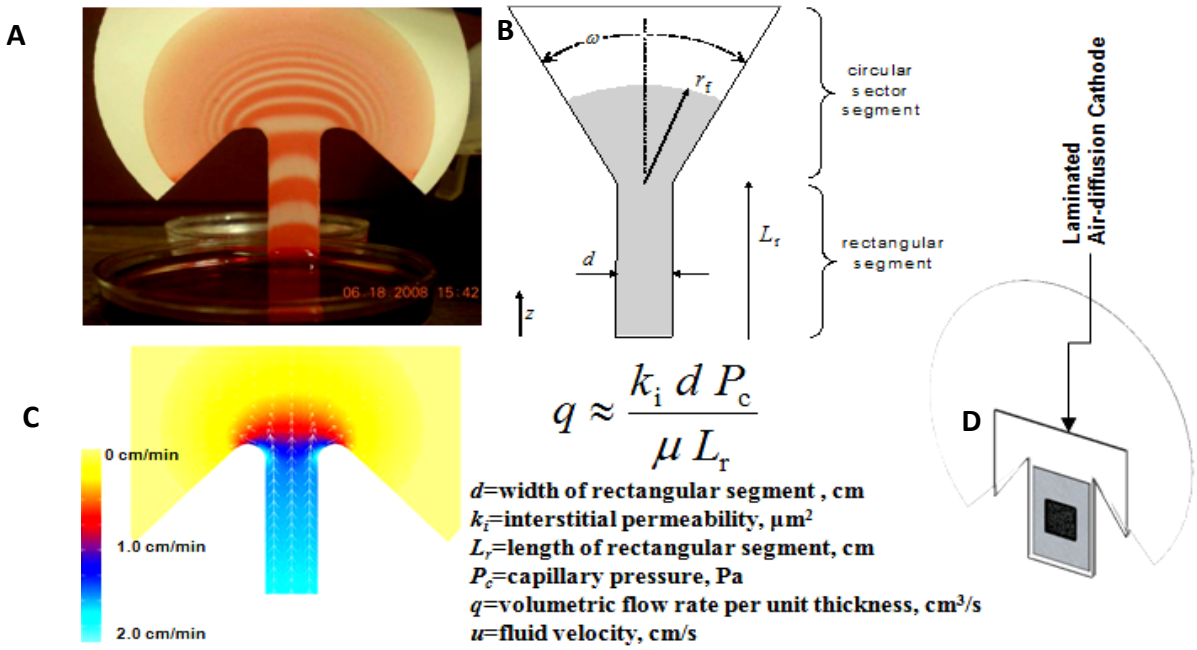

Figure 1.15. Paper-based microfluidic system. A) Image of experimental flow rate study; B) Schematic of fan and relevant parameters to determine volumetric flow rate, q; C) Computational simulation of flow rate driven by capillary action showing velocity of liquid flow; D) Schematic of gas-diffusional cathode assembled on a paper-based microfluidic system (*image source Mendez et al, Langmuir 2010, 26, 1380, and Bio-electrochemical Interface: The Case for Enzymatic Biofuel Cells, September 12, 2013 -Presentation, Prof. Plamen Atanassov, University of New Mexico*).

1.5. EFCs as Power Sources for Biomedical Devices

EFC devices that utilize glucose as biofuel are promising alternative power sources for BMDs. An example of an *ex-vivo* or extracorporeal application is the monitoring of analyte

concentration on the surface of the cornea; lachrymal fluids or tear fluids contain glucose levels in the range of 0.1-0.6 mM [122-124](among other compounds). Lachrymal fluids are accessible at the eye's surface and glucose depletion has apparently no effect on the cornea tissue.[103] The conversion of glucose to gluconic acid, with a two-electron transfer (ET) process, was demonstrated to be feasible and capable to satisfy energy demands for microdevices tha could be incorporated into a contact lens (figure 1.15).[125-127] Nicotinamide adenine dinucleotide (NAD^+)-dependent glucose dehydrogenase (GDH)-based anodes have been demonstrated to generate higher current than glucose oxidase-based anodes.[1, 46-48, 128] GDH system use NAD^+ cofactor as an electron receptor where reduction of NAD^+ is coupled with the glucose oxidation.[1, 30, 57, 74, 104] The development of reagentless bioanodes employing NAD^+/NADH-dependent dehydrogenases has been the area of study of researchers designing anodes for biosensor applications primarily.[129-131]The main challenges of these bioanodes are, first, that the regeneration of NAD^+ from NADH involves high overpotentials and, second, that NAD^+ should be present in the electrolyte in order to observe enzymatic conversion of the substrate. The first problem has been resolved by the utilization of methylene green (MG) as a mediator for the reaction.[58, 59, 132] MG, an azine, is electropolymerized on the SWCNT and MWCNT electrode material surface employing a protocol developed by Svoboda *et al.*[58] and transferred on SWCNT and MWCNT surfaces by Narvaez Villarrubia *et al.*[84, 133] Several approaches considered the integration of the cofactor to polymeric structures such as dextran[134], alginate[135], polyethylene glycol[136], chitosan[137], polyethyleneimine[130, 138], and entrapment in sol-gel using glycidoxypropyltrimethoxysilane[129, 131] as linker. Thus, the immobilization of the NAD^+/NADH-cofactor will lead to an improvement of the EFC design and will eliminate the need to add this

coenzyme during the normal performace of the EFC. In a contact lens application, the catalytic layer of the anode should be placed facing the cornea for better glucose collection.

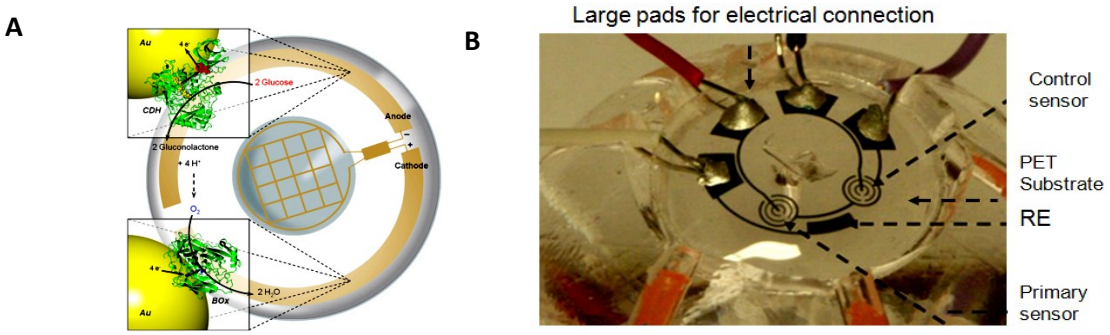

Figure 1.15. A) Schematic of Cellobiose dehydrogenase/Bilirubin oxidase EFC integrated in contact lens (M. Falk et al. Biosensors and Bioelectronics 2012, 37,38–45), B) Contact lens sensor tested for continous glucose monitoring on an eye-PDMS model (*H. Yao et al. J. Micromech. Microeng. 2012, 22 (075007), 1-10*).

The reduction of oxygen at the cathode surface has been shown achievable by bilirubin oxidase (BOx), a multicopper oxidase, generating water as bi-product.[91, 139] This enzymatic system can undergo a direct 4-electron transfer mechanism and has shown significant enzymes-carbon nanotube surface interaction that enhances electron transfer.[139-142] The development of passive air breathing cathodes has shown great advancement in dual-layered cathode designs for enhanced oxygen flow from air to the catalytic layer.[120, 140, 143, 144] An enzymatic fuel cell should be designed in a way to allow access of oxygen from air to avoid depleting oxygen from the tissue investigated; for example, an EFC operating on the cornea could lead to impairment of the vision if oxygen is depleted form its tissue.[103, 145-149] Thus, the state of the art technology on air-breathing cathode design should be transferred and adapted to the EFC-BMDs to avoid disrupting the physiological function of oxygen where the BMD is being used. For extracorporeal applications, the cathode would be exposed to the air but with its catalytic layer facing the inner matrix and the anode.

The catalytic layers of both electrodes must be engineered to stabilize the enzymatic systems on both electrodes and to enhance electron transfer and ionic/charge exchange between the active site of the enzymes, the electrode's surface and the electrolyte. Immobilization of the enzymatic systems can be achieved by utilizing silica-gel and chitosan as entrapment matrices to preserve the stability of the active 3D-structure of the enzymatic systems and ensure the close proximity of the active site of the enzymes to the electrode surface while allowing particle and fluid exchange with the electrolytic solution. Both, silica-gel[48, 129, 140] and chitosan/CNTs[49, 82, 150, 151] matrices have been studied previously resulting in improved performance and prolonging the lifetime of the enzymes in storage.

Additionally, the biocompatibility of the electrode's materials, circuitry and external ensemble material of the device has also to be considered. The material encapsulating the EFC should be biocompatible to avoid triggering the host's immune system. The materials considered in this research, polydimethylsiloxane (PDMS) [152-155], consisting of three-dimensional , amorphous, polymeric matrices, have been extensively used in the contact lens industry and are proven to be biocompatible for this application. These materials consist of a silicone-based hydrogel that confers the contact lens with efficient oxygen permeability, high wettability, resistance to biofilm formation (observed in non-silicon based hydrogels) conferring enduring lens comfort.[24] Therefore, PDMS can be integrated into EFC designs for extracorporeal biomedical applications.

From an electrode design perspective, the materials chosen should enhance electrical conductivity, provide stabilizing interactions with the oxidoreductase enzymes, have a high surface-to-volume ratio to allow high enzyme loading, and contain a sufficiently large pore size to facilitate efficient mass transport of glucose and oxygen.[125, 126, 156] Carbon nanotubes are

materials with attractive properties (high electrical conductivity, thermal and chemical stability, and mechanical strength) and demonstrate efficient interactions with enzymes.[127, 157-160] Moreover, multi-walled carbon nanotubes (MWNTs)-based 'bucky papers' are commercially available [161, 162] and have shown enhanced electron transfer due to their high conductivity and porosity.[163, 164] Although the carbon nanotube-based materials might not be biocompatible, the fuel cell can be designed to fulfill biocompatibility requirements for the intended biomedical application.

1.6. Statement and Objectives of the Research

This research focused on the development of a glucose/oxygen enzymatic biofuel cell integrated into a biocompatible polymer for electrical power generation for potential biomedical applications. This research introduces new concepts and innovative ideas aimed to optimize power generation from biological media in physiological conditions; at the same time significant challenges are faced in the EFC design in order to make this technology transferable to biomedical applications:

- Minimize losses, to stabilize the enzymatic system
- Enhance electron transfer
- Optimize the design within biocompatible polymeric matrices

The integration of the glucose/oxygen biofuel cell employing glucose dehydrogenase as an oxidation system into a biocompatible material (found in contact lens devices) to our knowledge is a novel idea.

Considering the requirements and concepts stated above, this research had the objective to improve the performance of glucose dehydroganase (GDH) and bilirubin oxidase (BOx) oxidoreductase enzymes outside their natural environment and to preserve their functional

structure in polymeric matrices conformed by silica-gel and chitosan. This research aimed to enhance the catalytic activity of these enzymes when attached to the surface of carbon nanomaterial-based electrodes by applying immobilization techniques that allow for the preservation of the active three-dimensional structure of the enzymes. Data collected shows that the enzymes remain stable for long periods of time in storage at 4ºC, and under continuous operation in physiological conditions.

Based on the current stage of the EFCs development and the requirements established for implantable power sources, the following objectives were placed:

- **Objective 1**: Minimize the inherent limitations of the bioanodic systems and improve the bioanode design to a reagentless GDH-based anode.
- **Objective 2:** Enhance enzyme stability on the anode surface by entrapment procedures that also promote enhancement of electron transfer at the electrode surface-enzyme-electrolytic solution interface.
- **Objective 3:** Minimize the inherent limitations of the biocathodic system and develop gas-diffusion electrodes based on passive flow of oxygen from air to the cathode catalytic layer.
- **Objective 4:** Enhance enzyme stability on the cathode surface through entrapment procedures that also promote the increase of electron transfer rate at the three-phase interface (electrode surface-enzyme-electrolytic solution-oxygen interface).
- **Objective 5**: Integrate the bio-electrodes into a biocompatible polymeric matrix.

Minimizing the kinetic, conductive and mass transport limitations would improve the performance of the anode. Increased kinetics can be achieved by improving the activity of

the catalytic layer by increasing the surface area, increasing enzyme loading and immobilizing the enzymes on the electrode surface for enhanced electron transfer. Decrease of the ohmic losses can be achieved through the integration of highly conductive nanomaterials. At this stage, mass transport losses can be minimized by employing highly porous material at the catalytic layer as entrapment matrices and a microfluidic system that ensures the transport of biofuel to the active site. In order to decrease ohmic limitations, optimum electrodes materials need to be applied.

In this research, the designs developed integrate composite carbon nanomaterials, "bucky" papers, as electrode materials that confer the catalytic layer with increased surface area, consisting of hierarchically-ordered nanostructures, with controlled surface chemistry. BEP and CMN-grade bucky papers were studied for current output performance employing lactate, alcohol and glucose dehydrogenases as explained in chapter 3.

Both non-reagentless and reagentless bioanode designs were developed (chapter 4). The latter was characterized as having the NAD^+/NADH-tethered on the MWNTs-based bucky paper through the utilization of PBSE by π-π interaction, while the GDH enzyme is entrapped within a CNTs/Chitosan and CNTs/Chitosan/silica-gel 3D-matrices. The bioanode was integrated and evaluated into a PDMS matrix showing encouraging results for potential BMD applications (chapter 7).

A gas-diffusional cathode, employing bilirubin oxidase (BOx) immobilized via silica gel on a complex matrix composed of carbon nanotubes (CNT) synthesized in Toray Paper, was developed. In order to analyze the behavior of the BOx-on carbon-composite nanomaterials, first an air-breathing dual-layered design was developed to characterize the system under

passive-air flow conditions in a paper-based 2D-microfluidic system; the stabilization of the system was investigated for 6 months (chapter 5).

The second approach consisted of integrating the BOX enzymatic system on a bucky paper surface; the system was characterized in a submerged electrolytic cell configuration. The goal was to stabilize the system employing a tethering agent on a 3D CNTs network and a silica matrix for enzyme entrapment. This system was analyzed for a period of 12 months (chapter 6).

The resulting information was employed to adapt the cathode to the third approach for the analysis of the behavior of BOx-on carbon-composite nanomaterials. The integration of the bucky paper-based electrode onto the PDMS-based polymeric matrices at passive-air flow conditions assembled to a paper-based microfluidic system was achieved and analyzed per chapter 7.

Electrochemical characterization of the electrodes surface was performed for the three different anode and cathode designs descrived above. Further physical characterization was carried out by scan electron microscopy and X-ray photoelectron spectroscopy as well. Electrochemical characterization on bioelectrodes individually and assembled to a 2D-microfluidic system was the focus of this research. The utilization of the biocompatible PDMS matrix was achieved for both bioelectrodes.

The concepts introduced and tested in this research, as well as the results obtained, show great potential for the development of enzymatic biofuel cell systems capable of functioning in foreign surroundings for prolonged periods of time and within physiological conditions. Later, this technology could be integrated into designs destined for extracorporeal and implantable applications for power generation of biomedical devices.

Chapter 2. Experimental Methods - Physical and Electrochemical Characterization Techniques

Several experimental procedures were used in this research in order to synthesize nanocomposite material and characterize the respective catalytic layers for bioanodes and biocathodes. Electrochemical techniques were applied in order to engineer a design of a catalytic layer and to characterize the electrode surface: Open Circuit Voltage measurements (OCV), Cyclic Voltammetry (CV), Chronoamperometry and Chronopotentiometry. Additional physical characterization methods, such as Scanning Electron Microscopy (SEM), Energy Disperse Spectroscopy (EDS) and Transmission Electron Microscopy (TEM) techniques, were used in order to further physically characterize the electrodes' surface.

2.1. Electrochemical Techniques for Electrodes Characterization

The configuration of the electrolytic cell chosen was a tree-electrodes cell, which consists of working, reference and counter electrodes. The working electrode was the electrode to be evaluated. The reference electrode is an electrode with known potential against which the working electrode is compared. The counter electrode is an auxiliary electrode, which acts as an electron source for a working cathode, or an electron sink for a working anode. This helps to mitigate limiting effects of electron transfer to the working electrodes, allowing for better electrochemical measurements.

2.1.1. Open Circuit Potential

This technique is based on the measurement of the potential at zero current or at open circuit. The potential difference between the analyzed electrode and the potentiostat terminal is measured. This measurement gives information about the thermodynamics of the electrolytic cell, allowing for better understanding of the thermodynamic potential of the enzyme-surface electrode. This method does not provide any information regarding kinetics and mass and electron transport of the biofuel cell.

2.1.2. Cyclic Voltammetry

This technique provides information on the reversibility, kinetics of the electron transfer, and redox potential of the electroactive species. This is performed by linearly sweeping back and forth the potential of the working electrode within a potential range via a triangular wave form (Figure 2.1.a). Herein, the current is measured against the potential while a scan rate potential is applied. For an oxidoreduction reaction, the cathodic potential peak, E_{pc}, and cathodic current, i_{pc}, correspond to the reduction of the species, and are shown at negative sweeps ($Ox + n\ e^-$ ---> Red) (Figure 2.1.b). In the reverse direction, the anodic potential peak, E_{pa}, and the anodic current, i_{pa}, are shown at positive sweeps and correspond to the re-oxidation of the species (Red --> $Ox + n\ e^-$) (Figure 2.1.b). Finally, the redox potential of the species (Red/Ox), E^o, can be obtained from the equation stated early: $E^o=(E_a+E_c)/2$.

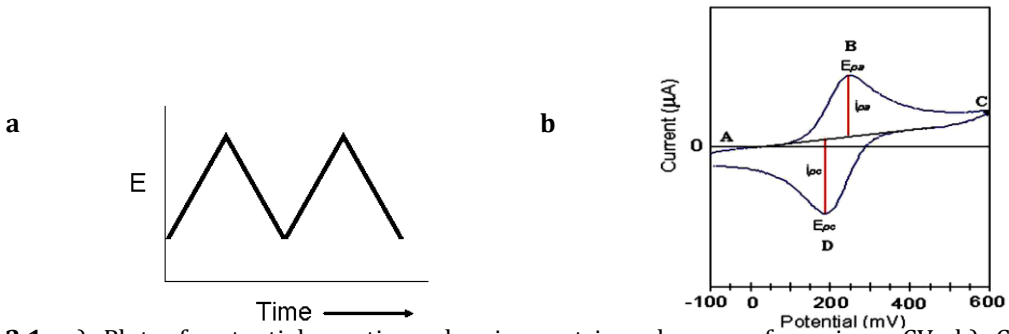

Figure 2.1. a) Plot of potential vs. time showing a triangular waveform in a CV, b) Cyclic Voltammogram for a reversible redox reaction

In this research, CVs are performed to electrochemically evaluate the electrodes and to immobilize the mediator for NADH oxidation (MG) by physical adsorption and electropolymerization of the monomer to PMG on the SWNTs electrode surface. Also, the cathode performance is tested using this procedure.

2.1.3. Chronoamperometry

Chronoamperometry is a potentiostatic technique that measures the faradic current generated as a function of time while a stepping potential is applied (Figure 2.2.a). The faradic current (as a function of time) shows the behavior of the charging double layer of the electrode at the applied potential and the exponential decay due to the electron transfer (Figure 2.2.b).

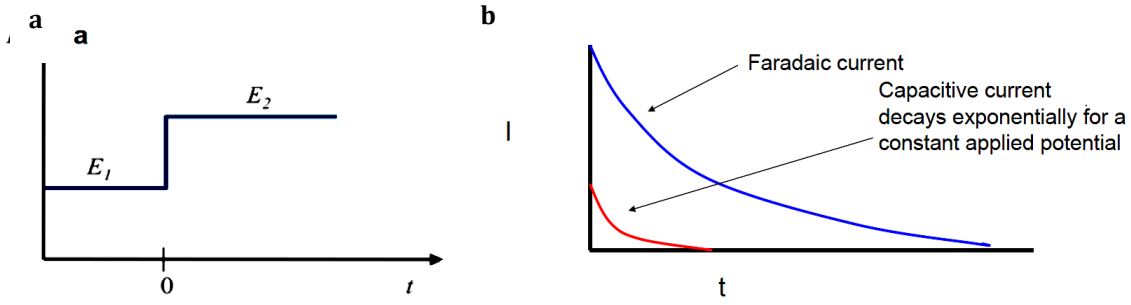

Figure 2.2. a) Stepped potential in chronoamperometry, b) Faradic current and exponential decay of current as a function of time.

Chronoamperometry helps to relate the working potential of the working electrode while it approaches a constant current density for changing stepping potentials (Figure 2.3.a). In order to determine the potential at which the working electrode is capable of having the best performance, stepping potentials are applied and the quasi-steady state current is measured. This process is followed until no change of current is observed for different stepping potentials; then, the data can be plotted in a **potentiostatic polarization curve**, current vs. potential (Figure 2.3.a). The working potential of the electrode is the potential at which the current starts its steady state behavior; that is, the current approaches a plateau.

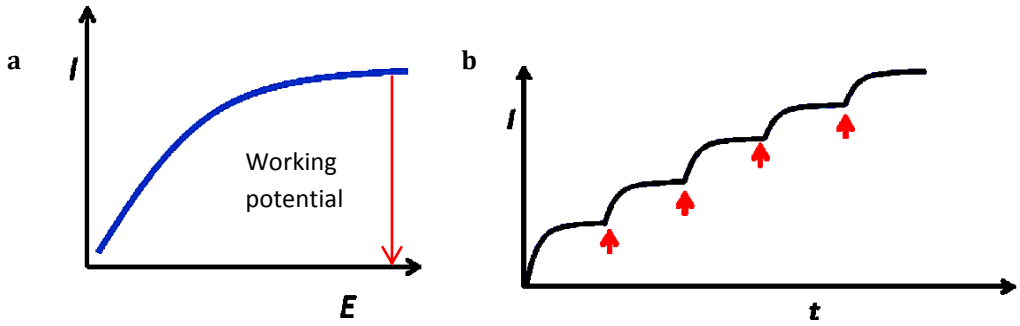

Figure 2.3. a) Potenstiostatic Polaryzation Curve, working potential of the electrode is found when current approaches steady state behavior, b) Chrnoamperometric curve, current vs. time, at a constant potential, the change in current measured is due to the change of the concentration of the reactant in the cell by aliquots added.

Furthermore, the chronoamperometric measurements of an oxidoreduction reaction are used to characterize the process with respect to the analyzed species. Considering an enzymatic reaction as the process and the substrate as the analyzed species, it is possible to relate the behavior of the enzyme to the concentration of the substrate in the electrolytic cell. For this, the current generated in the redox process at a constant applied potential is monitored. In the cell, the current is measured while aliquots of the substrate are added producing a increase in the current generated (Figure 2.3.b). This technique can be further used to characterize the behavior of an

enzyme with its substrate and its change in concentration. This technique more accurately provides information regarding the performance of the cell in real operational conditions

Chronoamperometry is also the procedure that allows us to monitor the current generation at the anode as a function of the concentration to determine the Michaelis-Menten kinetic parameters; this is accomplished considering that the glucose dehydrogenase enzyme shows one-site binding process. The Michaelis-Menten equation for the rate of the enzymatic reaction for a one-substrate enzyme catalyzed reaction is shown below:

$$v = k_{cat} E \frac{S}{K_M + S} \qquad \text{Eq.17}$$

In eq. 2.1, v is the biocatalytic constant or turnover number of substrate molecules converted to product per enzyme molecule per second, E is the enzyme concentration, k_{cat} is the catalytic constant, S is the substrate concentration, and K_M is the Michaelis-Menten constant. For the maximum rate of reaction, $V_{max}=k_{cat}E$. However, when monitoring the current generation of enzymes showing one-site binding mechanism, the current generated is $i = v$ and $I_{max}= k_{cat} E$.

2.1.4. Chronopotentiometry

In this technique, a controlled current is applied to the cell and the potential of the working electrode is monitored as a function of time. The Galvanostatic potential is measured when the applied current is constant (Figure 2.4.a). In order to sustain the constant current applied, changes in potential to the working electrode are introduced. In a redox couple, *Red/Ox,* as *Red* species moves from the electrode surface, the *Ox* species moves toward the electrode surface, where it is reduced. The space where the species travel is called the *transition region* and the time they take to travel this space is called the *transition time*. This technique is used to

determine the electron transfer rate of the oxidoreduction reaction occurring on the electrode surface. By plotting the potential measured against the applied current, the **galvanostatic polarization curve** is obtained (Figure 2.4.a).

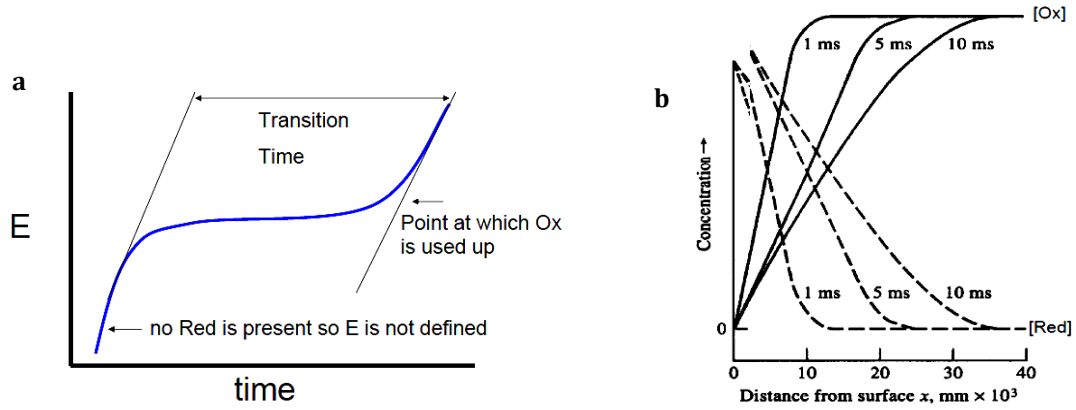

Figure 2.4. a) Chronopotentiometric curve, potential as a function of time at a constant applied current, b) Red and Ox species concentration with respect to the distance to the working electrode surface

2.2. Physical Surface Characterization Techniques

2.2.1. Scanning Electron Microscopy (SEM)

SEM is a technique that allows the imaging of the surface of a material at a micro and nanometer scale. A negative potential is applied to a tungsten wire generating an electric field; this electric field is then concentrated on the tip of the tungsten wire and an accelerated electron beam is emitted. The SEM uses magnetic fields to focus the electron beam toward the sample. The beam of accelerated electrons carries energy when it collides with the surface of the material to be analyzed. As an interaction of beam-surface is produced, the electrons are decelerated and energy is dissipated; as a result, secondary electrons, backscattered electrons and x-rays, visible light and heat emissions are observed. Secondary and backscattered electrons are detected and used to study the topology and morphology of the surface for SEM imaging.

2.2.2. Energy Disperse Spectroscopy (EDS)

The EDS characterization technique was used to analyze the chemical composition of materials. As stated above, for the SEM technology, when the accelerated electrons beam hit the surface of the sample, an emission of X-ray was produced. This emission is due to the inelastic collisions of the electron beam with electrons in the shell of the atoms of the sample; X-ray photons are generated due to the specific energy of the external orbital of the atoms that compose the sample. X-ray photons have an energy that corresponds to the energy difference between the levels of the electrons involved in the process. Those photons are characteristic of each atom and have a defined wavelength of emission. These X-ray emissions are used to identify the atomic elements present in the sample. This technique is used to characterize qualitatively and quantitatively the elemental composition of the sample.

2.2.3. X-Ray Photoelectron Spectroscopy (XPS)

XPS allows the determination of elemental and chemical composition of the sample at a depth of 10nm from the surface. The sample is irradiated with an X-ray beam of primary energy ($h\nu$) which produces the release of photoelectrons with a characteristic binding energy (E_b).

$$E_b = h\nu - E_k - \varphi \qquad \text{Eq. 18}$$

This binding energy (E_b) is specific to the element and chemical bond from where it was ejected. The photoelectron, when ejected, travels with a kinetic energy (E_k) correlated to the primary photon energy ($h\nu$) and energy characteristic of the instrument (φ), eq.2.1. Then, the ejected photoelectron can be analyzed in vacuum conditions and a spectrum characteristic is generated which correlates to the binding energies respective to the photoelectron in the electronic

configuration of the element in the molecular structure. This procedure can be used to effectively quantify the amount of enzyme or other molecular components on the bioelectrodes' surface.

Chapter 3. Biofuel Cell Anodes Integrating NAD^+-Dependent Enzymes and Multi-walled Carbon Nanotube Papers

3.1. Introduction.

Enzymatic biofuel cells are power-source devices that make use of renewable biofuels to generate electric energy. Several enzymatic biofuel cell systems do not utilize a proton exchange membrane to separate the compartments due to the specificity of the enzymes,[1, 2, 4] and oxidoreductive processes can be developed at atmospheric pressure and temperature, contrary to conventional fuel cells. An efficient enzymatic biofuel cell design has to minimize inherent limitations. These are kinetic limitation on the catalytic layer, ohmic limitation due to resistivity of materials and the electrolytic solutions in the system, and mass transport limitation due to restrained mass transport of the biofuel toward the enzymatic-catalytic layer.[2, 121, 142] Extensive research has been performed to develop an enzymatic biofuel cell that can power small portable devices and implantable devices for biomedical applications.[1, 15, 103, 165]

Herein, the minimization of the aforementioned losses is approached by designing a novel nanoarchitecture of the enzymatic catalytic layer, circuitry and the microfluidic system and increase in current density are achieved. Kinetic losses are minimized by increasing the loading and stabilizing the enzymatic structure on a high surface-area to volume ratio nanostructured material, a MWNTs- based buckeye paper (BEP). The catalytic activity of the 3D-enzymatic structures adopted within the MWNT-chitosan nanoarchitectured matrix on the BEP surface toward biofuel oxidation can be electrochemically evaluated. Nicotine adenine dinucleotide (NAD^+/NADH)-dependent enzymes [74] lactate, alcohol and glucose dehydrogenases (LDH, ADH and GDH respectively) were electrochemically evaluated and compared. Enzymes were

physisorbed and entrapped in novel nanostructured architecture, a highly conductive 3D-high surface area-porous polymeric chitosan-CNTs mixture on the BEP surface by procedure previously used [82, 150, 151](figure 3.1). The oxidative activity of dehydrogenases is coupled to the reduction of NAD^+ to NADH.[57, 62] NAD^+ is made available through the oxidation of NADH employing MG polymerized on the electrode surface (PMG).[58-61, 71, 84] Overcoming the overpotential of NADH oxidation using PMG as mediator perpetuates the cyclic reaction overtime, making the dehydrogenases kinetically active and the anode design feasible to be applied in fuel cell assembly.

In order to minimize the ohmic losses, the electrode surface optimization needs to satisfy various criteria. The criteria are: high electrical conductivity, significant attractive interactions with enzymes, high surface area-to-volume ratio, and a surface with sufficiently large pore size to facilitate mass transport.[2, 3, 14] MWNTs accomplish the criteria due to their high electrical conductivity, mechanical strength and thermal and chemical stability.[44, 106, 112, 113] Their small diameters confer them with both high surface-to-volume ratios and favorable interactions with enzymes of comparable size. Composite materials integrating MWNTs have large pore sizes that facilitate mass transport to the catalytic layer. Previous research has demonstrated successful enzyme immobilization and direct electron transfer (DET) on MWNTs.[46] The properties of MWNTs make them feasible for engineering bioelectrode materials with hierarchically-ordered carbon nanostructures, controlled surface chemistry and efficient enzyme interaction for enhanced ET that minimize ohmic losses.

To overcome the mass transport losses, an efficient microfluidic system needs to be employed. A Paper-based quasi-2D system driven by capillary action[119, 121] assures the transport of the substrate toward the catalytic layer while minimizing applied energy to drive the flow.

Efficient mass transport can be achieved by relying on a continuous pump of the biofuel solution by a capillary-driven flow maintained by the system when it approaches a liquid-vapor equilibrium.

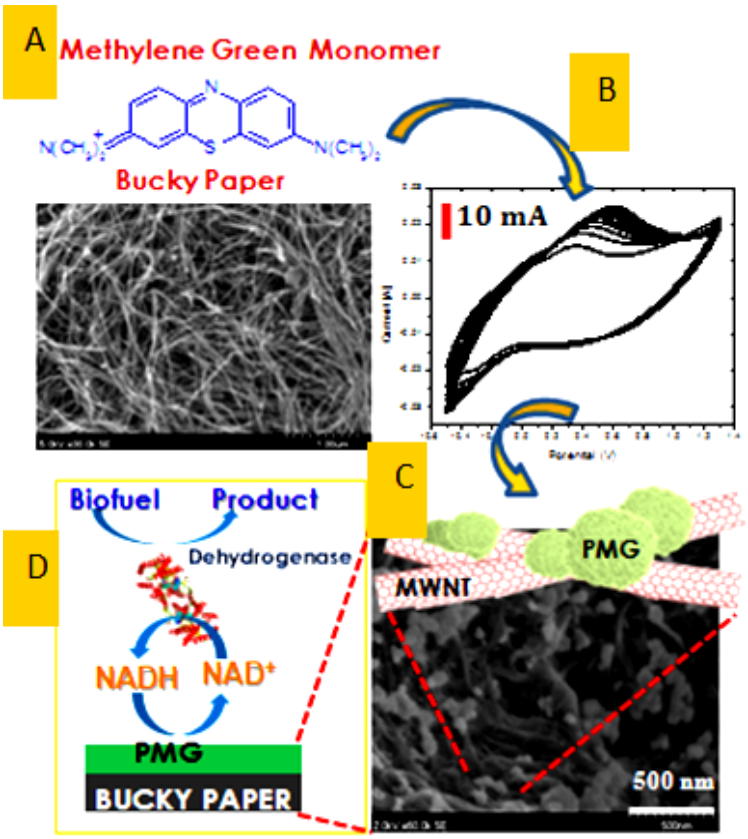

Figure 3.1. Glucose dehydrogenase/ multi-walled carbon nanotube (MWNTs) paper – based anode. A) plain MWNTs paper, B) methylele green (PMG) catalyst polymerized by electrochemical procedures, C) image in scan electron microscope of the anode surface showing the formation of the catalyst (PMG), D) scheme of the oxidative reaction of glucose promoted by the glucose GDH which uses NAD^+/NADH cofactor (reaction takes place on the anode surface where the PMG is a catalyst for the oxidation of NADH to NAD^+)

This study evaluates and compares the electrochemical performance of LDH, ADH and GDH 3D-structures adopted within the 3D MWNTs-Chitosan matrix on the BEP surface of the bioanodes. The bioanode design is easily reproducible and feasible to be used in a true dehydrogenase-based biofuel cell where the biofuel flows in and out through the system rather than being static in a battery-like fuel cell commonly used. The structure of GDH enzyme shows

higher catalytic activity toward glucose oxidation within the carbonic nanostructured on BEP compared to the ADH and LDH catalytic activity on their respective biofuels.

3.2. Experimental Methods

3.2.1. Apparatus

The electrochemical experiments were performed in a three-electrode cell by conventional potentiostat: Gamry Reference 600 Pontentiostat/Galvanostat. All potentials are reported vs. Ag/AgCl (CH Instruments Inc. Cat. CHI111), using Pt (0.127 mm and purity 99.9% Alfa-Aesar Cat. 10282) as counter electrode. The material characterization was performed using a scanning electronic Hitachi microscope (S-5200) equipped with an energy dispersive spectrometer (EDS).

3.2.2. Chemicals

Buckeye Paper (BEP) was obtained from Buckeye Composites Inc. (Kettering, OH) and had an average thickness of 15-250 μm and a purity of ~100% MWNTs. Isopropanol (purity >99%), monobasic and dibasic sodium phosphates were obtained from EMD Chemicals Inc. Phosphates were used to prepare pH 7 and pH 7.5 buffer (KPB) stock solutions. Methylene Green (MG) Zinc Chloride double salt (purity >99%, from Fluka Cat. 66870) and KNO_3 from EMD Chemicals Inc. were used to make a MG growing solution in PB of pH7. NAD^+ (purity ~98%, Fluka Cat. 43407). D(+)-Glucose (purity >99.5%), Lyophilized Glucose Dehydrogenase (GDH) from *Pseudomonas sp.* (272 U/mg activity, Cat. 19359), Lyophilized Lactic Dehydrogenase (LDH) powder from *Lactobacillus leichmanii* (260.71 U/mg activity, Cat. L3888), Crystallized and Lyophilized Alcohol Dehydrogenase (ADH) powder from *Bakers Yeast* (340 U/mg activity, Cat. A3263) and Sodium DL-Lactate solution, syrup 60 % (w/w) were

obtained from Sigma Aldrich (St. Louis, MO). Koptec 200 Proof Ethanol was from VWR (King of Prussia, PA).

3.2.3. Electrode Design

For each anode, a rectangular piece of 3.7 cm^2 (1.7cm x 2.17 cm) with a tail of 1.5 cm length and 0.6 cm width of BEP was cut (connected to the potentiostast) and later washed with IPA and. MG was polymerized on the surface of the BEP by electrochemical deposition by cyclic voltammetry (10 cyclic) at a scan rate of 50 mV/s within -0.5 V to 1.3 V. The MG growing solution consisted of 10 mL 0.5mM MG and 0.1M KNO_3 in 50mM PB at pH 7 where oxygen was depleted by bubbling nitrogen. After PMG deposition, 3 mg of enzyme was dissolved in 150 µL of 95% Chitosan /5% MWNTs mixture (1mg enzyme/50 µL Chitosan-MWNTs ratio), deposited on the BEP-MG surface and the electrode was stored overnight at 4ºC. GDH, ADH and LDH were utilized to fabricate the BEP-MG-GDH, BEP-MG-ADH and BEP-MG-LDH anodes, respectively.

3.2.4. Open Circuit Potential

The anodic potentials were monitored against time at zero applied current density during 1½ hours and 15 hours overnight (not shown) in both absence (blank) and presence of the respective substrates. The blank electrolytic solution was 1 mM NAD^+, 0.1M KCl in 0.1M PB at pH 7.5. In presence of the substrate, the electrolytic solution contained 0.1M biofuel to be evaluated. The OCP was measured in the electrolytic cell as well as the half fan cell. Fan cell setup consisted in laminating the working bioanode on the filter paper (catalytic layer facing the paper), and the Pt-counter on the opposite face (setup transferred from previous study on the cathode[84, 120, 121]).

3.2.5. Cyclic Voltammetry

The oxidation potential of each substrate by the respective enzyme was found by cyclic voltammetry (CV). The CVs were taken at 10 mV/s of scan rate in the potential range of -0.4 V to 0.8 V for the GDH-anode, and -0.8V to 0.8 V for LDH and ADH-based anodes. CVs were measured in the electrolytic cell.

3.2.6. Michaelis-Menten Analysis

The catalytic activity of the dehydrogenase was evaluated by the Michaelis-Menten analysis. The electric currents generated by the anodes - when their substrates were added in solution - were monitored as a function of time at -50 mV of constant applied potential. Initially, each anode was submerged in the blank solution. Later, aliquots of the respective substrate were sequentially added every 400 seconds to reach a 0.1M concentration in a final volume of 15 ml. In the case of BEP-MG-GDH, the substrate source was a 1M glucose solution; for BEP-MG-ADH, the substrate was 17 M ethanol; and for BEP-MG-LDH, the substrate was 1M lactate. Michaelis-Menten curves were obtained by plotting the current density recorded against the substrate concentration after the system approached a steady state. The Michaelis-Menten kinetic parameters were found through a computational analysis of the curves assuming the enzymes work through a one-site binding mechanism.

3.2.7. Polarization Curves in the Electrolytic Cell

By chronoamperometry, the current was recorded at different stepped potentials departing from the OCP value up to 0.35 V with 50 mV increments (every step approached steady state and consisted of 300 seconds). Currents were plotted as a function of the applied potentials to generate the polarization curves.

3.2.8. Stabilization Study of BEP-MG-GDH Anode

The stability of the GDH enzyme within the Chitosan-MWNTs matrix on the BEP was analyzed. Simultaneously, BEP-MG-GDH bioanodes were made and stored for 30 days at 4ºC in 'dry' conditions. Chronoamperometric measurements were taken daily during the first five days and later at different periods of time between each measurement.

3.3. Results

Thermodynamics of the catalytic layer of the anodes or the interaction energy of the particles within the system were analyzed by OCP curves. The OCP measurements were performed on the BEP (Figure 3.2.A), BEP-MG (Figure3.2.B), BEP-MG-ADH and BEP-MG-LDH (both not shown) and BEP-MG-GDH (Figure 3.2.C) in the absence and in the presence of a substrate. The BEP-MG-GDH bioanode shows a decrease of the OCP from ~0.03 V in the absence of substrate to -0.18 V in the presence of the substrate, showing the interaction of GDH-structure with its substrate on the anode surface is thermodynamically favorable toward the generation of products from the glucose oxidation reaction.

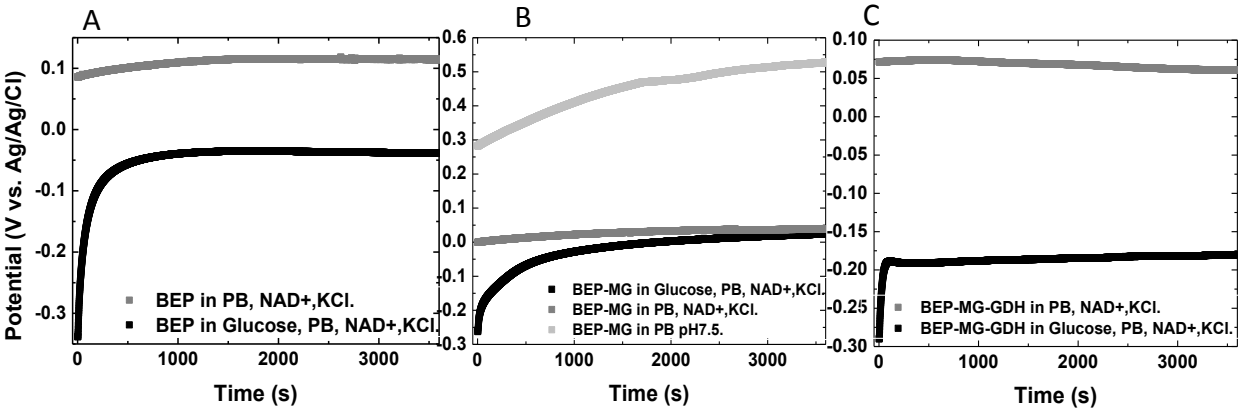

Figure 3.2. A) Plain BEP in blank 2 solution OCP~ 0.11 V (grey line) and 0.1M glucose OCP of -0.042 V(black line), B) BEP-MG in blank 1 OCP ~ 0.56 V (light grey line), in blank 2 solution OCP~ 0.45V (grey line) and 0.1M glucose OCP of 0.36 V (black line), C) BEP-MG-GDH in blank 2 solution OCP of 0.06 V (grey line) and BEP-MG-GDH in 0.1M glucose OCP of -0.18 V (black curve). BEP-MG-GDH shows the most thermodynamically favorable OCP in presence of its substrate compared to BEP-MG-ADH and BEP-MG-LDH (not shown)

Cyclic voltammertries show GDH enzyme have the best performance in the nanostructured matrix of the catalytic layer of the bioanode (Figure 3.4). The oxidation peak for glucose is shown at 0.22 V with a current of approximately 0.033 A (~33 mA) for the 3.7 cm^2 anode (full line); in the absence of the substrate, there is no significant electrochemical process observed (dotted line). Similarly, ADH shows oxidation peaks at 0 V and 0.5V with a current of 0.02 A (full line). LDH shows oxidation peaks at 0.2V with 0.008 A of current (full line).

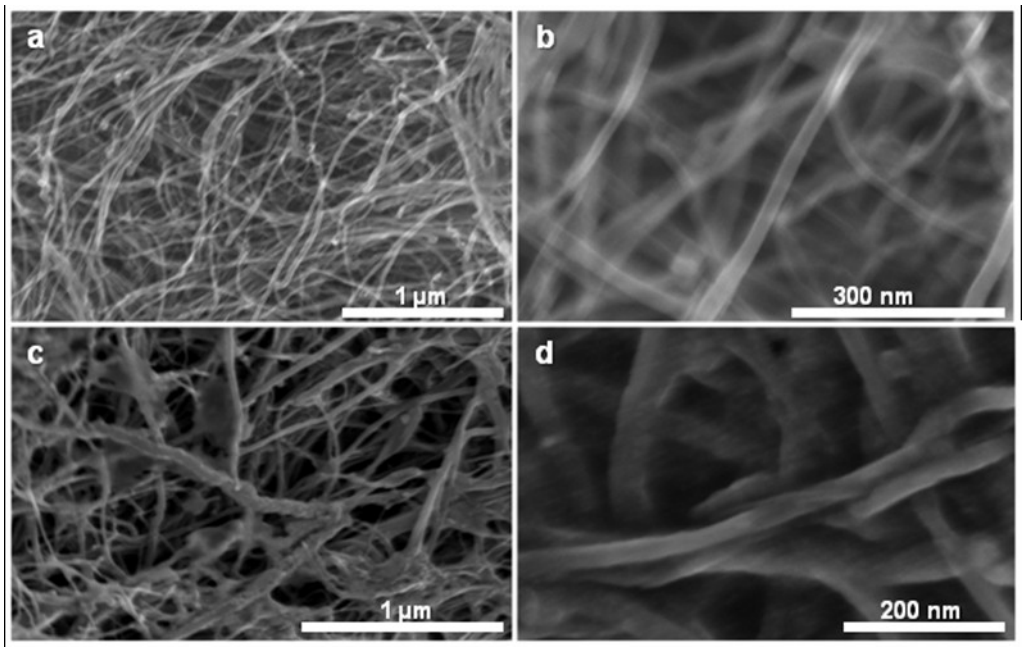

Figure 3.3. a) and b) Plain BEP. c) and d) BEP with MG and GDH in Chitosan-CNTs matrix.

Additionally, the kinetic Michaelis-Menten study confirms the GDH enzyme is the more active enzyme in the design proposed in this research (Figure 3.5.A). Under similar conditions, the kinetic parameters obtained for GDH overpass those shown by LDH and ADH. GDH shows a I_{Max} = 3.382 ± 0.180 $mA.cm^{-2}$ and K_M= 17.5 ± 3.1 mM while ADH show a 226.6 ± 10.1 $\mu A.cm^{-2}$, K_M = 16.0 ± 2.5 mM and LDH show a I_{Max}= 53.4 ± 5.1 $\mu A.cm^{-2}$ and K_M = 6.6 ± 3.3 mM. The kinetics of the catalytic layer of the GDH-based bioanode is increased 14 times with

respect to the ADH-based anode and increased 63 times with respect to the LDH-based bioanode at 50mV. GDH enzyme shows highly active kinetics toward the oxidation of glucose. This is reflected by the enhanced ET between the active site of the enzyme and the carbon nanostructured electrode demonstrated as an increase in the current generated.

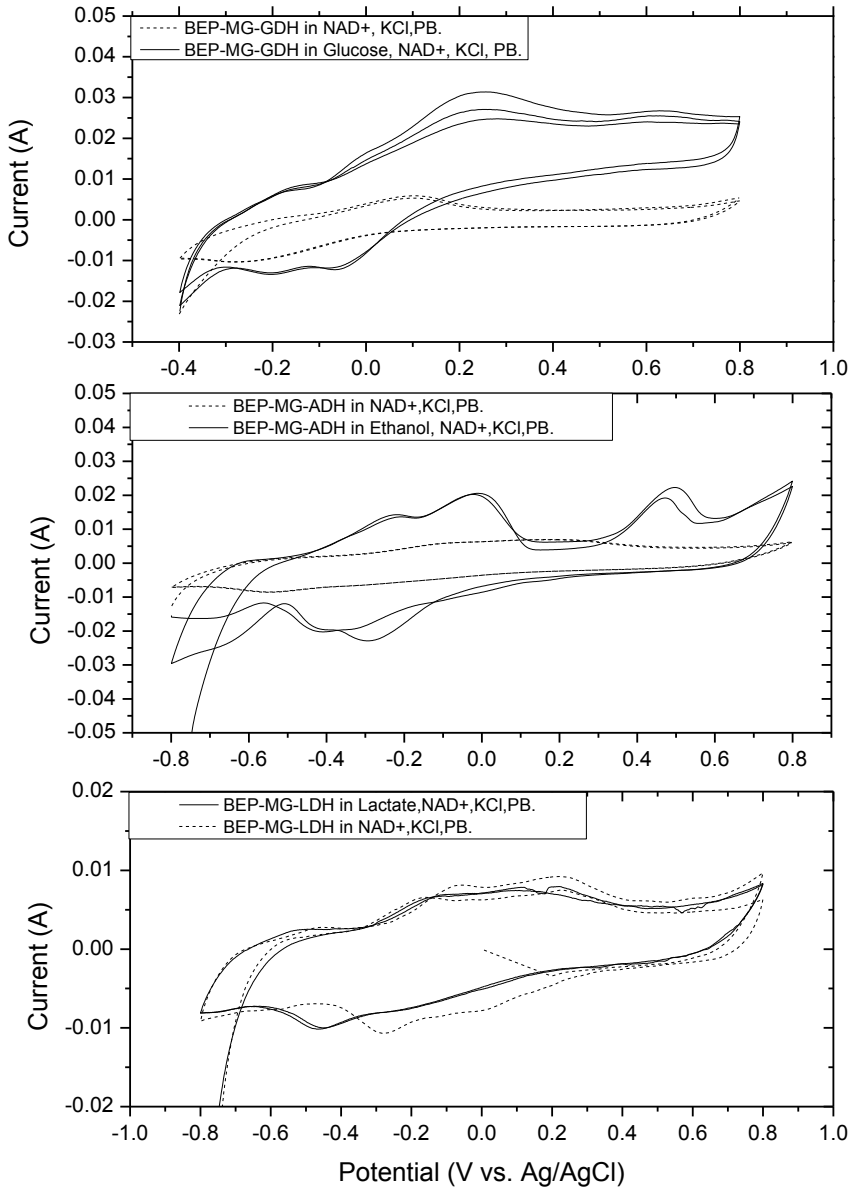

Figure 3.4. Cyclic voltammograms for BEP-MG-GDH, BEP-MG-ADH and BEP-MG-LDH anodes in electrolytic cell setup in NAD+ 1 mM, KCl 0.1M in PB 0.1M, pH 7.5 (dotted line), and biofuel (glucose, ethanol and lactate respectively) 0.1 M, NAD+ 1 mM, KCl 0.1M in PB 0.1M, pH 7.5 (full line).

To evaluate the performance of the BEP-MG-GDH anode, the polarization curves were measured from the OCP up to 0.35V in the absence and presence of the substrate. For the blank anodes (BEP, BEP-MG and BEP-GDH), the polarization curves give an output current density in the range of approximately 0 μA and 250 μA at 0.35 V in the absence and presence of the substrate. For the BEP-MG-GDH anode with 3 mg and 4 mg of enzymes on the surface of the electrode, the current density output is 2.5 $mA.cm^{-2}$ and 2.73 $mA.cm^{-2}$ (Figure 3.5.B), respectively, in the presence of glucose. The polarization curves confirm that the GDH enzyme shows higher activity by successfully oxidizing glucose within the MWNTs-wired/Chitosan matrix on the surface of the bioanode. The GDH entrapment within the wired-polymeric matrix was shown to partially stabilize the system for 30 days (Figure 3.6) where the anodes were shown to maintain ~80% of its initial performance at 15 days and ~65% of its initial activity at 30 days, when stored at 4ºC in 'dry' conditions.

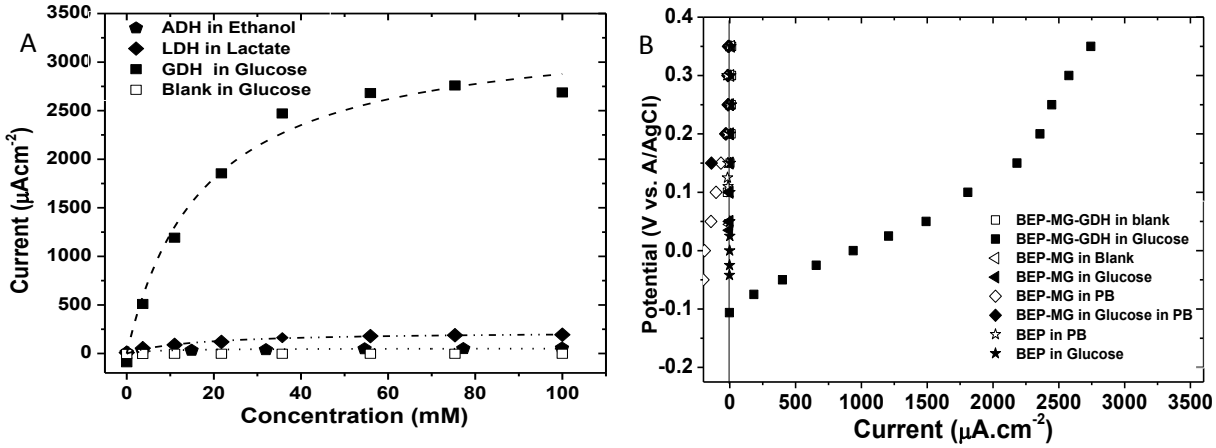

Figure 3.5. A) Michelis-Menten curves performed in the electrolytic cell setup show the activity of the dehydrogenases enzymes. GDH (-■- for 4mg,- ►-) shows the best performance in equivalent conditions with respect to LDH (-◆-) and ADH (-●-): biofuel 0.1M, NAD^+ 1mM, KCl 0.1M in PB 0.1M at pH 7.5. B) Potenstiostatic polarization curve for 4 mg (-■-)GDH- based bioanode and its respective blanks (plain BEP, BEP-MG, BEP-GDH, blank solutions 1 and 2) show the 4 mg GDH bioanode has the better performance.

The dehydrogenase enzymes herein are characterized by employing comparable enzyme units for the conversion of their respective substrate; ADH-enzyme unit is 340 Umg^{-1}, for LDH is 260 Umg^{-1} and GDH is 272 U/mg. The results obtained allow us to speculate that the chitosan-MWNTs matrix on the BEP surface (Figure 3.5) has adopted a unique 3D nano-conformation and electronic distribution that allows the GDH-structure to have a higher catalytic activity when compared to ADH and LDH. Also, it is possible that the interaction of the GDH-active site and the wired matrix on the nanostructured electrode enhance ET. The novel application of BEP into the bioanode designs introduced herein creates an efficient improvement in the interaction of the GDH active site-electrode-substrate in electrolytic solution and an improvement in the conductivity of the system's components.

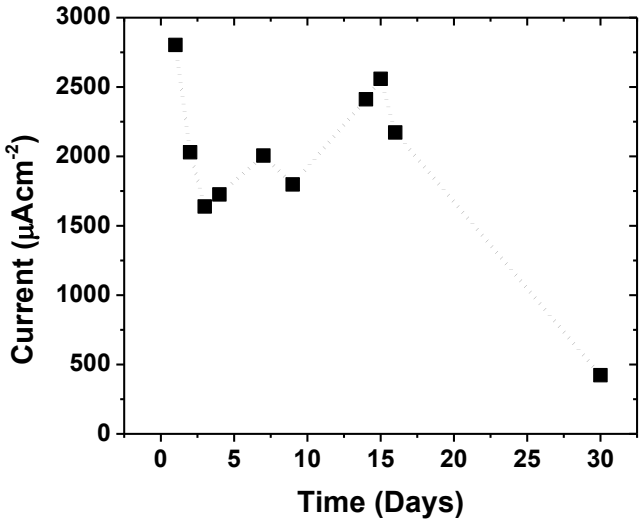

Figure 3.6. Stability study shows the GDH-based anode maintains ~80% of its initial activity at 15 days of storage at 4ºC in dry conditions.

Table 3.1. Michelis-Menten data from chronoamperometric measurements for GDH, ADH and LDH based anodes.

	I_{max} ($\mu A.cm^{-2}$)	K_M (mM)
BEP-MG-GDH	3382 ± 180	17.5 ± 3.1
BEP-MG-LDH	226.6 ± 10.1	16.0 ± 2.5
BEP-MG-ADH	53.4 ± 5.1	6.6 ± 3.3

3.4. Conclusion

This study has demonstrated an improvement in design compared to previous studies using NAD+-dependent GDH enzymes and CNTs network on the anode's surface (6.5μA at 0.1V at 45mM glucose concentration[166] and ~240 μA at 0.1 M glucose[167] both at 0.1 V). The BEP-MG-GDH anode shows a higher thermodynamic and kinetic performance than ADH and LDH- based anodes, demonstrated by the OCP measurements and Michaelis-Menten analysis. The catalytic performance of the 3D-GDH structure integrated into the composite MWNTs-nanomaterials has shown the best performance when compared to ADH and LDH, dehydrogenases that show comparable enzyme unit activity. These results show the kinetic, ohmic and mass transport limitation inherent in the GDH-based anode have been minimized allowing high current outputs. These nanostructured bioanodes can be assembled to quasi-2D capillary-driven flow systems for real fuel cell applications.

Chapter 4. NAD^+/NADH Tethering on MWNTs-Bucky Papers for NAD^+-Dependent Glucose Dehydrogenase-Based Anodes

4.1. Introduction

The development and implementation of alternative energy systems is highly desired and envisioned for overcoming environmental issues. Furthermore, designing environmentally friendly power devices is needed because current systems such as conventional batteries have shown to contain toxic compounds and produce toxic residues.[168] Harvesting energy from glucose, for example, would make possible the utilization of fruits as well as commercial drinks as source of biofuel and the products of their oxidation are naturally biodegradable. Enzymatic biofuel cells are devices engineered for that purpose.[2, 12, 169] These biofuel cells are envisioned to power small portable devices and devices for biomedical applications.[1, 2, 4, 5, 12, 15, 24, 25, 121, 170-175]

Increasing the efficiency of the biofuel cell systems requires decreasing limitations on the kinetics of the catalytic layer, resistivity losses of the electrode materials and mass transport losses. In previous work, we reported the integration of bucky papers[109] (multiwalled carbon nanotube (MWNTs)-based papers) to bioelectrode designs to reduce kinetic and ohmic limitations. The employment of a quasi-2D microfluidic system (paper-based fan) was employed to decrease mass transport limitations of fuel to the catalytic layer. The enzymatic systems were immobilized within CNTs network-Chitosan 3D-matrix in order to improve electron transfer and enzyme lifetime. Herein, the improvement of the NAD^+-dependent glucose dehydrogenase (GDH)-based bioanode is presented.

Harvesting energy from glucose by enzymatic biofuel cells could be performed by using oxidoreductase enzymes such as glucose dehydrogenase (GDH) on the anode[133] and analogous

enzymatic systems on the cathode for reduction of oxygen from air.[120, 140] At the anode, GDH shows a biocatalytic activity when coupled to its NAD^+/NADH-cofactor.[57, 71, 74, 151, 173] The oxidized form of the cofactor (NAD^+) is reduced to (NADH) while glucose is oxidized to gluconolactone. The reoxidation of NADH is needed for the GDH enzymatic activity to continue. Since NADH oxidation occurs at high overpotential, mediators such as methylene green (MG) are employed to overcome this energetic barrier.[58, 59, 84] NAD^+ is externally fed into the system with the biofuel solution. MG is polymerized on the electrode's surface. Then, engineering of a reagentless bioanode where NAD^+/NADH-cofactor is immobilized on the bioanode's surface allows for no-external feeding of the cofactor. This is highly desired for improved cofactor-enzyme-electrode interaction and improved friendly-user design of the biofuel cell.

The development of reagentless bioanodes employing NAD^+/NADH-dependent dehydrogenases has been the area of study of researchers designing anodes for biosensor applications primarily. According to literature, several approaches considered the integration of the cofactor to polymeric structures such as dextran[134], alginate[135], polyethylene glycol[136], chitosan[137], polyethyleneimine[130, 138], and entrapment in sol-gel using glycidoxypropyltrimethoxysilane[129, 131] as linker. Then, the improvement of the dehydrogenases-based anode designs involve the tethering of the NAD^+/NADH-cofactor in proximity to the enzyme to enhance electron transfer in order to create an efficient reagentless enzymatic biofuel cell.

In our research, the tether selected is pyrene butanoic acid succinimidyl ester (PBSE) which interacts with the surface of carbonaceous MWNTs without disrupting its conductivity. The use of an adsorbed crosslinking agent on the MWNTs is desired in order to maintain the benzene-

ring like structure and the quasi-metallic electronic conductivity of their walls. Chen et al reported the successful use of PBSE as noncovalent functionalization agent for protein immobilization on single walled nanotubes (SWNTs) by π-stacking.[101] The pyrenyl group of the compound was reported to interact with the graphite plane and the SWNTs surface. However, due to the planar structure of the pyrenyl ring, this moiety has better interaction with carbonic MWNTs. These have a larger diameter than SWNTs and wall circumference which is 'seen' by the pyrenyl rings as approximately planar structure which improves π- π interaction. At the opposite side of the tether chain, at the *N*-hydroxysuccinimide side of the PBSE agent, an amine group of the enzyme is attached covalently to the tether by forming an amine bond. The immobilization of enzymatic structures on MWNTs-based materials for biofuel cell applications was successful.[142] Similarly, due to the presence of an amine moiety in the molecular structure of NAD^+/NADH, the formation of a covalent amide bond with the *N*-hydroxysuccinimide side of PBSE is expected. The NAD^+/NADH-PBSE structure would be absorbed by *π-π* interaction on the surface of the MWNTs integrating the bioanode material.

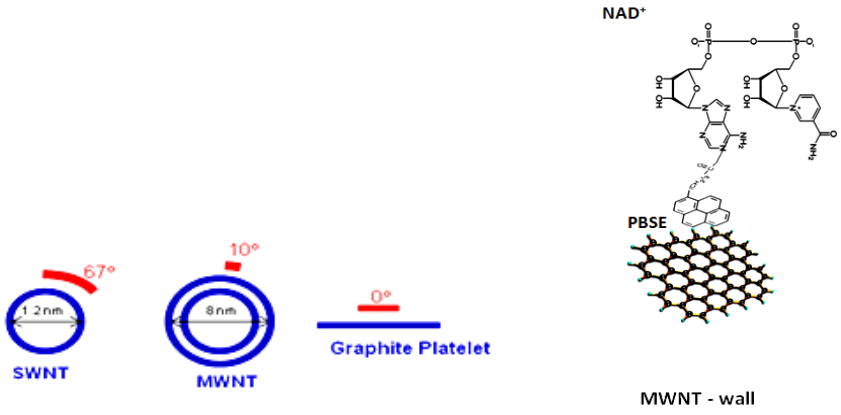

Figure 4.1. PBSE interaction with MWNTs surface *(Am. Chem. Soc. 2001, 123, 3838)* and NAD^+ linked to PBSE which interacts by pi-stacking interaction with the MWNTs surface

Herein, we present two non-reagentless and reagentless bioanode designs. The latter is characterized for having the NAD^+/NADH-tethered on the MWNTs-based bucky paper PBSE by

π-π interaction while the GDH enzyme is entrapped within a CNTs/Chitosan 3D-matrix. Additionally, we have integrated a new bucky paper, CMN-grade, which has demonstrated to increase the current output performance in the GDH-bioanode design. The objective of this research is to minimize the inherent limitations of the bioanodic system and improve the bioanode design to a reagentless GDH-based anode for biofuel cell applications.

4.2. Experimental Methods

4.2.1. Apparatus. The electrochemical experiments were performed in a three-electrode cell by conventional potentiostat: Gamry Reference 600 Pontentiostat/Galvanostat. All potentials are reported vs Ag/AgCl. The material characterization was performed using a scanning electronic microscope Hitachi (S-5200) equipped with an energy dispersive spectrometer (EDS) and Kratos Axis Ultra DLD X-ray photoelectron spectrometer.

4.2.2. Chemicals. Buckeye Paper (BEP) of thickness of 15-250 μm and purity of ~100% MWNTs and CMN grade-bucky paper of 15-250 μm and a purity of ~100% were obtained from Buckeye Composites Inc. (Kettering, OH). Isopropanol (purity >99%), monobasic and dibasic sodium phosphates were obtained from EMD Chemicals Inc. and used to prepare pH 7 and pH 7.5 phosphate buffer stock solutions. Methylene Green (MG) Zinc Chloride double salt (purity >99%, from Fluka Cat. 66870) and KNO_3 from EMD Chemicals Inc. were used to make MG growing solution in phosphate buffer of pH7. NAD^+ (purity >98%, Fluka Cat. 43407). D(+)-Glucose (purity >99.5%), Lyophilized Glucose Dehydrogenase (GDH-2) from *Pseudomonas sp.* (272 U/mg activity, Cat. 19359) from Amano Enzyme USA Co., Ltd. (Elgin, IL). Koptec 200

Proof Ethanol from VWR (King of Prussia, PA). Pyrene butanoic acid succinimidyl ester (PBSE) (Cat. 457078) from Sigma-Aldrich (St. Louis, MO).

4.2.3. Anode Design Procedure. BEP and CMN-based bioanode designs and their respective control electrodes were developed, evaluated and compared in this study. Three set of each electrode were analyzed for reproducibility and reported herein. Each electrode material was washed with IPA initially, and DI water later. The polymerization of MG proceeded as described in previous work by cyclic voltammetry.[133] For electrodes with no cofactor immobilized, the deposition of the GDH was performed after PMG formation. For electrodes employing NAD^+-tethered on the electrode surface, NAD^+ and PBSE dissolved, mixed and deposited on the bucky paper's surface after PMG formation. PBSE tether was dissolved in DMSO and the NAD^+ cofactor in phosphate buffer (PB) 0.1M at pH 7.5. The amount of PBSE and NAD^+ used maintained the 1:1 molar ratio. For a 3.7 cm^2 of geometrical surface area of bucky paper, 5 mg NAD^+ is dissolved in 100 µl PB 0.1M, pH 7.5 and 2.9 mg PBSE in 100 µl DMSO. After the electrode was dried for an hour at room temperature (25±1 ºC), the immobilization of the GDH is performed by mixing the enzyme within 150 µl of 95/5wt% Chitosan/CNTs mixture, deposited on the electrode and left to dry overnight at 4ºC. The electrodes fabricated were BEP-MG-GDH and CMN-MG-GDH (with no tethered NAD^+), and BEP-MG-NAD^+-GDH and CMN-MG-NAD^+-GDH (with tethered NAD^+). Control electrodes, CMN and CMN-MG electrodes, were evaluated in similar conditions.

4.2.4. X-Ray Photoelectron Spectroscopy. XPS measurements were performed with a Kratos Axis Ultra DLD X-ray photoelectron spectrometer using a monochromatic Al Kα source operating at 225W. The data obtained are average from 3 separate areas per sample. High resolution spectra of C1s, O1s, N1s and S2p were acquired after the survey was taken. No charge

compensation was necessary. The samples MG, GDH-Chitosan, NAD^+, PBSE, plain BEP, plain CMN, BEP-MG, CMN-MG, BEP-MG-PBSE-NAD^+, CMN-MG-PBSE-NAD^+, BEP-MG-PBSE-NAD^+-GDH (BEP full set) and CMN-MG-PBSE-NAD^+-GDH (CMN full set) were analyzed. Additionally, the analysis of samples with NAD^+ tethered by PBSE was done. After the bioanode was electrochemically tested, we have analyzed it with respect to time in continuous operating conditions. The sampling times were at 0, 1, 3, 6, 9, 12, 15, 18 and 24 hours.

Data analysis and quantification were performed using the CasaXPS software. A linear background was used for C 1s, N 1s, O 1s, S 2p and P 2p spectra. Quantification utilized sensitivity factors that were provided by the manufacturer. A 70% Gaussian / 30% Lorentzian (GL (30)) line shape was used for the curve-fits. Full width at half maximums (FWHMs) used for curve fits of N 1s and S 2p spectra were constrained to 1.1 ± 0.2 eV for all spectra acquired. These are based upon analysis of reference materials. Curve fitting analysis was completed first on the high resolution spectra of reference compounds using the above parameters and then similar constraints were applied to mixture spectra and new peaks were added (if necessary) to obtain an optimal curve fit. Identification of peaks is based on Scienta ESCA300 database[14] and NIST Standard Reference Database[15].

4.2.5. Chronoamperometry. The BEP and CMN-based electrodes were tested by chronoamperometry, the current generated was monitored while step potentials were applied. Each step was maintained for 300 seconds and incremented by 50 mV with respect to the previous; the potential range started from the OCP up to 350mV. The electrochemical test was performed in a three electrode-electrolytic cell as well as in the 270º paper-based fan cell at room temperature as well as 4ºC. The results were used to generate the potenstiostatic polarization curves (potential vs. current density). Later, similar procedure was used to monitor the electrode

behavior with respect to time, at this time every stepping potential was applied during an hour. The overall test lasted 20 hours.

4.2.6. Chronopotentiometry. The electrodes were evaluated by chronopotentiometry, the steady state current obtained by chronoamperometry (described above) was applied to the electrodes, and the resulting voltage was monitored. Each step was maintained for 500 seconds. These tests were performed also on both electrolytic and fan cell-setup at room temperature. The resulting potentials were used to generate the galvanostatic polarization (potential vs. current density).

4.2.7. Michaelis-Menten Analysis. The kinetic activity of the enzyme on the anodic surface was monitored as a function of substrate concentration and temperature by chronoamperometry. At 50 mV of constant applied potential, current generated was monitored when the aliquots of substrate were added to the electrolytic cell every 400 seconds. The results obtained were used to develop the Michaelis-Menten curve (current vs. concentration) and to find the respective parameters.

4.2.8. Stability Study. In previous research, we analyzed the stability of the catalytic layer of the BEP-MG-GDH bioanode in storage in 'dry' conditions at 4ºC for 30 days. In the current study, the electrode integrating CMN-grade bucky paper was evaluated similarly. Additionally, the stability study at continuous working conditions was performed on the reagentless bioanode design. Also, XPS analysis was performed for the test in continuous operation of the anode.

4.3. Results

4.3.1. Bioanode Design. The bioanodes developed integrated BEP and CMN- grade bucky papers, and the NAD^+/NADH-cofactor and GDH-enzyme immobilized on the bioanode surface.

SEM images show the nanoarchitecture of the plain BEP and CMN surface differ from each other in the diameter range of MWNTs-integrating the material. The surface of BEP-paper is constituted by MWNTs of more uniform size distribution, diameters ranged between ~15 nm to 40 nm (Figure 4.2.a). The CMN-nanoarchitecture shows to be constituted by MWNTs of a wider range in diameter, from ~10 nm to 200 nm (Figure 4.2.b). Due to the wide diameter/size differences of the MWNTs, the CMN-paper has a wider range of porous structures as well (Figure 4.2.c). When the cofactor and enzyme in Chitosan/CNTs mixture is deposited on the electrode surface, the mixture is capable of penetrating the small and wide porous structures and form a 3D-CNTs network of unique conformation, architecturally distinct from BEP at the nanoscale (Figure 4.2.d). The CMN-nanostructure demonstrates to enhance electron transport and current generation shown below.

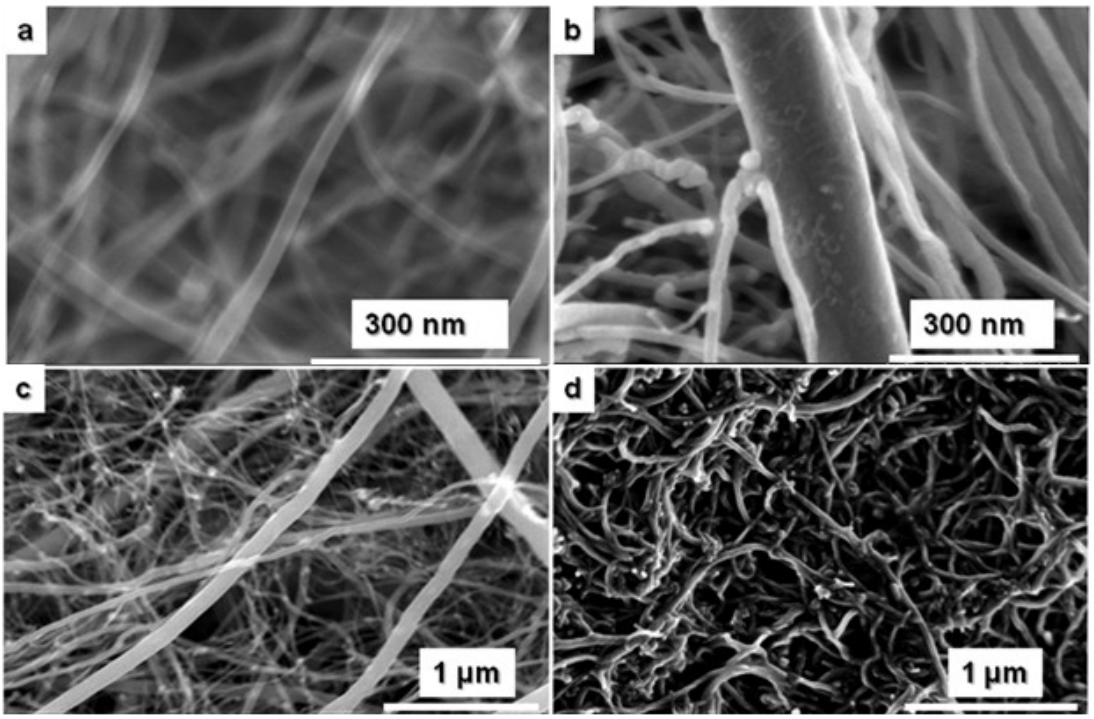

Figure 4.2. SEM images of a) plain BEP paper, b) plain CMN paper in high magnification. SEM images in low magnification of c) plain CMN paper and d) bioanode with polymerized MG and GDH deposited on the surface (CMN-MG-GDH).

4.3.2. XPS Analysis

In a recent minireview, we have discussed that through (1) careful selection of reference materials, which constitute part of the multicomponent nanoarchitectures and individual relevant mixtures, and (2) constraining curve fits using information obtained from the references, it is possible to differentiate between chemically similar biological compounds in the matrix of organic materials and to establish interaction between them.[176]

As was discussed in the Experimental section, we have analyzed all reference materials, such as CMN and BEP paper, and powders of MG, PBSE, chitosan, GDH and NAD^+. In addition, we have analyzed not only full sets but also mixtures such as BEP-MG, CMN-MG, BEP-MG-PBSE-NAD^+, CMN-MG-PBSE-NAD^+, BEP-MG-PBSE-Chitosan-GDH, CMN-MG-PBSE-Chitosan-GDH. Table 4.1 shows XPS elemental composition and Figure 4.3 shows a subset of high resolution spectra. Plain paper has only carbon and very small amount of oxygen detected. All other components of bioanode have various amounts of N, while MG has also ~3% of S and NAD^+ has ~4 % of P. The presence of N, S and P is XPS spectra confirm the expected qualitative composition of all mixtures. Based on N/C ratio for pure MG sample, MG constitutes 29% (CMN) and 23% (BEP) for MG-paper sets. N/S for both MG-paper samples is very close to that from pure MG reference. Based on N/S ratio for MG, in CMN-MG-NAD^+ 50% of N signal comes from MG and 50% from NAD^+. For BEP-MG-NAD^+ set, 40% of N signal comes from MG and 60% from NAD^+. This is also confirmed by P/N ratio for reference NAD^+. Significant increase in O and N is observed for both full sets due to the contribution from all constituents – MG, chitosan, GDH, PBSE and NAD^+. Based on amounts of sulfur and phosphorous detected we confirm that for CMN based full set, total N consists of 31% from MG, 49% from NAD^+ and

20% from the PBSE/chitosan/GDH mixture. For BEP based full set, total N consists of 18% from MG, 45% from NAD^+ and 38% from the PBSE/chitosan/GDH mixture.

Table 4.1. Elemental quantification of carbon, oxygen, nitrogen and sulfur on plain BEP, plain CMN, BEP-MG, CMN-MG, BEP-MG-PBSE-NAD^+, CMN-MG-PBSE-NAD^+, BEP-MG-PBSE-NAD^+-GDH/Chitosan/CNTs (BEP full set) and CMN-MG-PBSE-NAD^+-GDH/Chitosan/CNTs (CMN full set).

Sample Identifier	C 1s %	O 1s %	N 1s %	S 2p %	P 2p %
MG reference	73.4	11.3	12.5	2.8	
Chitosan reference	67.1	28.7	4.3		
GDH reference	64.9	22.6	12.3		
NAD reference	56.2	29.7	10.6		3.5
PBSE reference	79.3	18.8	1.9		
Sample Identifier	**C 1s %**	**O 1s %**	**N 1s %**	**S 2p %**	
CMN	99.3	0.7	0.0	0.0	
CMN MG	89.0	5.7	4.4	1.0	
CMN MG GDH Chit CNT	72.8	19.8	7.1	0.3	
CMN MG NAD	82.7	11.1	4.9	0.5	0.9
CMN full set	66.0	23.4	8.6	0.6	1.4
Sample Identifier	**C 1s %**	**O 1s %**	**N 1s %**	**S 2p %**	
BEP	99.2	0.7	0.1	0.0	
BEP MG	92.4	4.1	3.0	0.6	
BEP MG GDH Chit CNT	73.9	18.5	7.4	0.2	
BEP MG NAD	87.6	7.7	3.6	0.4	0.8
BEP full set	67.2	21.4	10.1	0.4	0.9

Figure 4.3 shows high resolution N 1s and S 2p spectra from reference pure constituents, i.e. MG, PBSE, NAD^+, and a full set on CMN paper. Pure MG has a main peak at 399.5 eV due to amine, peak at 401.3 eV due to N-C=O and peaks due to NOx species between 404 and 408 eV. Pure NAD^+ has a unique peak at 400.1 eV due to amide group in addition to peaks due to amine and N^+. GDH and Chitosan have single peak due to amine at 399.5 eV (not shown). Main peak of PBSE is due to imide at 401.3 eV. From the reference spectra, we can conclude that MG

has a unique peak at high BE between 404 and 408 eV due to NO_x, NAD^+ has a unique peak at 400.1eV due to amide, while PBSE has a large peak at 401.3 eV, but both MG and NAD+ also contribute in the same BE region due to similar N-C=O types of species or some charged N^+. This information can be used to study the composition of partial and full sets on paper. Results of N fit for all samples (not shown). All composite samples with MG have peak at 407 eV detected due to MG and its relative contribution decreases with the addition of other constituents. In a full set, this peak is 7.7 % for CMN and 5.6 % for BEP representing, based on the ratio of this peak to the total N amount, 39% of total nitrogen detected from CMN and 28% from BEP, respectively.

In samples where PBSE is present, there is an evident increase in imide peak at 401.3 eV. In partial set with NAD^+, PBSE and MG on both papers, peak due to NAD^+ at 399.7 is present. This peak, however, is absent in a full set. It may be explained by either attenuation of the NAD^+ signal with the added layer of GDH-Chitosan or change in the chemical environment of NAD^+. GDH and Chitosan have a single peak at 399.5 eV (not shown). Total amount of N increases from paper-MG sample to both MG-GDH-Chitosan and a full set (table 4.1); but the peak at 399.5, where Chitosan and GDH should contribute, the amount of N decreases significantly. This fact may be due to change in a chemical environment of amines present in Chitosan and GDH. Moreover, MG-GDH-Chitosan and a full set have large peak at 400.6 eV (Figure 4.3.d) that is not present exclusively in either of the pure constituents. This suggests a shift in BE due to the interaction between constituents. At this BE, multiple possible species may contribute, including secondary amines, protonated amines as well as N-C-O species. Change in a chemical environment of NAD^+ (amide), chitosan and GDH (primary amines) and appearance of a new peak due to secondary amines point to the interaction between constituents of a nanocomposite.

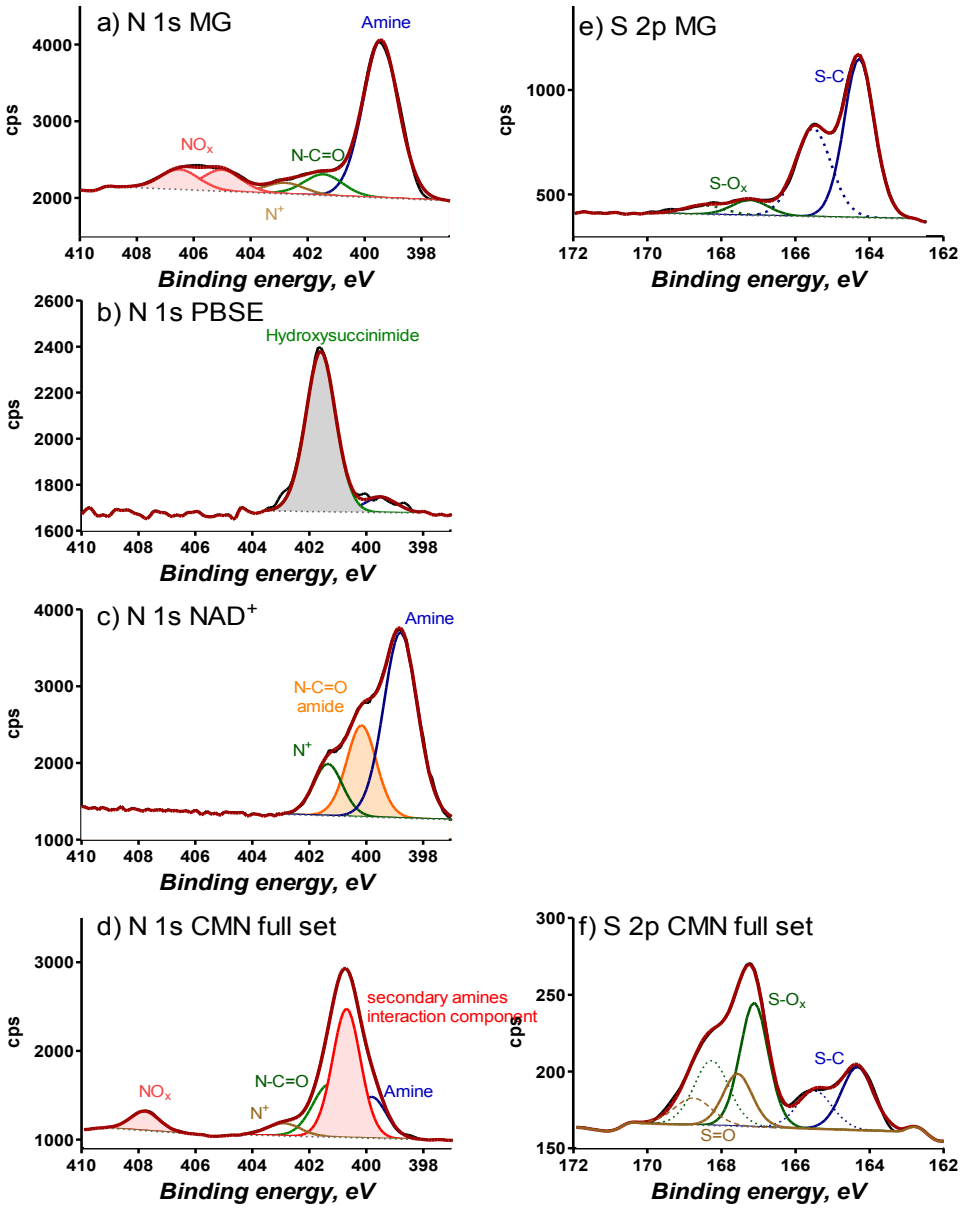

Figure 4.3. Nitrogen 1s (a-d) and sulfur 2p (2-f) spectra obtained by XPS analysis of references – MG (a and e), PBSE (b), NAD+ (d) and CMN-MG-PBSE-NAD$^+$-GDH in Chitosan/CNTs (CMN full set) (d and f).

S is only present in MG itself. In addition to the majority of S present as S-C, there is some amount present as S-O (Figure 4.3.e). When GDH/Chitosan is added to the system, the ratio of S-C to S-O changes to having more S-O (Table 1S). When MG mixed with NAD$^+$, in

addition to larger relative % of S-O, new peak at 168.2 eV due to sulfoxides $R_2S=O$ or some charged sulfonic $S=O^+$ appears (not shown). In a full set, the relative % of S-Ox is largest among all the samples, especially for CMN sample (Figure 4.3.f).

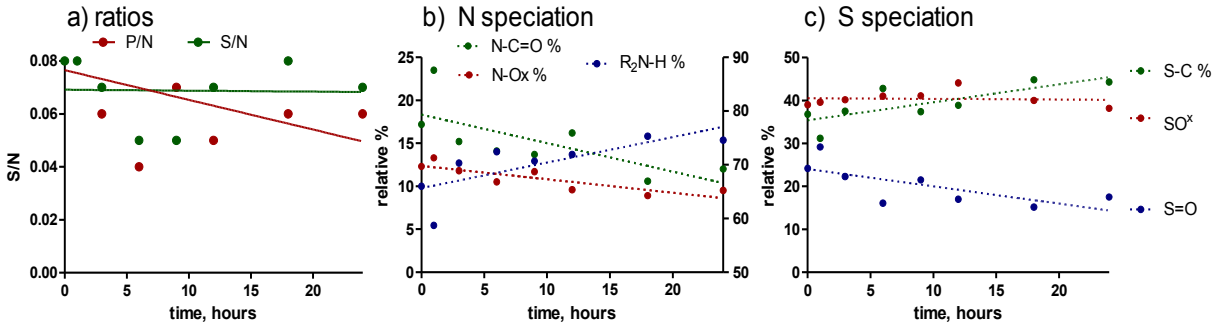

Figure 4.4. Stability of CMN full set within the first 24 hours of continuous operation. a) S/N and P/N ratio; b) N speciation and c) S speciation as a function of time

The stability of the full set nanostructures was studied by XPS. The CNM-based bioanode was electrochemically tested at 0, 1, 3, 6, 9, 12, 15, 18 and 24 hours, and these bioanodes were then analyzed by XPS. Table 2S shows full results while Figure 4.4 shows changes in the composition as a function of time for a subset of species. S/N ratio stays the same throughout the series demonstrating overall stability of MG in the matrix. There is, however, a decrease on P/N ratio with electrochemical testing pointing towards loss of NAD^+ in the nanostructure. The peak that we have identified as an interaction component between constituents of composite due to the formation of secondary amines by participating amides and primary amines, increases during electrochemical testing that is accompanied by loss of oxygenated types of nitrogen. Sulfur environment also undergoes changes in which oxygenated S species decrease while S-C increases.

4.3.3. Polarization Curves for BEP-MG-GDH/Chitosan/CNTs and CMN-MG-GDH/Chitosan/CNTs anodes.

The potentiostatic and galvanostatic polarization curves were developed by chronoamperometry and potentiometry, respectively, in order to evaluate the bioanodes performance in both electrolytic and paper-based fan shape setups. The potentiostatic polarization curves started from the OCP up to 0.35V. Control electrodes, systems without enzyme, show negligible current generation demonstrating the material has not significant catalytic properties for glucose oxidation (-□-, Figure 4.5.C and 4.5.D) as demonstrated in previous study as well[133].

For BEP-MG-GDH/Chitosan/CNTs the OCP was ~ -0.18 V[133] and for CMN-MG-GDH/Chitosan/CNTs the OCP~ -0.225V (Figure not shown). The potentiostatic polarization curves of BEP-MG-GDH/Chitosan/CNTs (-●-, Figure 4.5.A) in the electrolytic cell with the NAD^+-cofactor in solution generates ~2200 $\mu A.cm^{-2}$ at 50 mV and 2250 $\mu A.cm^{-2}$ at 0.1V (~2.5 $mA.cm^{-2}$ at 0.35V[133]). Similar procedure on the CMN-MG-GDH/Chitosan/CNTs bioanode (-■-, Figure 4.5.A) produces larger current densities, with observations of ~3100 $\mu A.cm^{-2}$ (3.1 $mA.cm^{-2}$) at 50 mV and 3600 $\mu A.cm^{-2}$ at 0.1V (~4.5 $mA.cm^{-2}$ at 0.35V). From comparison of the polarization curves, it is possible to recognize that at low current densities, the kinetic activity of the enzymatic system on the CMN-paper is slightly slower than on the BEP-paper.

At larger current densities (>2000 $\mu A.cm^{-2}$), it is possible to observe the transport limitation of the substrate to the catalytic layer on the BEP-paper is much greater than on CMN-paper. Both bioanodes were prepared to use the same procedure of MG deposition and enzyme immobilization (in Chitosan/CNTs) and both materials present comparable ohmic resistivity.

The aforementioned results allow us to infer that the porosity of the CMN-bucky paper conferred by the large range of MWNTs-size/diameter provides the CMN-structure with extraordinary nanoarchitecture demonstrating improved electron transfer and mass transfer of substrate at the catalytic layer due to an improved integration of the GDH-CNTs-Chitosan mixture within the electrode material compared to the architecture of BEP surface.

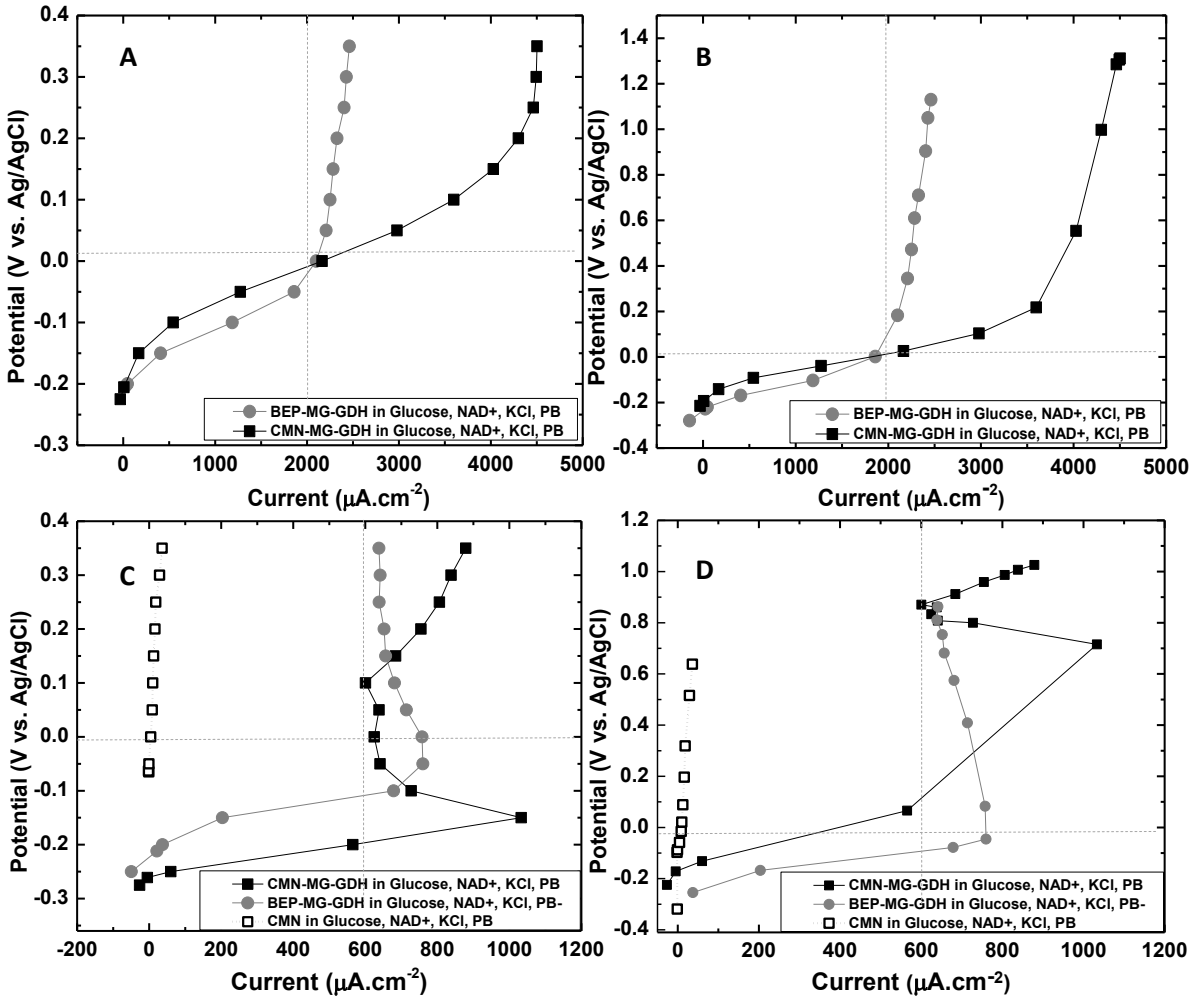

Figure 4.5. A) Potentiostatic and B) galvanostatic polarization curves performed on BEP-MG-GDH/Chitosan/CNTs and CMN-MG-GDH/Chitosan/CNTs in electrolytic cells. C) Potentiostatic and D) galvanostatic polarization curves performed in 270º paper-based fan cell. Experiments were performed in 1mM NAD^+, 0.1M glucose in 0.1M PB and 0.1M KCl at pH 7.5 at room temperature (25ºC).

Furthermore, potentiostatic and galvanostatic curves were performed to analyze the behavior of the bioanodes in simulated real-life working conditions. The galvanostatic polarization curves for both bioanodes in the electrolytic cell (Figure 4.5.B and 4.5.D) show that at applied current densities higher than 2000 $\mu A.cm^{-2}$ (>0V) the potential recorded increased drastically compared to the potentiostatic curve (comparing right upper quadrant of Figure 4.5.A and 4.5.B). At applied currents below 2000 $\mu A.cm^{-2,}$ (<0V) the behavior of the curves were similar (comparing left bottom quadrant of Figure 4.5.A and 4.5.B). At current densities below 2000 $\mu A.cm^{-2}$ and 0V, the electrochemical processes of the enzymatic catalytic layer of both bioanodes are approaching steady-state behavior, current densities and measured potentials are similar in magnitude. When potentials are increased from 0V to 0.35 V in potentiostatic mode, the polarization curve shows that the currents generated range from 2,000 $\mu A.cm^{-2}$ to 2,500 $\mu A.cm^{-2}$ and 2,000 $\mu A.cm^{-2}$ to 4,250 $\mu A.cm^{-2}$ for BEP and CMN-based anodes, respectively. On the other hand, when applying those currents to the electrodes to generate galvanostatic polarization curves, the potentials generated are observed to range from 0V to ~1.2 V and 0V to ~1.3 V for BEP and CMN-based anodes, respectively (Figure 4.5.B and 4.5.D). The potentiostatic and galvanostatic polarization curves have different behavior, the systems abandoned the steady-state at potentials > 0V and current densities > 2,000 $\mu A.cm^{-2}$. At high current densities and potentials (>2000 $\mu A.cm^{-2}$, >0V), the contribution of processes involving the material's performance may be affecting the system inducing a transient or unsteady state.

In order to minimize mass transport limitations, the bioanodes were assembled to the quasi-2D microfluidic system, and their performance was electrochemically evaluated. The OCPs were obtained and employed in choroamperometric tests. The BEP-based anode presented an OCP ~ -0.225 V and the CMN-based anode's OCP was ~ -0.275V. In order to evaluate the

catalytic layer utilizing the capillary driven microfluidic system to diffuse the biofuel, potentiostatic polarization curves were generated by chronoamperometry from the OCP up to 0.35V. Using this 270º paper-based fan setup, the polarization curve of the enzymatic system on the BEP-based anode exhibits a slower kinetic activity represented by the lower current density generated compared to the CMN-based anode, approximately 200µA.cm^{-2} for BEP (-●-) and 1100 µA.cm^{-2} on CMN (-■-), at -0.15 V (Figure 4.5.C). Both enzymatic systems exhibit shift to decreased current densities on the polarization curves at potentials higher than -50 mV for BEP and -150 mV (-0.15V) for CMN. Above 0.1V, the curve of the CMN-based bioanode starts recovering its performance by increasing the current densities generated. At 0.35 V, the CMN-based anode gives around 900µA.cm^{-2}. The BEP-based anode displays a decreasing polarization performance above -50mV and does not recover but maintains overall constant 620 µA.cm^{-2} of current density at potentials higher than 0.2V.

These results indicate the catalytic layer of the BEP-based paper presents a nanostructural architecture of smaller porosity and active site exposed to the biofuel mass transport. This observation reflects limitation of flow of the substrate to feed the catalytic layer; therefore, a decrease of current density is observed. The potentiostatic polarization curve of the CMN-based anode demonstrates decreasing electron transfer or current density due to minimized mass limitation. Although the current output decreases when the anode is assembled into the paper-fan cell when compared to the static electrolytic cell, the design is energetically convenient since no external energy is applied to drive the flow of fuel to the anode. This design could be feasible employed in biofuel cell applications that employ the glucose as biofuel.

4.3.4. Storage Stability Study on CMN-MG-GDH anode.

The stability study on the bioanodes was performed in a time range of 30 days. Potentiostatic polarization curves were developed to analyze the current output on the enzymatic systems on the electrodes at different days of storage (inset Figure 4.6.A). The experimental results, current as a function of time, were analyzed at 0.35V of applied voltage (Figure 4.6.A). The CMN-bioanode system maintains approximately 73% of its initial performance up to 25 days and ~65% up to 30 days of storage in 'dry' conditions at 4ºC. The enzymatic system is stabilized within the Chitosan/CNTs 3D-structure and is capable of generating an average of 1,800 $\mu A.cm^{-2}$ at 25 days in the electrolytic cell setup.

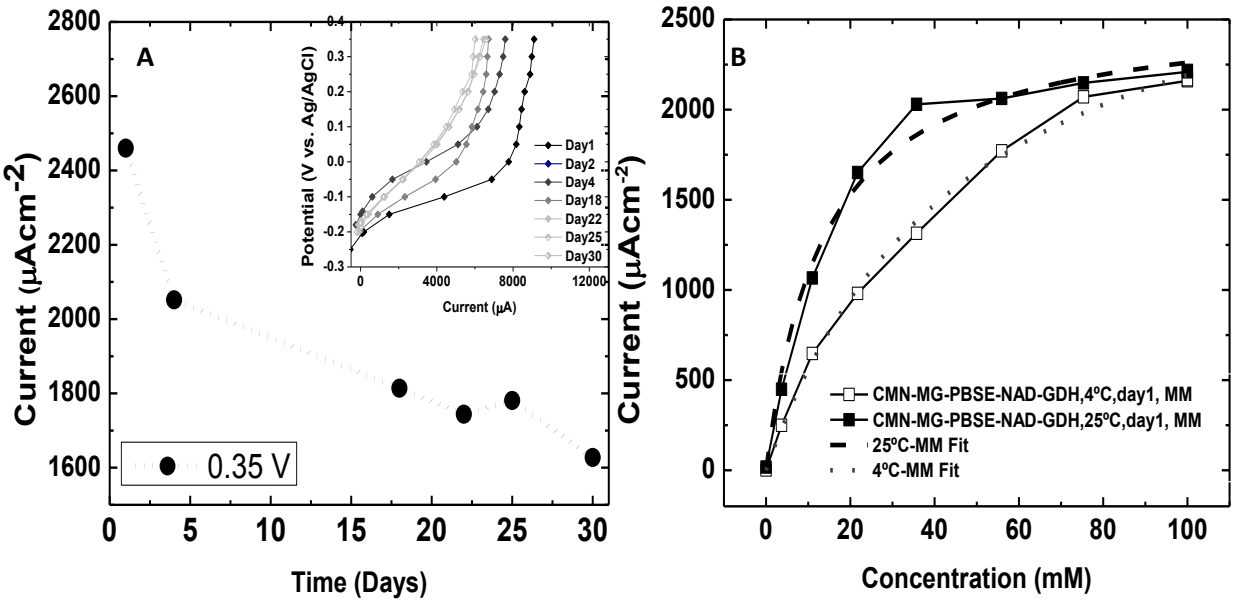

Figure 4.6. A) Stability study for CMN-MG-GDH/Chitosan/CNTs bioanode showing the current density as a function of time at 0.35V obtained from the potentiostatic polarization curves at 0.35V (inset). B) Michaelis-Menten curves for CMN-MG-PBSE-NAD^+-GDH//Chitosan/CNTs bioanode at 4ºC and 25ºC where the current generated is analyzed as a function of glucose concentration.

4.3.5. Michaelis-Menten Analysis on GDH/Tethered NAD^+-CMN catalytic Surfaces.

In order to improve the design of the bioanode to a reagentless NAD^+/NADH-dependent GDH anode, the immobilization of the cofactor was performed. PBSE tethering NAD^+/NADH-cofactor has a pyrenyl moiety that acts as footprint interacting with the MWCNTs surface by cloud overlap of sp^2 orbitals. The Michaelis-Menten parameters of the enzymatic system having the cofactor tethered to the electrode surface were found from the curve of current generated as a function of substrate concentration at 0.35V by chronoamperometry. The Michaelis-Menten curve shows that at 4ºC and 0.1M glucose a limiting current of approximately I_{Max}= 3,252.5 ±133.9 µA.cm^{-2} is observed (-□-, Figure 4.6.B and Table 4.2). At 25ºC, the limiting current is I_{Max}=2,568.1±85.0 µA.cm^{-2} (-■-, Figure 4.6.B and Table 2). The Michaelis-Menten constant at 4º C is K_M=48.3 ±4.6 mM and K_M=13.6±1.8 mM at 25ºC (Table 4.2). The resulting information corroborated the catalytic activity of the GDH coupled to the tethered NAD^+-cofactor for glucose oxidation on the bioanode surface. The kinetic of the reaction is faster at 25 ºC showing the smaller Michaelis-Menten constant, indicating I_{Max} is reached faster at 25ºC than at 4ºC. However, the limiting current is higher for the process at 4ºC which is reflected by the $I_{Max\ (4ºC)} > I_{Max\ (25ºC)}$. This may be explained from a kinetic point of view, slower movement of the cofactor-PBSE structure that allows an increased number of interactions by affinity between the substrate-active site-cofactor-electrode at 4ºC when compared to 25ºC.

Table 4.2. CMN-MG-PBSE-NAD^+-GDH/Chitosan/CNTs at 4ºC and 25ºC, Michaelis-Menten parameters obtained by chronoamperometry at 50mV.

CMN-MG-PBSE-NAD^+-GDH	I_{Max} (µA.cm^{-2})	K_M (mM)
25º C	2568.15 ± 85.05	13.6 ± 1.8

4.3.6. Stability Study at Continuous Working Conditions for GDH and Tethered NAD^+-CMN anodes.

Potentiostatic polarization curves to evaluate the bioanode at 4ºC (not shown) and 25ºC were performed in the electrolytic cell. Additionally, the stability of the electrode at continuous working conditions were developed in order to analyze the stability of the cofactor tethered on the MWNTs by π-π stacking interaction. In figure 4.6.A, the OCP at 25ºC was plotted for the system in the absence of substrate giving an OPC of 0V (light grey line); on the other hand, in the presence of the glucose substrate at day 1, an OCP of -0.25V (black line) was observed, and day 2 gave and OCP of -0.124V (grey line). The polarization curves were also obtained from OCP up to 0.35V (Figure 4.7.B).

In day 1, the applied stepping potentials of 300 seconds intervals were plotted (-●-, Figure 4.7.B). The current generated reached 2,100 $\mu A.cm^{-2}$ at 0.35V and 1,215 $\mu A.cm^{-2}$ at 50mV. After the electrode was depolarized (and OCP was measured), the electrode new chronoamperometric procedures were performed. At this time, the stepping potentials were applied for 1 hour intervals (-■-, Figure 4.7.B). At 0.15V, the current generated is ~1,250 $\mu A.cm^{-2}$ after 9 hours of hourly potentiostatic measurements but after 16 hours of continuous experimental operation. At this point, the current density had decreased from 1,750 $\mu A.cm^{-2}$ (-●-) to 1,250 $\mu A.cm^{-2}$ (-■-) at 0.15V (~71.4% initial activity was maintained). After the 0.15V, for the hourly potentiostatic polarization test, the current density generated decreased more and approached 860 $\mu A.cm^{-2}$ at 0.35V at 20 hours of continuous test (~40% of initial activity was preserved). The polarization curve obtained at day 2 shows the electrode is generating ~100's of $\mu A.cm^{-2}$ (-◇-). Later in day 2, after renewing the electrolytic solution (1mM NAD^+, 0.1M glucose

in 0.1M PB and 0.1M KCl at pH 7.5), the electrode began generating current densities close to the ones obtained in day 1 (plot not shown). These results indicate that continuous interaction of the tethered NAD^+ with GDH-enzyme and PMG (to produce NADH and regenerate NAD^+, respectively) induces the release of the tethered cofactor to the solution. This phenomenon is also corroborated by ultra-violet light spectroscopy (not shown) and XPS analysis (not shown). The structure of the enzyme however is preserved on the electrode surface, and it maintains its catalytic activity.

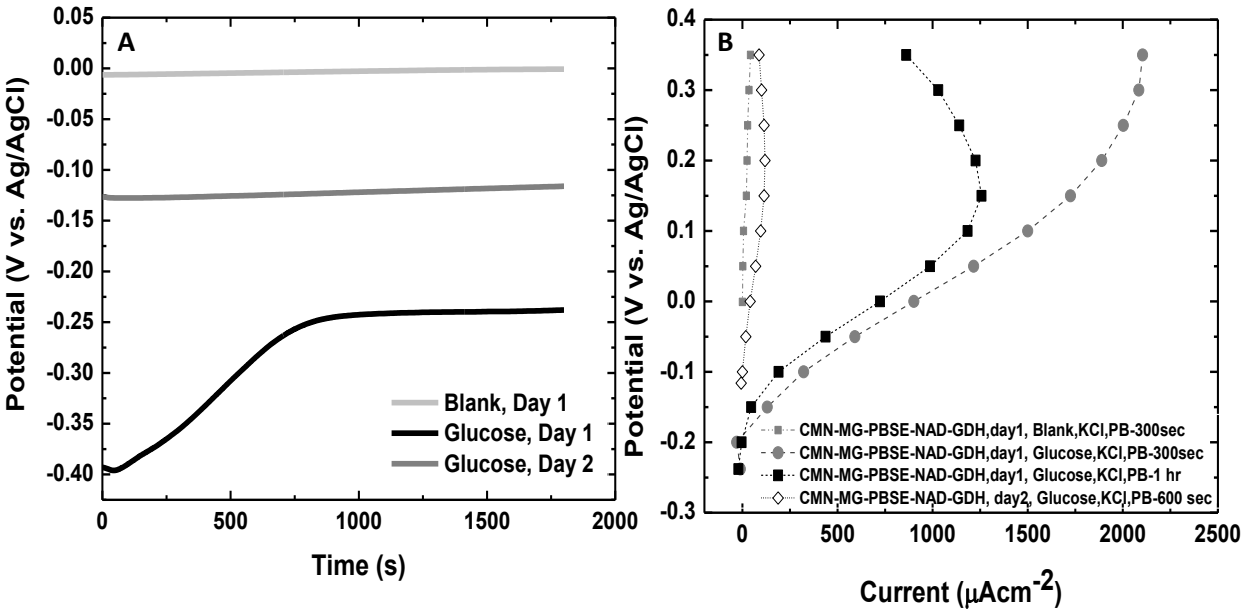

Figure 4.7. A) Open circuit potential of CMN-MG-PBSE-NAD^+-GDH/Chitosan/CNTs in absence (light grey line) and presence of substrate (grey line) at day 1 and in the presence of substrate at day 2 in an electrolytic cell. B) Potentiostatic polarization curves performed on CMN-MG-PBSE-NAD^+-GDH/Chitosan/CNTs in an electrolytic cell in the absence (-■-) and presence of substrate (0.1M glucose, 0.1 KCl in 0.1M PB) at day 1: measurements taken at 300 seconds intervals (-●-) and at 1 hour interval after OCP, potentiostatic polarization by chronoamperometry and depolarization (-■-, starting after 7 hours of working conditions); at day 2: intervals of 600 seconds (-◇-).

The nanoarchitecture of the entrapment matrix has adopted exceptional characteristics that increased enzyme loading and fuel mass transfer. The chitosan/CNTs 3D-structure on the CMN-bucky paper forms a CNTs- 3D network that helps to maintain the active 3D-enzymatic conformation and enhances electron transfer as observed on the previous study on BEP-based GDH-bioanodes.[133] The increased current density demonstrated by the CMN-based anode compared to BEP-bioanodes may be due to the increase in the porosity range that allows the GDH/Chitosan/CNTs mixture to reach inner depths on the CMN-material. The large range of pore size allows further minimization of substrate mass transport limitations.

4.4. Conclusion

This study proposes various advances in GDH and bucky paper- anode designs looking to minimize kinetic, ohmic and mass transport limitations for feasible application into fuel cell designs. The improvement in current density generation has been possible by increasing the surface to volume ratio and porosity of the electrode material that increases enzyme loading and fuel mass transport to the catalytic layer. The stability of the enzymatic system has been preserved in a Chitosan/CNTs-matrix that posses a unique CNTs-3D network that induces improvement in substrate-enzymatic active site-electrode surface interaction enhancing electron transfer and current output.

The first improvement in design was presented in the BEP-MG-GDH anode which showed OCP of -0.18V, and current generation of approximately 2.2 $mA.cm^{-2}$ at 50 mV and 2.5 $mA.cm^{-2}$ at 0.35V[133]. The later improvement consisted in modifying the aforementioned nanostructural architecture of the enzymatic catalytic layer introducing a new material, the CMN-bucky paper. The current generated by the CMN-MG-GDH bioanode has extraordinary

performance approaching -0.225V of OCP, and a current generated of ~3.1 $mA.cm^{-2}$ at 50 mV and ~4.5 $mA.cm^{-2}$ at 0.35 V in the electrolytic cell.

Next, the use of a paper-based quasi-2D microfluidic system improved the biofuel feeding process with non-external energy supplied because it consisted of a capillary driven flow maintained by liquid-vapor equilibrium. The integration of such system to the half-cell, anode, was successfully achieved. This assembly presents an OCP of -0.225V and -0.275 for BEP and CMN-based anodes, respectively and displays 200$\mu A.cm^{-2}$ and 1.1 $mA.cm^{-2}$ at -0.15V for BEP- and CMN, respectively. This bioanode satisfactorily exceeds the performance of recent MWNTs-based designs.[167]

The bioanode was redesigned to a reagentless NAD^+-dependent GDH anode. The NAD^+-cofactor was tethered to the surface of the MWNTs-wall by employing a linker capable of adsorbing on the CNT-wall by π-π stacking interaction from the pyrenyl end of the molecule. At the alkyl-ester end, the molecule forms a covalent amide bond with the amine moiety of the NAD^+ molecule. These bonds made feasible the immobilization of the mentioned cofactor which can be successfully coupled to the glucose oxidation by the enzymatic process and can be regenerated by action of the MG mediator. This design has a working duration time of approximately 16 hours which shows an improvement with respect to previous research.[131]

The reagentless and non-reagentless NAD^+- dependent GDH-based bioanode integrating CMN-bucky paper presented in this research has demonstrated to be reproducible and feasible to employ in half-electrolytic and paper-based fan cells. These designs could be employed in the real fuel cell applications to power small devices as well. Further studies have to be performed to prolong the continuous working conditions of the reagentless bioanode and storage life as well in

order to meet manufacturability standards and user needs. However, to the author's knowledge, the bioanodes introduced in this research have shown the best performance among previous NAD^+-dependent GDH-based bioanodes or other enzymatic system used for glucose oxidation.

Chapter 5. Design of Gas-Diffusion Cathodes Integrating Carbon Nanotube Modified-Toray Paper and Bilirubin Oxidase

5.1. Introduction

Interest in biofuel cells has increased in the past decade in the pursuit of self energetically-sustained biomedical devices and also small, portable electrical devices capable of working by harvesting energy from natural fuels. Such interests exists due to the low temperature and neutral pH operating range of biofuel cells[2, 4, 14], this depends on the mechanism of the enzyme, either direct or mediated electron transfer (DET and MET, respectively). Further design considerations center on three main areas of inherent energetic losses in fuel cells: kinetic, ohmic and mass transfer limits. Although there are different ways to design an enzymatic electrode, the general procedure requires deposition of the enzyme onto a conductive material which then should be immobilized in a matrix such as chitosan[177], nafion[178], or silica gel in order to retain enzyme structure and function[48, 91, 179]. The objective of this research was to stabilize the enzymatic structure within a 3D-silica matrix to create an air "breathing" biocathode. The bioelectrode surface was designed to: a) improve enzyme loading on the biocathode while improving the kinetic activity of the system, b) decrease mass-transfer limitations of oxygen, protons and electrolytes while retaining the active enzymatic 3D structure stabilized on the surface of the bioelectrode, and c) minimize the resistivity of the electrodes by incorporating a highly conductive carbon nanostructure on the electrode.

Previous research established that the design of a viable enzymatic gas-diffusional cathode has to satisfy the following requirements:

1) Have a porous hydrophobic layer that allows the flow of oxygen to feed the catalytic layer.

2) Have a porous thin catalytic layer with enzyme-air-electrolyte three-phase interface[120, 180].

3) Preserve enzymatic activity.

At the three phase interface, oxygen molecules from air and proton (H^+) from the electrolytic solution meet at the active site of the enzyme (Figure 5.1). The oxygen molecule is reduced at the active site of the enzyme by the electrons obtained from the electrode. The end product is water that should be repelled or pushed past the three-phase interface (electrode surface) in order for the reaction to continue. Therefore, in order to enhance electron transfer at the electrode surface, an enzymatic structure showing DET immobilized within a porous matrix on the electrode surface is desired.

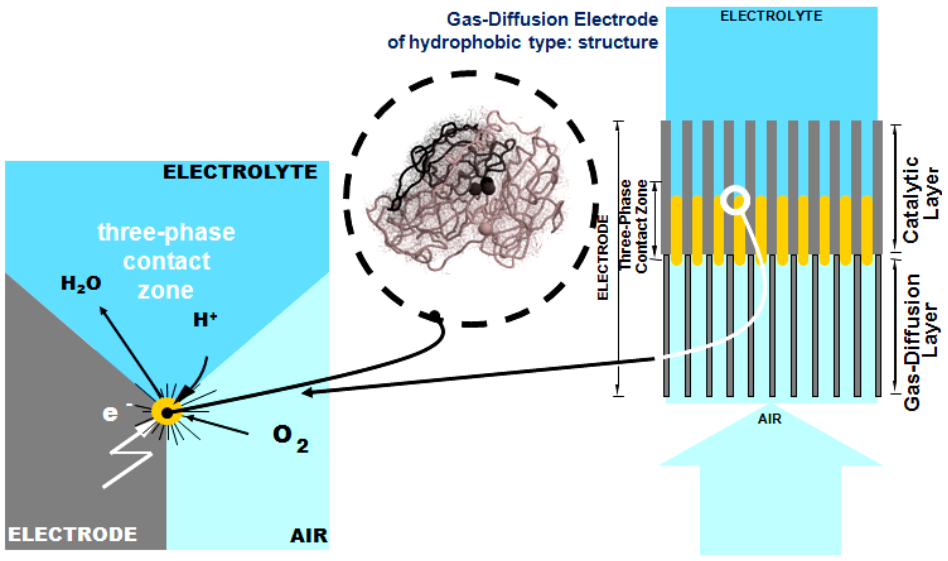

Figure 5.1. Schematic of a gas-diffusion cathode, three phase interface conceptual design for oxygen reduction at the catalytic layer *(Image source: Building Air-Breathing Biofuel Cell Cathode, Fuel Cell Design Paradigm in the Context of Enzyme Catalysts, Prof. Plamen Atanassov, University of New Mexico).*

The biocathode design presented here is constructed by utilizing a dual-layered electrode assembly that integrates composite nanomaterial constituting a unique nanoarchitecture. Toray

paper (TP) modified with carbon nanotubes (CNTs) were introduced by previous studies[46, 105, 181] as alternative materials to minimize ohmic losses and increase gas diffusion transfer. In this research, the gas diffusion layer (GDL) has hydrophobic and porous properties to allow oxygen transport (XC35, 35% teflonized carbon powder) while the catalytic layer (CL) is thin and has a high surface area for enzyme loading and stability. A chemical vapor deposition (CVD) process was used to grow CNTs onto the TP surface utilizing electrodeposited metal seeds which catalyze the reduction of the carbon source[46, 105, 112, 113, 182-184], ethylene, at high temperature. The integration of the hydrophobic (XC35) and hydrophilic (TP-CNTs) layers allow efficient transport of oxygen. In order to maximize the proton mass transfer and increase the cathode's performance, the biocathode was assembled to a capillary-driven quasi-2D microfluidic system. This system facilitates the electrolytic solution transport to the cathode[119-121] by pumping the electrolytic solution by action of liquid-vapor equilibrium with no external energy applied, thus, addressing ohmic resistance in electrolyte solution by supplying "fresh" electrolyte to the CL.

As stated earlier, carbon nanostructures have a great potential for high enzyme loading, stabilization and activation of enzymes with high performances that are believed to go far from traditional electrode-enzyme immobilization techniques. Engineering the biocatalyst-electrode surface is the critical step in biofuel cell design. Because of this, the enzyme entrapment in silica-gel, a technique mostly applied in pharmaceutical research for enzyme stabilization in drug-delivery studies, was utilized. Silica-gel matrix formation by CVD has been used as encapsulation and stabilization technique for proteins (Figure 5.2).[179] Moreover, Lopez's group has been able to immobilize cell organelles such as liposones and porteoliposomes, cell membranes and whole cells and this technique has proven to conserve the organelles' stability. The polymer precursor utilized is tetramethyl orthosilicate (TMOS), a volatile silica precursor at

room temperature. The process is based on the volatilization of the precursor into a solution, which contains the enzyme. CVD of TMOS is performed within a chamber with established dimensions (50mm of diameter x 12 mm deep) to allow for adequate mass transport. Once the precursor reaches the solution/ air interface, it reacts with water by a polymerization process. As a result, the enzyme is entrapped into a bulk silica-gel or silica matrix.

$$Si(OCH_3)_4 + 4\ H_2O \longrightarrow Si(OH)_4 + 4\ CH_3OH$$

$$Si(OH)_4 \longrightarrow SiO_2 + 2\ H_2O$$

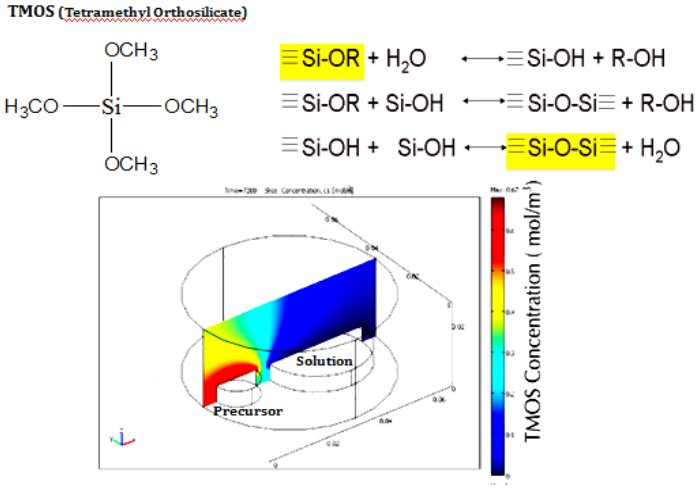

Figure 5.2. Hydrolysis and condensation of TMOS-silica precursor in aqueous solution *(Source: G. Gupta et al Langmuir 2009, 25, 13322).*

The present study aimed to engineer the enzyme/electrode surface for a biofuel design utilizing the CVD of TMOS to create catalytic layers with controlled thickness. This was performed to ensure enzyme-electrolyte solution interaction, an improvement of the DET on the electrode surface, with enzyme entrapment and stabilization was achieved.

Bilirubin oxidase (BOx) enzyme, a multicopper oxidase, was selected as the biological catalyst because it is proven to work by DET with 4 electron transfered.[1, 141] The selection of DET mechanism was done to minimize kinetic losses of the catalytic system. Immobilization of

BOx in a silica-gel matrix using TMOS resulted in the formation of a 3D nanostructure that is efficient for electron transport, increasing the current density generated.[48, 179] The TMOS entrapment was believed to prolong the enzymes stability for approximately one month.[48] In this research, the silica gel surrounding the TP-CNTs surface formed a 3D CNTs network-gel matrix which is highly conductive, porous, and stable allowing the BOx enzyme to be immobilized on the electrode's surface. The design introduced herein shows improved stability of the active 3D structure of BOx for a time range of 6 months, which was demonstrated.

The research conducted aims to tailor the nanostructured architecture of the catalytic layer for the improvement of enzyme loading and passive air breathing cathode for biofuel cell applications to power small electronic devices. The proposed design proved to be a more efficient cathode, with better controlled and more uniform size distribution of CNTs, achieved via pulse chronoamperometry employed in this research**.**

5.2. Experimental Methods

5.2.1. Apparatus

All experiments were conducted using a three-electrode cell by the common potentiostats: Gamry Reference 600 and 300 Potenstiostat, Galvanostat/ZRA and Princeton Applied Research VersaSTAT 3 potentiostat/galvanostat. All potentials were reported versus Ag/AgCl (CH Instruments Inc. Cat. CHI111) reference electrode, and Platinum mesh counter (Pt. 0.127mm and purity 99.9% Alfa-Aesar Cat. 10282). Characterization of materials was done using Scanning Electronic Hitachi Microscope (S-5200) equipped with Electron Diffraction Spectrometer (EDS). The tube furnace used was a Blue M model TF55030A from SPX-Thermal Product Solutions for the CVD of carbon nanotubes onto TP (within a quartz crystal tube).

Plasma Cleaner/Sterilizer by Harrick model PDC-32G was used to make TP pieces more hydrophilic for electro deposition process.

5.2.2. Materials

The manufacturer, Fuel Cell Earth LLC (Stoneham, MA.), of TGP-H-060 (Toray Paper) reported the material has a resistivity of 80 mΩ through the plane and 5.8mΩ in the plane. The porosity was reported to be 78% with a thickness of 0.19mm, and carbon fiber diameter of 5-10 μm. Bilirubin Oxidase (BOx) with enzyme unit 2.7 unit/mg was obtained from Amano Enzyme USA Co., Ltd. (Elgin, IL). Paper based setup consisted of Filter Paper from VWR International (North American Cat. No.: 28310-128) with 15cm diameter. The circuitry of the cell was painted on the filter paper with PELCO © Colloidal Graphite water-based, isopropanol-based, and Fast Drying Silver Paint (silver in iso-butyl methyl ketone) from TED PELLA, INC. (Redding, CA). Scotch (3M St. Paul, MN) packaging tape (clear) was used as laminate to hold the electrode in place along with generic painted paper clips.

Ethylene, Hydrogen and Nitrogen gas was supplied by Argyle Welding Supply Inc. (Albuquerque, NM). Solutions of buffer, Nickel, Cobalt made with Nickel (II) acetate tetrahydrate ($Ni(CH_3COO)_2$), 99.998% metals basis, Cobalt (II) acetate tetrahydrate, reagent grade and Tetramethyl Orthosilicate (TMOS) were obtained from Sigma-Aldrich Co. (St. Louis, MO). Potassium phosphate (KP), monobasic and dibasic from EMD Chemicals Inc., with no further purification, were used to make KP buffer solutions (K-PB) of pH 5,5.5, 6, 6.5, 7, 7.5, and 8. Deionized water from Honeywell Burdick & Jackson (Muskegon, MI) was used to make all the electrolytic solutions.

5.2.3. Metal catalyst deposition

Toray paper is a commercially available carbon-fiber paper used regularly in biofuel cells. In order to deposit metal seeds on TP, we used an oxygen plasma cleaning process to adsorb oxygen radicals on the paper's surface, making it hydrophilic. The TP-sample was placed within a plasma cleaner which is vacuum pumped to ~70 mTorr and activated for 12 seconds. Once this is done, TP was placed in a ring-like stack cell with open faces and immersed into a beaker containing the mixture $Ni(CH_3COO)_2$ and $Co(CH3COO)_2$ (solution a) or only $Ni(CH3COO)_2$ solution (Figure 5.3). The solution was prepared by weighing out 2.5 grams of $Ni(CH_3COO)_2$ and/or $CoNi(CH3COO)_2$ and dissolving it in 100mL of deionized water. The addition of 3.5mL of acetic acid (20 N Molar) brought the solutions pH to 4. With the TP in place as the working electrode and Ni-mesh as the counter electrode connected to a potentiostat, pulse chronoamperometry was performed. In order to control seed diameter and size, a potential of -1.3V was applied by chronoamperometry in 8 steps of 2 seconds each (Figure 5.3).

$$Ni(H_2O)_6^{2+}{}_{(aq)} + 2\ e^- \longrightarrow Ni_{(s)} + 6\ H_2O$$

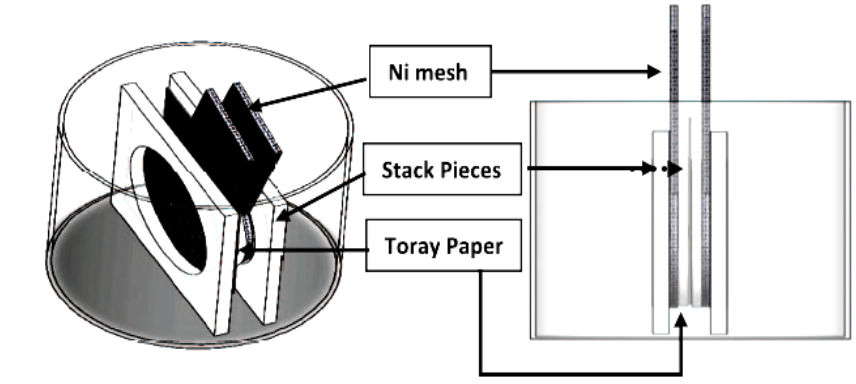

Figure 5.3. Stack cell assembly for Ni-seed electrodeposition, isometric and side views.

5.2.4. Carbon Nanotube Growth by Chemical Vapor Deposition

Chemical vapor deposition (CVD) was performed on the TP-Ni and TPCoNi in order to grow CNTs. A crystal quarts tube was utilized as the chamber for deposition. Six pieces of TP-Ni were inserted into the glass tube. The pieces were separated by reticular vitreous carbon (RVC) of 80 grade porosity to provide spacing between TP-samples and allow the flow of gases. One RVC-"sacrificial" piece was used at the front (inlet) of the tube to avoid burning of the TP-sample due to the initial temperature rise. The tube was placed in a tube furnace where an inlet and outlet hose were connected. The apparatus was equipped with gas flow controls and a sequenced-program was set to run on the furnace:

1. Gas flow settings were set at 5 $mLmin^{-1}$ for hydrogen and 95 $mLmin^{-1}$ for nitrogen. Temperature was raised 10°$Cmin^{-1}$ up to 500ºC, and was held at 500°C for 30 minutes.
2. Then, the temperature was set to increase at a rate of 10ºCmin^{-1} up to 750ºC. When the temperature reached 620ºC, hydrogen gas was shut off and ethylene gas was fed at a rate of 35 $mLmin^{-1}$ while the flow of nitrogen gas was maintained.
3. The temperature was maintained at 750°C for one hour, ethylene and nitrogen flow were maintained per step 2 above. After 60 minutes at 750°C exposure, the ethylene flow was shut off and the tube was left to cool down.
4. The contents were removed once at room temperature.

The results from Ni-seed deposition and CNTs growth observed under SEM are shown as Figure 5.4.

5.2.5. Dual-Layer Assembly and BOx-Enzyme Entrapment

As stated previously, the design of an air-breathing cathode must have a porous hydrophobic layer, this was achieved by employing 35% teflonized carbon powder (XC35) on

TP. 75mg of XC35 was pressed on the surface of TP at 1000 psi for 5 minutes along with 50uL of ethanol, using a hydraulic table press. The powder was weighed and placed in a die with 1.446 cm of diameter and circular area of 2.27 cm^2, which was the area of CNT growth. This hydrophobic layer allowed for constant oxygen diffusion from the air toward the catalytic layer. This process was performed to create the XC-TP-CNTs electrode (where XC stands for XC35).

The enzyme was entrapped on the CNT-modified TP through the polymeric matrix formation of silica gel. First, 5mg of BOx enzyme was dissolved in 200µL of 0.1M K-PB, pH7.5 and deposited on the CNT modified-TP surface (the CL). BOx was allowed to physically adsorb overnight at 4°C. The following day, the biocathode with BOx was placed in a CVD chamber (9cm diameter, 1.7cm height) of approximately 108 cm^3 in volume. Two small caps were placed in the chamber, one with 1 mL of deionized water and the other 200µL of TMOS, for a period of 5 minutes while having the catalytic layer of the CNT-modified TP exposed to the TMOS vapor. Later the chamber was sealed with parafilm and TMOS vapor diffused toward the exposed surface of the electrode along with water vapor reacting to form a silica-gel matrix. Five minutes of deposition formed an adequate thickness to entrap the enzyme and allow gas and electrolytic solution diffusion to the enzyme. After the TMOS deposition, the cathodes, which contain the BOx dissolved in K-PB, were stored in a refrigerator overnight at 4°C, as TMOS was still reacting on the surface of the electrodes to form silica gel.

5.2.6. Stability of BOx by Electrochemical Characterization

A pH and a time-stability study were conducted to evaluate the activity of the enzyme when submitted to low acid and low basic environments as well as the stability of the active site of the enzymatic structure within the 3D silica- gel matrix when stored for prolonged periods of

time. For the pH stability study, the thermodynamic potential and performance of the enzyme were evaluated when the biocathode was exposed to electrolytic solutions of pH: 5.5, 6, 6.5, 7, 7.5, and 8.

Later, for the time stability study, a batch of biocathodes were fabricated and stored at 4ºC, and later evaluated at different time intervals using an electrolyte at pH 7.5 (physiological pH). The biocathodes were selected randomly for testing at different intervals for a period of 6 months. The performance of the enzymatic systems was also analyzed by OCP and chronoamperometry.

5.2.7. Paper-Based Cathode Microfluidic System Ensemble

The biocathodes were assembled onto a capillary driven-quasi 2D microfluidic system. This system was fabricated from filter paper that also served as a structural mechanical support, proton exchange membrane and separator. The system consisted of a filter paper cut out with a 270º- semicircular shape (fan) adjacent to a rectangular section (leg) as depicted in Figure 1.14 (chapter 1). The biocathode and Pt-counter electrode were placed on opposite sides of the paper and laminated on the fan's leg using packaging tape. The lamination was designed to allow the exposure of the hydrophobic layer (XC35) of the cathode to air. After the half-cell assembly, the section of the fan's leg that was not laminated was immersed in the electrolyte in a 50ml-cell. K-PB was driven through the catalytic layer, which contained the BOx enzyme entrapped within the CNTs network-3D silica matrix on the CNTs-modified TP. The flow of the electrolytic solution was driven by capillary action, characteristic of the filter paper material, and maintained by the pumping effect sustained by the liquid-vapor equilibrium of the semicircular-fan shape.

5.3. Results

5.3.1. Metal seed deposition

In order to increase the surface area of the TP, CNTs were grown on the surface of the carbon fibers of TP. This was achieved by depositing Ni and Ni-Co seeds onto the TP-fibers, which catalyzed the reduction of ethylene gas forming CNTs. A range of solutions with varying pH and metal compositions including Ni, Ni-Co, and Fe were attempted (not shown) to form metal seeds. The metal solutions of Ni pH4 (Figure 5.4.A) and Ni-Co pH7 (Figure 5.4.B) were used to produce metal's nucleation. Ni seeds deposited at pH4 nucleated into seeds having a defined shape and regular size (35–60 nm diameter, Figure 5.4.A). Ni-Co seeds deposited at pH 7 nucleated into seeds having an agglomerated shape and larger size (70–120 nm diameter, Figure 5.4.B). This result led to the use of Ni pH4 seeds exclusively for CNT growth for the cathode, with the goal of obtaining CNTs with a uniform distribution.

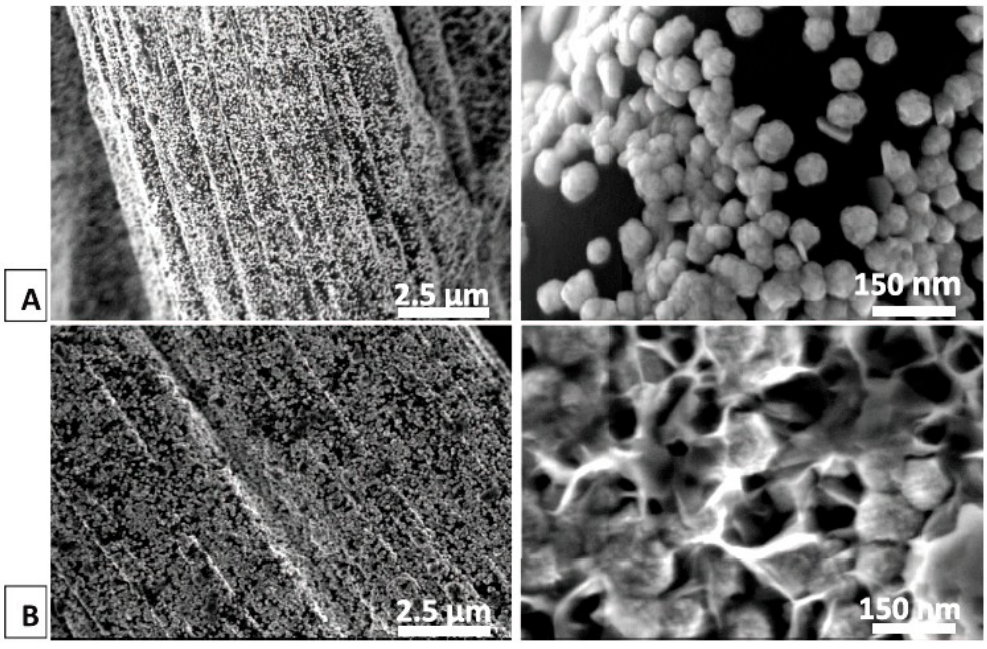

Figure 5.4. SEM images of metal-seeds deposited on carbon fibers of TP with lower and higher resolution on the left and right, respectively. A) Ni seed deposition at pH4. B) Ni and Co seed deposition at pH7.

5.3.2. Carbon nanotube growth

Growth of CNTs on the TP occurred at 750°C by CVD with ethylene as the source of carbon. As expected the Ni-seeds deposited at pH 4 resulted in uniform distribution of CNTs throughout the TP-fibers. An abundant forest of CNTs can be seen in the SEM images of Figure 5.5.C. A visible circular area of growth (Figure 5.5.A) was also observed which corresponds to the circular area of Ni seed nucleation. The CNTs observed under SEM range from 65 nm to 100 nm in diameter. SEM provides visual evidence that the desired result of this growth was achieved and increased the surface area of the TP (compared to plain TP, Figure 5.5.B), similarly to previous reports of CNTs- modified TP employed on an anode design.

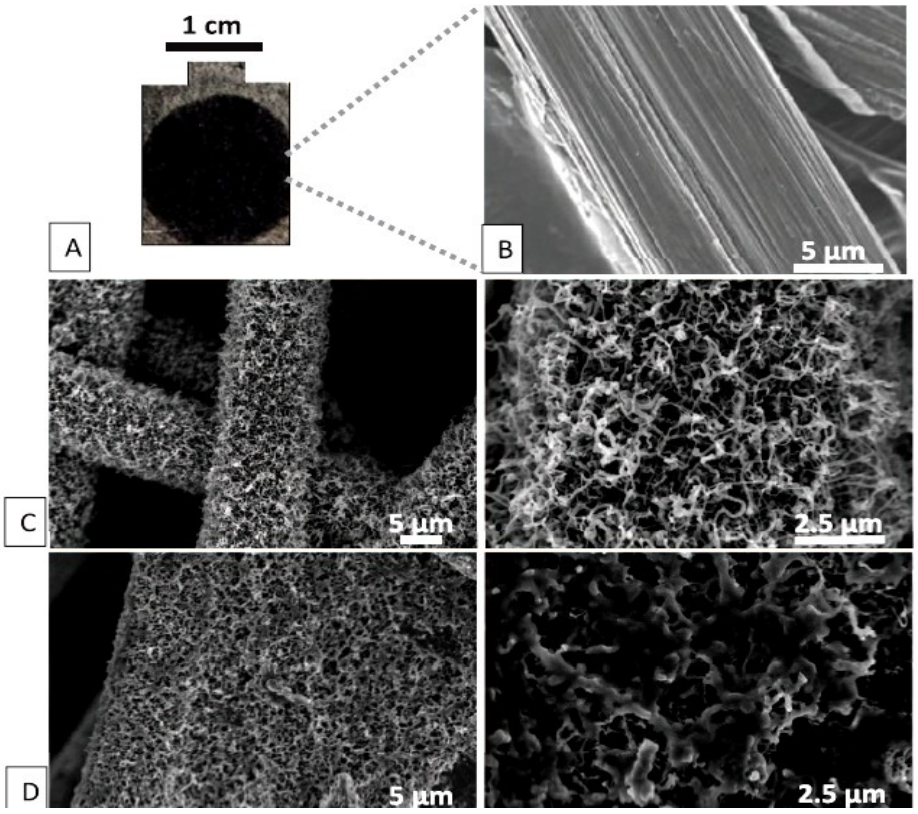

Figure 5.5. (A) (B) SEM image of plain TP (C) SEM images of TP-CNT-BOx cathode, (D)and TP-CNTBOx-TMOS cathode.

5.3.3. pH-dependence study

The BOx-enzyme entrapped in the silica gel matrix on the CNTs-modified TP electrode was subjected to pH dependency study. The performance of the system was analyzed employing K-PB of pH 5, 5.5, 6, 6.5, 7, 7.5, and 8 as electrolytic solutions. The K-PB solution serves as the electrolyte and source of protons needed to reduce molecular oxygen to water at the multi-copper active site of the BOx. When comparing the polarization curves obtained by chronoamperometry, the performance of the biocathode employing the electrolytic solution at low pH shows the highest generated current density (i.e. pH 5.5, Figure 5.6). According to the manufacturer of BOx, the isoelectric point (pI) of the enzyme is at pH 4.1, and pH 6 is the pH at which the enzyme shows optimal activity. Correlating those results, it is possible to determine that the BOx 3D-structure has a net negative charge at pH 5.5 (pH > pI), which, at the same time, is a pH< optimal pH reported by the manufacturer. These results show that the 3D structure of the enzyme obtained by induction of the electronic distribution of the nanoarchitecture of the CNTs-network 3D-silica gel matrix is highly active, enhancing electron transfer and H^+ diffusion at pH 5.5 when compared to the other pHs analyzed herein. The pH of highest performance observed in this study (655 ± 146.18 $\mu A.cm^{-2}$ at 0 V and 345.36 ± 30.04 $\mu A.cm^{-2}$ at 0.3 V for pH 5.5, Table 5.1) is found to be between the pI and the optimal pH reported by the manufacturer (pI 4.1 < pH 5.5 < pH 6).

Additionally, studies have reported that at pH < 7.5 the kinetics of condensation of the silica gel is higher than at basic pH (≥ 8); furthermore, the dissolution of silica gel is kinetically higher at pH > 8. Then, having the electrolytic solution at pH ≤7.5 would confer stability to the silica matrix on the electrode surface, enhancing the enzyme stability in this pH range. At pH 8 the electrode shows the lowest performance (Figure 5.6), which is correlated to dissolution of the

silica gel[185], releasing the enzyme from the surface. The stability of the silica gel as a function of the pH is observed in the behavior/enzymatic performance of BOx in Figure 5.6 where the cathodes show a higher current generation between pH 5 and 7.5 and high decrease of activity at pH 8.

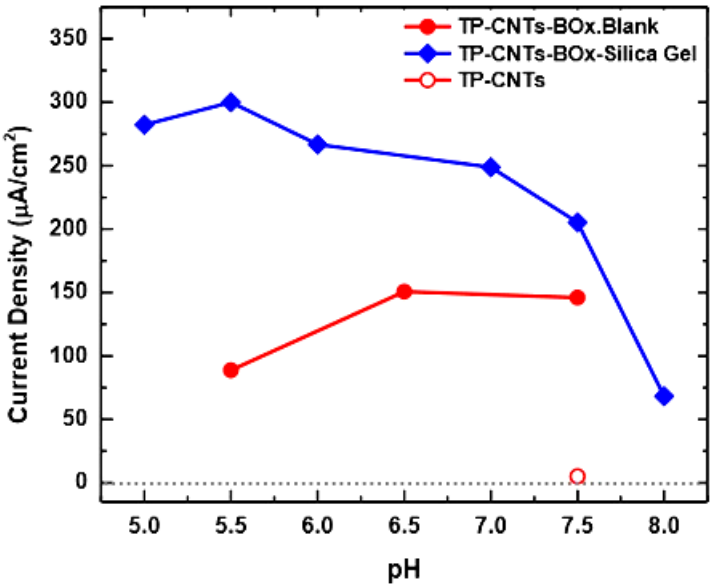

Figure 5.6. PH-dependency study performance points at 0.3 V for the TP-XC35-CNT-BOx-TMOS cathode in phosphate buffer pH range 5 to 8.

Table 5 I. Performance of XC-TP-CNTs-BOx-TMOS at different pH at 0.3 V and 0 V.

pH	Current ($\mu A.cm^{-2}$) at 0.3 V	Current ($\mu A.cm^{-2}$) at 0 V
5	312.77 ± 51.47	495.89 ± 34.63
5.5	345.36 ± 30.04	655.07 ± 146.18
6	266.77 ± 20.37	439.32 ± 29.54
6.5	282.33 ± 69.37	466.81 ± 36.01
7	248.72 ± 46.11	376.06 ± 49.24
7.5	205.37 ± 1.57	287.048 ± 20.37
8	155.1 ± 15.47	148.05 ± 36.7

When compared to other cathode designs, this design shows improved performance versus gas-diffusional cathodes not employing CNTs. At pH 7 the current generated of 248 $\mu A.cm^{-2}$ is increased with respect to previous gas-diffusional designs employing XC35-BOx and

carbon ink-BOx assembled to paper-based microfluidic systems, which generated approximately 197μA.cm^{-2}and 118 μA.cm^{-2}, respectively (at 0.3 V and pH 7). Furthermore, the design shows a current density of 345.56 μA.cm^{-2} at pH 5.5 which is comparable to the performance of cathodes introducing high conductive bucky paper (commercial CNTs-based paper), which show a current output of approximately 345 μA.cm^{-2}at pH 7. The analysis of the performance of the biocathode at physiological pH of 7.5 is of relevance if considering employment of the device in biomedical applications. The polarization curve at pH7.5 (Figure 5.6) presents 287.05 ± 20.37 μA.cm^{-2} at 0 V and 205.37 ± 1.57 μA.cm^{-2}at 0.3 V; statistical analysis show the small standard deviations, showing feasibility and reproducibility of the design (Table 5.1).

5.3.4. Time-dependence study

The CL-nanostructure system was designed to enhance structural stability of the enzyme. Following the procedure specified above, the electrodes were characterized in 6 months of study. Figure 5.7 summarizes our findings, where current density obtained at 0.3V are plotted against time, comparing the biocathode utilizing silica-gel and without silica-gel as entrapment polymeric matrix. Here, the electrodes with silica gel conserve about 80% of their highest performance for up to 6 months. Biocathodes without silica gel, where the enzyme is only physisorbed on the electrode surface, show a decay of their performance within 20 days of testing. These results indicate that engineering the surface of the TP electrodes by CNTs growth in combination with silica-gel formation effectively entraps and maintains the 3D-active structure of the BOx enzyme over a 6-months period.

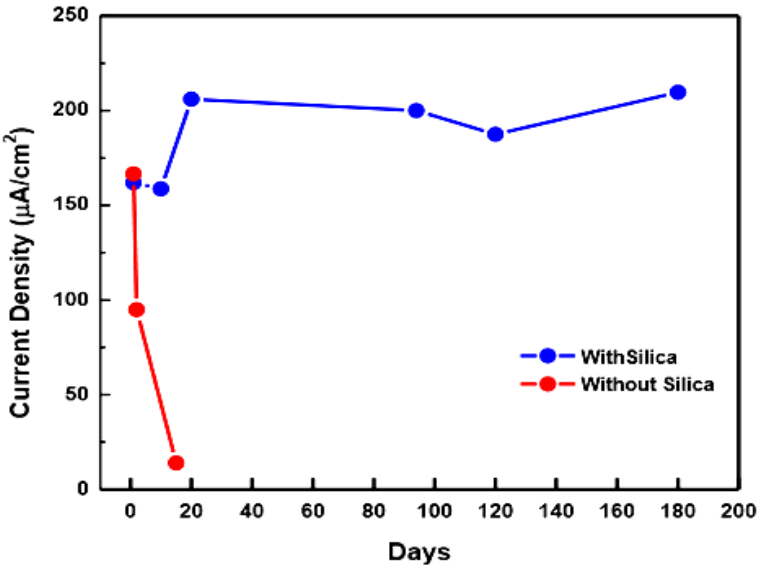

Figure 5.7. Stability study with respect to time, performance points at 0.3 V for the cathode with and without silica in phosphate buffer at pH 7.5.

5.4. Conclusion

This research has shown that the process of growing CNTs on TP is reproducible. The nanostructured architecture of the catalytic layer can be tailored to provide a favorable environment for the active enzymatic structure and confer stability within the range of pH 5 to 7.5. The CNT growth increases the available surface area for increased enzyme loading and a more stable entrapment of the enzymatic structure. SEM observations provide topographic evidence of CNT growth, enzyme adsorption and entrapment. Chronoamperometric experiments done on blank cathodes (i.e. no BOx enzyme) and fully-developed biocathode designs confirm reproducible enzymatic activity with full designs. As the pH of the K-PB buffer was increased from 5 to 8, the performance of the biocathodes varied, reflecting probable conformational changes induced by the environment surrounding the enzymatic structure. The observation may be due to the degradation of the silica gel matrix at a pH higher than 7.5 showing a decrease of current generation (i.e. pH 8), as studies in silica gel reported. Maximum current output was

observed at pH 5.5 while the most consistent and reproducible current density was obtained at a pH of 7.5. At pH 7.5, the cathode performed satisfactorily giving a current density of 205.37 ± 1.47 $\mu A.cm^{-2}$ at the expected operating potential of 0.3 V. This biocathode design is suitable for use in biofuel cells intended for biomedical extracorporeal applications. Furthermore, study of the stability of the design of the catalytic layer confirms active enzyme stability within the 3D CNTs-network/silica-gel matrix throughout 6 months of evaluation. To our knowledge, it is the first time an enzyme is reported to show such stability on a bioelectrode surface.

Chapter 6. Tailored Catalytic Layer for Enzyme Structure Stabilization

6.1. Introduction

Enzymatic fuel cells (EFCs) oxidize organic fuels such as sugars, alcohols, fatty acids and amino acids among others to generate electric energy. These substrates are available for use in the blood stream of living organisms and could be harvested to power implantable medical devices (IMDs). Liquid electrolyte cathodes, fully submerged cathodes operating in non-air-breathing mode, should be designed for IMDs. In this scenario, the biocathodes use oxygen dissolved in fluids of the host organism, such as blood or subcutaneous fluids, where the EFC is implanted. The cathode for such fuel cell applications can be designed to mimic oxygen reduction existing in some living organisms, i.e. some prokaryotes and eukaryotes. In this research we designed various nanoarchitectured catalytic layers (CLs) on carbon composite electrode materials aiming to stabilize the enzymatic oxygen reduction (ORR) system to prolong the lifetime of its 3D-active structure and enhance electron transfer (ET). The stabilization procedures applied to these biocathode designs may also be transferred and adapted to gas-diffusional biocathodes.

The reduction of oxygen (ORR) by multicopper oxidases (MCOs), found in eukaryotes and prokaryotes, is a 4-electron pathway undergoing a direct electron transfer (DET) mechanism. Bilirrubin oxidase from *Myrothecium verrucaria* could be used for implantable applications, under physiological conditions (0.14 M NaCl, pH 7.41) because it is not inhibited by Cl^- (contrarily to Laccase, for example). Also, for implantable devices, the immune response of the organism to the elements present in the EFC is a prevailing factor to consider when the enzyme

immobilization procedure is selected and the cell is assembled. Herein, we aim to develop a biocathode design that successfully overcomes the enzyme stability barriers to promote direct electron transfer (DET). In order to overcome these necessities, the 3-D structure of the enzymes has to be preserved to assure the active site will catalyze the reaction and will do so for a long period of time.

In implantable devices, oxygen would be supplied by the fluids or blood of the organism where the EFC is implanted. In lab tests, oxygen is supplied by pumping oxygen to an electrolytic cell solution within physiological conditions. This research made use of enzyme silica-gel entrapment formed by chemical vapor deposition (CVD) of tetramethyl ortosilicate (TMOS), a technique successfully applied in previous studies for stabilizing organelles, cells, etc.[179] Then, by applying this technique, the catalytic activity and the 3D structure of the enzyme is expected to be maintained. The objective of this research is to create a cathode by entrapment of BOx through CVD of silica gel on the electrode to achieve the catalysis of the ORR within physiological conditions. Additionally, employing this immobilization technique, it is expected the lifetime of the active enzyme can be prolonged for at least one month.

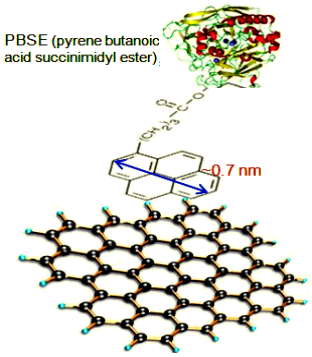

Figure 6.1. PBSE tethered attached to the enzyme by covalent bonds and to the MWNT by π-π interaction to the MWNT.

6.2. Experimental Methods

6.2.1. Apparatus

The electrochemical experiments were performed in a three-electrode cell by conventional potentiostats: Gamry Reference 600 Pontentiostat/Galvanostat/ZRA and Princeton Applied Research VersaSTAT 3 potentiostat / galvanostat. All potentials are reported vs. Ag/AgCl reference electrode. The material characterization was performed using a Scanning Electronic Microscope Hitachi (S-5200).

6.2.2. Materials

Bilirubin Oxidase (BOx) with enzyme unit 2.7 unit/mg was obtained from Amano Enzyme USA Co., Ltd. (Elgin, IL). High conductivity-grade (15-80 μm thickness) bucky paper (HCBP) of purity of ~100% was obtained from Buckeye Composites Inc. (Kettering, OH). Pyrene butanoic acid succinimidyl ester (PBSE, Cat. 457078), Tetramethyl Orthosilicate (TMOS, purity >98%, Cat. 87682), ethanol, and Dimethyl sulfoxide (DMSO) were obtained from Sigma-Aldrich (St. Louis, MO). Monobasic and dibasic potassium phosphates and potassium chloride (KCl) were obtained from EMD Chemicals Inc. KCL and phosphates were used to prepare pH 7.5 buffer 0.1M (KPB) and KCl 0.1M in PB 0.1M stock solutions. Deionized water from Honeywell Burdick & Jackson (Muskegon, MI) was used to make all the electrolytic solutions. All chemicals were used with no further purification. High conductivity bucky paper (HCBP) pieces were plasma cleaned for 12 seconds prior to use if no PBSE tether was used.

6.2.3. Bilirrubin Oxidase Enzyme Immobilization for ORR

In this research, the catalytic layer of the biocathode is designed to overcome time stability and improve electron transfer. Enzymes were trapped in a very porous silica-gel matrix, which was designed to be thin enough to allow electrode surface-electrolytic solution interaction. The formation of the silica-gel matrix is produced by the polymerization of the TMOS precursor in solution as it was stated in earlier research (Chapter 5). 16 sets of biocathodes were created as follows:

1. Enzyme (with and without TMOS and stored at 4ºC and 37ºC)

2. Enzyme + CNTs (with and without TMOS and stored at 4ºC and 37ºC)

3. PBSE + enzyme (with and without TMOS and stored at 4ºC and 37ºC)

4. PBSE + enzyme + CNTs with and without silica-gel, (with and without TMOS and stored at 4ºC and 37ºC).

First, 3cm x 3cm pieces of HCBP were cut. For sets 1 and 2, which used no PBSE, the HCBP pieces were cleaned by oxygen plasma for 12 seconds, to improve hydrophilicity of the material and enzyme interaction. For sets 3 and 4, no prior cleaning was performed; PBSE was used as a tether agent for enzyme immobilization to increase enzyme-electrode interaction. PBSE was dissolved in ethanol:DI water (50:50) and this is used to dissolve PBSE in ratio 2mg PBSE:1ml of solvent mixture. For electrodes integrating additional CNTs (sets 2 and 4), 1 mg of CNTs were mixed in the PBSE solution and sonicated for 30 minutes before use. Then, 793 µl PBSE was deposited on the electrode and left to interact with the "bucky" paper for 2 hours. Later, the electrodes were rinsed with PB 0.1M, pH 7.5, and left to dry, allowing for ethanol

evaporation. For sets 3 and 4, BOx enzyme (19.824 mg BOx) was dissolved in 793µl PB 0.1M, pH 7.5 and deposited on the electrode surface after PBSE deposition. For sets 1 and 2, no PBSE was used and BOx was deposited directly on the electrode. The electrodes were stored overnight at 4ºC or 37ºC. The next day, for electrodes that used no silica-gel, the characterization process started. For biocathodes that employed silica-gel, the catalytic layer was exposed to CVD of TMOS precursor for 5 minutes at room temperature as reported elsewhere. Those biocathodes were also stored at 4ºC or 37ºC as specified above.

The biocathodes were characterized in a conventional electrolytic cell using a glassy carbon cap electrode. A piece 0.5cm in diameter was cut from the larger electrode (3cm x 3cm-batch) and tested. The characterization was performed to determine the reproducibility of the batch, where 5 electrodes were tested at once in day 1 (after overnight storage). The following tests were performed at different time ranges: a) everyday between day 1 to 5, b) every 5 days up to 15 days, c) every 30 days up to month 4, and d) every 60 days up to 14 months.

The electrochemical characterization consisted of open circuit potential measurement, polarization curve development (by chronoamperometries) and cyclic voltammetry. For chronoamperometric tests, controlled potentials were applied while the current was measured. The potentials were applied in 300 second intervals to allow the system to approach a steady state. The potentials were applied from the OCP down to 0V in decreasing steps of 50 mV. For cyclic volatemmetries, scan rates of 10, 20 and 50 mVs^{-1} were applied between -0.6 to 0.7V to observe the ORR process. All electrochemical tests were carried out against Ag/AgCl electrodes and platinum mesh as the reference and counter electrodes, respectively. The electrolytic cell contained 10 ml KCl 0.1M, PB 0.1M, pH 7.5. A continuous flow of oxygen was supplied to the

electrolytic solution during the electrochemical measurements to minimize mass transfer limitations.

6.3. Results

Evaluation of electrodes stored at 37ºC demonstrated that the use of additional CNTs as conductive wires on the electrode surface helps to stabilize the enzymatic system on the electrode surface compared to electrodes that did not use these conductive wires. In figure 6.2, on the left side, from top to bottom, we can compare the polarization curves for HCBP-electrodes with BOx, PBSE-BOx and finally with PBSE-CNTs-BOx. Comparing these electrodes, we can observe that the use of PBSE leads to a decrease in the current density generated or lower ET when electrodes are tested on the 1st day (after 24 hours of their fabrication). When adding CNTs to the layer, the ET is enhanced with respect to HCBP-BOx and HCBP-PBSE-BOx cathodes. On the other hand, at the right side in figure 6.2, it is possible to observe the effect on the PBSE-BOx and PBSE- CNTs-BOx layer when the silica-gel matrix is used to stabilize the 3D active structure. For HCBP-BOx and HCBP-PBSE-BOx with silica-gel, the electron transfer is increased during the first day of testing. For the cathodes utilizing additional CNTs, the current output decreased in density, but the stability of the system improved; this electrode shows small current generation for the 5th and 15th day of testing, which is not observed in the other systems. Even though the systems studied in this step are not stable for more than a few days, the results show the effects of the different components on the biocathode surface and help us to plan the next experimental procedures that involve a change in storage temperature.

For this phase of the study, we continued utilizing the components mentioned above, to analyze their effect on the stability of the enzyme considering that at 37ºC the humidity was not well controlled, and the enzymatic system dried, which may be the leading cause for the enzyme denature.

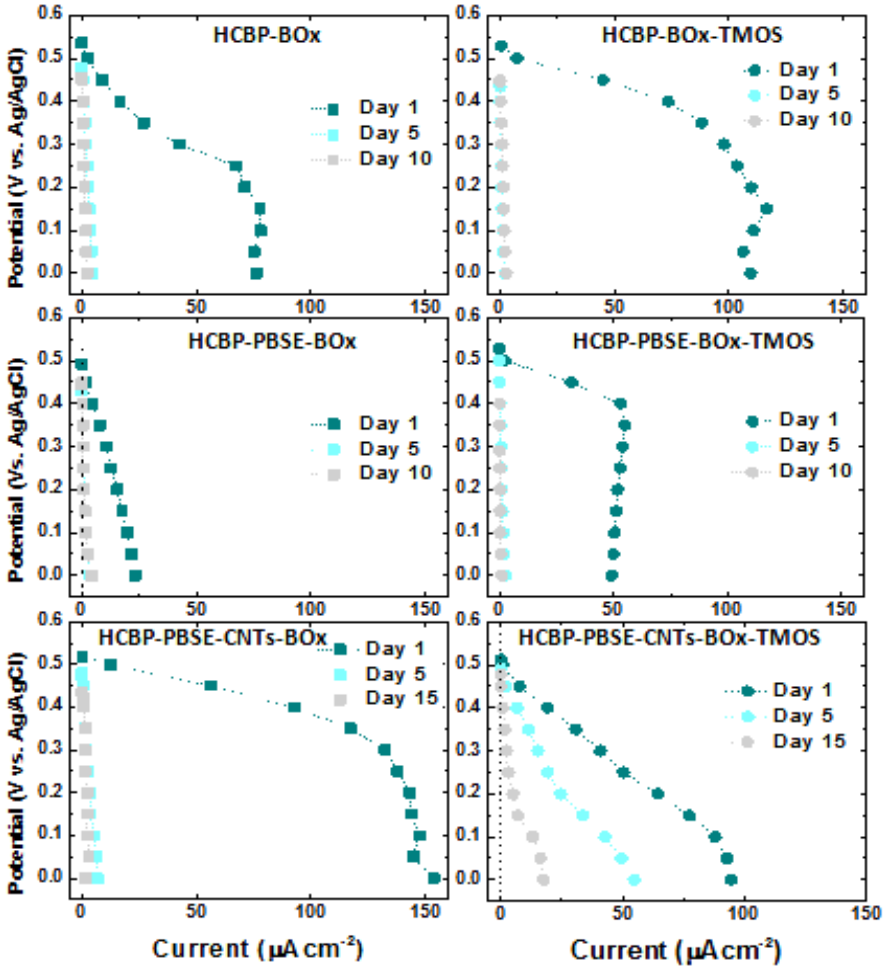

Figure 6.2. Polarization curves of biocathodes stored at 37°C. The electrode employing CNTs shows the highest current density at the first day of testing (HCBP-PBSE-CNTs-BOx).The use of CNTs and silica-gel on the electrode surface (HCBP-PBSE-CNTs-BOx-TMOS) helps to stabilize the catalytic layer for a prolonged period of time for electrodes stored at 37°C.

At 4ºC, the electrodes effectively maintained their performance for ORR for a prolonged period of time. For the initial days of the experiments, the thermodynamic potential

measurements showed the biocathodes employing BOx-silica gel, the combination of CNTs-silica gel, and PBSE-CNTs-silica gel were more reproducible and stable over a larger time frame (red label, Figure 6.3). Moreover, the best performing electrode when looking at the OCP measurements is the HCBP-PBSE-CNTs-BOx-TMOS cathode (red label, Figure 6.3.D). Also, SEM images show the different morphologies from electrode integrating CNTs, PBSE linker and silica gel (Figure 6.4). The biocathode integrating CNTs and CNTs-TMOS demonstrate the formation of agglomerates of CNTs on the HCBP surface. These agglomerates are believed to contain the enzymatic system allowing enzymatic stability. These also worked as wires to the HCBP for enhanced ET.

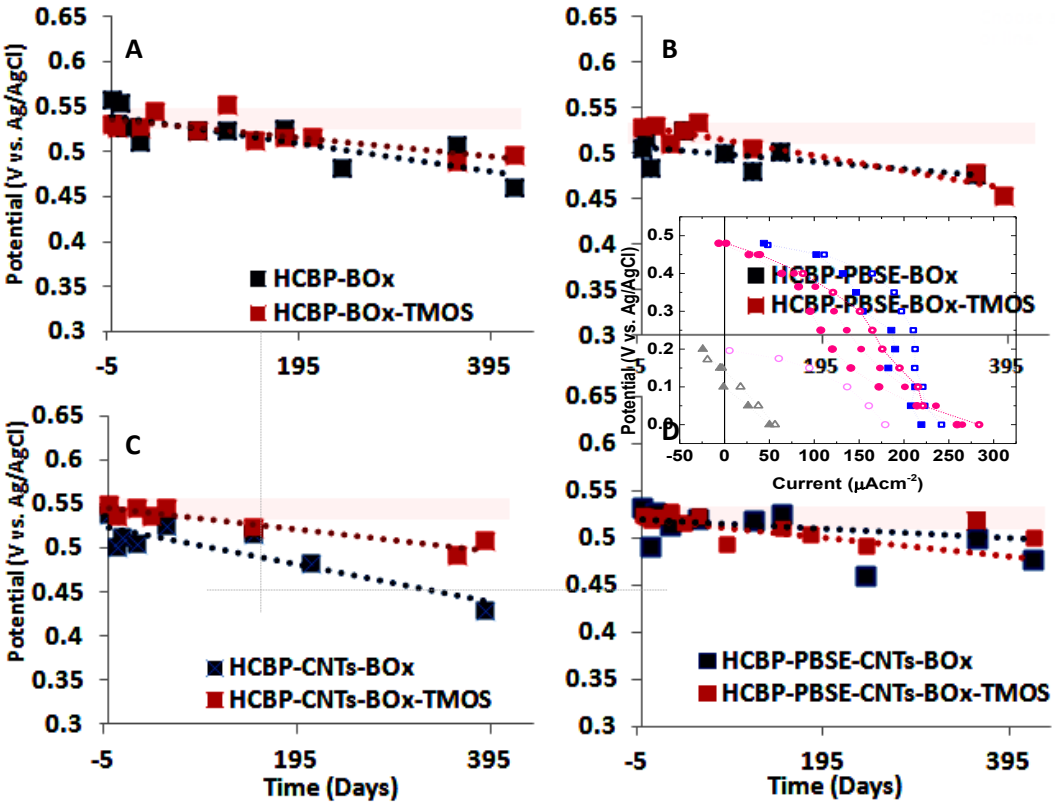

Figure 6.3. Open circuit potential measurements as function of time for biocathodes stored at 4°C in humid conditions. Biocathodes integrating CNTs added to the bucky paper surface, PBSE linker and silica-gel entrapment (HCBP-PBSE-CNTs-BOx-TMOS) maintains shows the smaller decrease in OPC in (D) above.

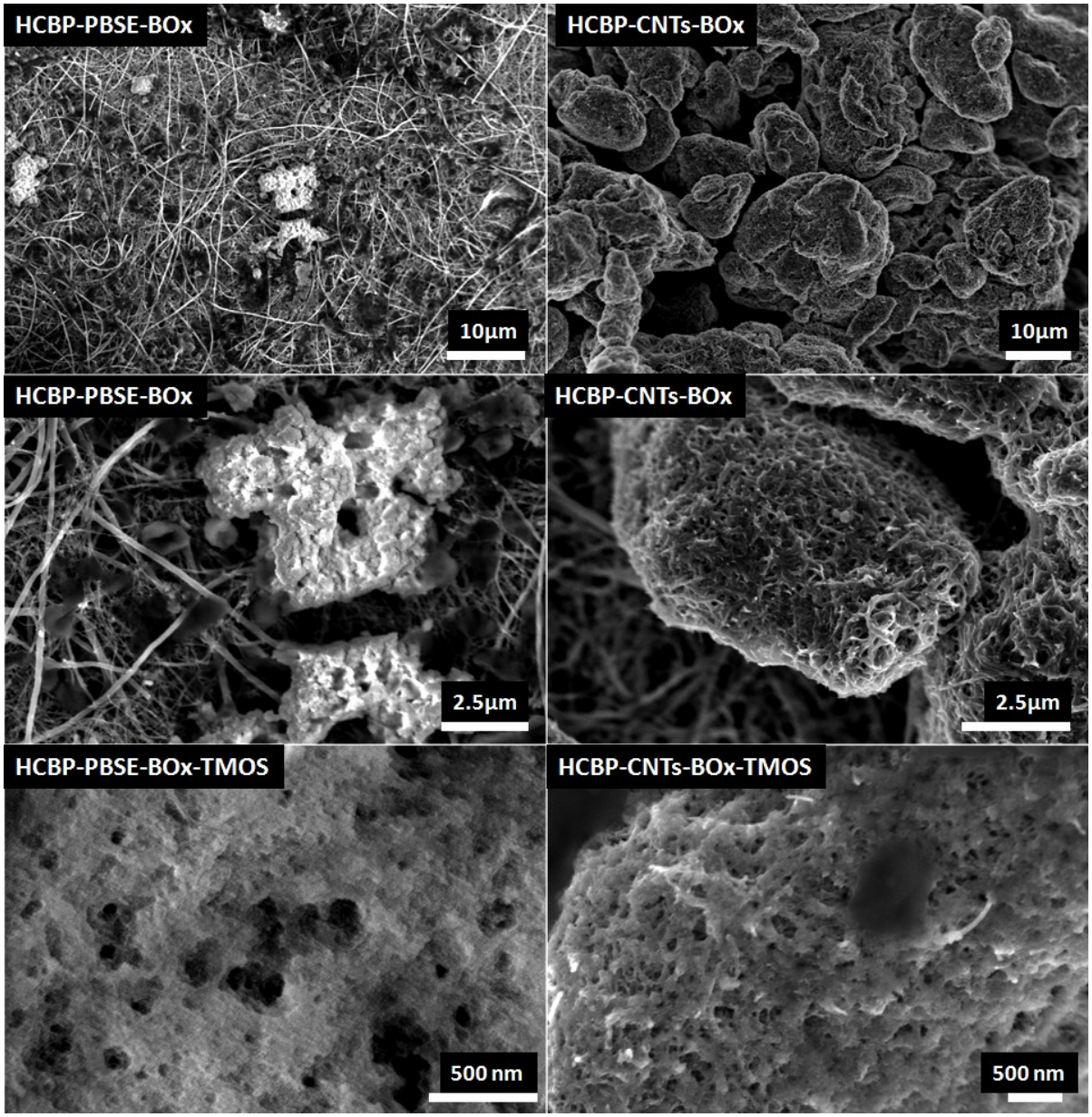

Figure 6.4. SEM Images of HCBP-PBSE-BOx and HCBP-PBSE-BOx-TMOS, and HCBP-CNTs-BOx and HCBP-CNTs-BOx-TMOS (samples stored at 4°C. in humid conditios).

Looking at the kinetic of the biocathodes, the systems with an increased ORR rate, with higher ET, are systems integrating CNTs and silica-gel as depicted in figure 6.5 (HCBP-CNTs-BOx-TMOS). The cyclic voltammograms utilizing the PBSE-tether, CNTs and TMOS, obtained

at the same conditions after 360 days of storage are compared. The red curve in figure 6.5, representing the catalytic layer using BOx-CNTs and BOx-silica gel, shows the best performance compared to HCBP-BOx and HCBP-PBSE-CNTs-BOx-TMOS. The reduction peak is at ~-0.4V and 820μAcm^{-2}. Oxidation processes are also at ~ -0.3V, 400 μA.cm^{-2} and 0.1V, 420 μA.cm^{-2}.

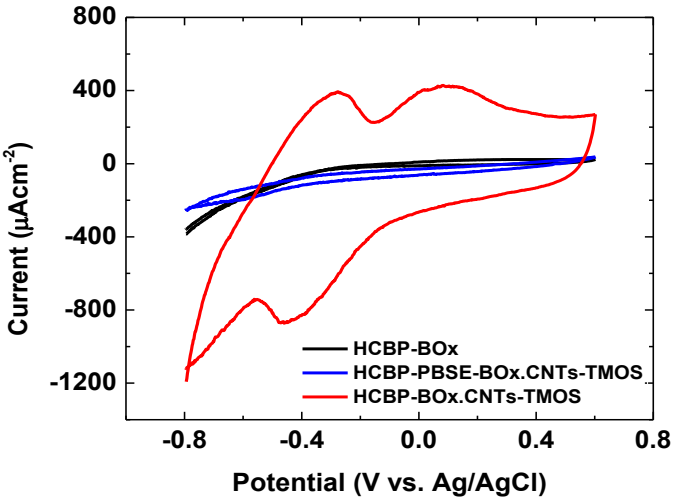

Figure 6.5. Cyclic voltammetry (CV) of HCBP-based biocathodes using a scan rate of 20mVs^{-1}, CV was performed on the 360th day of storage at 4 °C in humid conditions. Biocathodes integrating CNTs added to the bucky paper surface and silica-gel entrapment (HCBP-CNTs-BOx-TMOS) shows a reduction peak at ~-0.4V and -820μA.cm^{-2} which is significantly higher than for HCBP-BOx AND HACB-BOx-CNTs-TMOS electrodes under similar testing conditions.

The electrodes were evaluated through chronoamperometry. For these measurements, a potential was applied while the current generated was monitored (not shown). Later, these results were used to gather the information about the current generated at the specific potentials applied. In this research, the performance of the electrodes was compared at 0.25V. The current generated at this potential was plotted as a function of the time of storage, represented in figure 6.6. This graph shows the current output of the set of electrodes studied above (figure 6.6) evaluated between 360 or 420 days.

From the figure 6.6, top graphs from left to right, we are able to observe that biocathodes utilizing PBSE and TMOS show a higher current density generated within 100 days of storage. After that time, the catalytic layer losses its slightly enhanced ET behavior, decreasing current output. Looking at the right graphs from top to bottom, the biocathodes using CNTs in addition to PBSE tether and TMOS (employed for enzyme immobilization) show an increment in current generation, which can be explained by the increase in the conductive surface allowing for higher active site-CNTs interaction and ET.

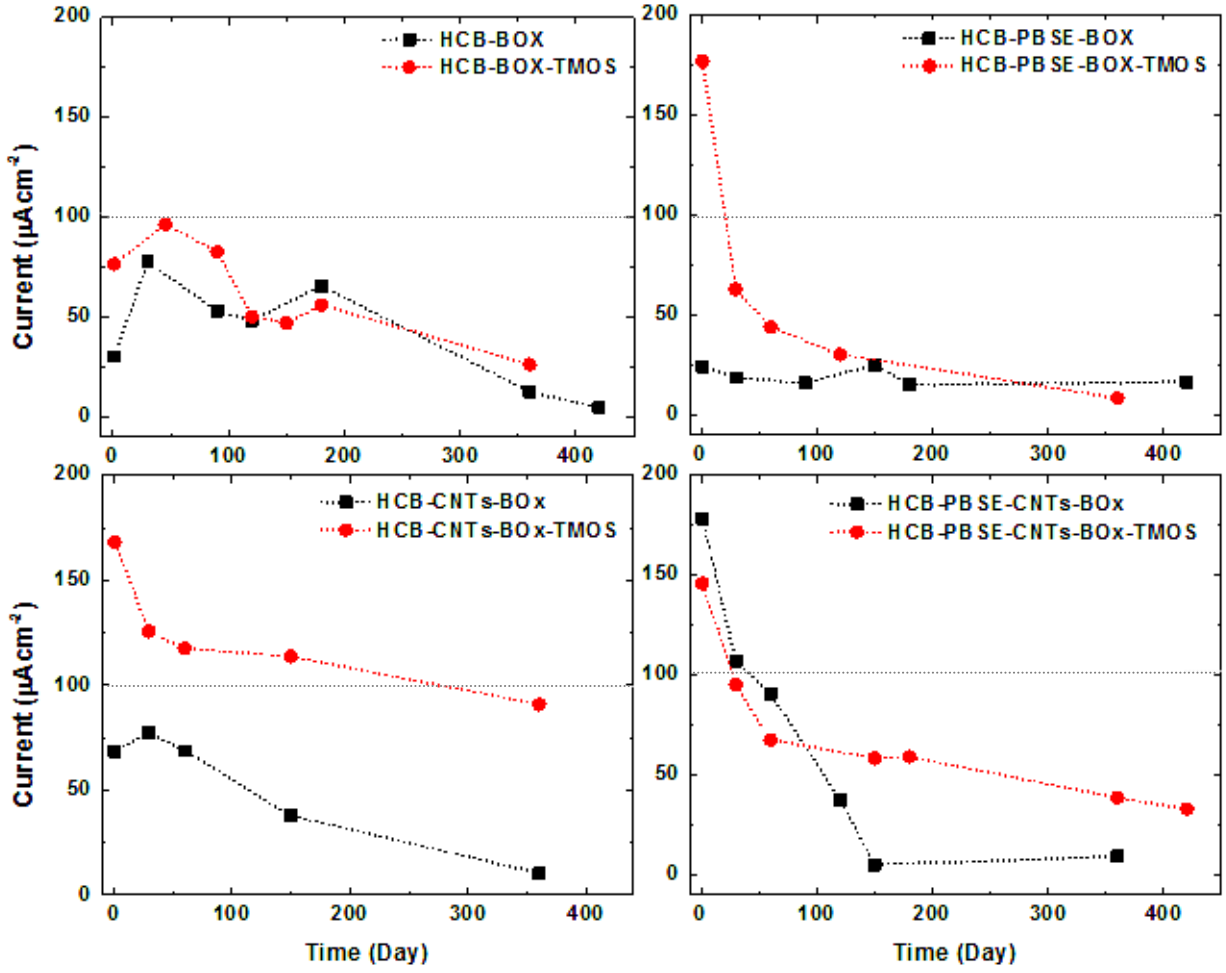

Figure 6.6. Current density at 0.25V, measured as function of time for biocathodes stored at 4°C in humid conditions. Biocathodes integrating CNTs added to the bucky paper surface, PBSE linker and silica-gel entrapment (HCBP-PBSE-CNTs-BOx-TMOS) maintains shows the smaller decrease in OPC in (B) above.

Finally, comparing the plots at the left in figure 6.6, from top to bottom, and the ones at the bottom (from right to left), we see that the catalytic layer maintained ~65% of its initial performance after 150 days of storages and ~50% after 360 days of storage. Increasing the conductive surface and creating a conductive network within a silica-gel matrix, the active 3D-structure of the BOx enzyme is maintained for prolonged periods of times compared to other architecture of the catalytic layers.

These results allow us to speculate that the 3D-structure of the enzyme is maintained within the porous structure of the silica-gel due to an optimum balance of molecular interactions (van der Waals, hydrophobic, hydrophilic, ionic interactions) of the enzyme with its surroundings while the water content and the porous dimensions are maintained. This is further supported by the fact that that the gellation process for the silica matrix is a process very slow at the given temperature (4ºC) and pH 7.5 and the optimal silica gel conformation to maintain the enzymatic structure active, shown by previous research. Then, understanding each component of the catalytic layer and its effect on the enzymatic structure at a molecular level could help us design and control those parameters to tailor the optimum nanostructural architecture of the entrapment matrix for enhanced structural stability and performance of the enzyme.

6.4. Conclusion

This study has demonstrated the relevant role of the 3D-CNTs network and the silica-gel matrix in an engineered catalytic layer for enhanced structural stability of the enzyme and ET. This research developed a biological catalytic layer for ORR that maintained 65% of its initial performance for 150 days and ~50% of its performance within 360 days of evaluation. This biocathode design can be applied to EFC for biomedical applications.

Chapter 7. Nanomaterial-Based Bioanode and Gas-diffusional Biocathode Encapsulated in Polydimethylsiloxane

7.1. Introduction.

Contact lenses, transparent biocompatible polymeric biomedical devices (BMDs), are mostly used to correct faulty vision and as an aesthetic accessory. However, studies have stated that contact lenses could be employed as a platform for health monitoring, drug delivery and super vision devices. Lately, devices designed for health monitoring, for example sensors for measuring eyelid pressure or intraocular pressure by electroretinogram, and tear glucose concentration have been successfully assembled into contact lens designs.[103, 152, 153, 186] Furthermore, drug delivery systems are being studied for controlled drug-dosage administration to improve eye treatment and avoid any collateral effects of the drug that traditionally would reach other tissues in the nasolachrymal system.[187] Some designs of health monitoring, drug delivery and super vision systems require the integration of a power source.

Recent studies have focused on the development of enzymatic biofuel cells (EFC) as power source devices to harvest energy from physiological components found in the tear film on the eye of the host organism.[103, 153] These physiological components (glucose, lactate, ascorbate, pyruvate, dopamine and urea)[153, 188, 189] can be oxidized by enzymatic systems on the bioanodes while, simultaneously, the enzymatic system on the biocathode reduces oxygen. EFC devices that utilize glucose as a biofuel are a promising alternative for electric power sources for contact lens integration because lachrymal fluids or tear fluids contain glucose levels in the range of 0.1-0.6 mM [122-124] and these fluids are accessible on the eye's surface. Additionally, glucose depletion has apparently no effect on the cornea tissue.[103] At the concentration of glucose found

in lachrymal fluids, its conversion to gluconic acid with a 2-electron transfer (ET) process was demonstrated to be feasible and capable to satisfy energy demands for microdevices on the contact lens.[125-127] Utilizing a reagentless bioanode that integrates nicotinamide adenine dinucleotide (NAD^+/NADH) - dependent glucose dehygrogenase (GDH), its tethered cofactor (NAD^+/NADH), and multiwalled carbon nanotubes (MWNTs)-based bucky papers could satisfy the demand of current generation of a micro or nano BMD.

On the other hand, the reduction of oxygen at the cathode surface has been shown to be achievable by bilirubin oxidase (BOx), a multicopper oxidase, generating water as a product.[91, 139] This enzymatic system can undergo a direct 4-electron transfer mechanism (DET) and has shown significant enzyme-carbon nanotube interaction which enhances ET.[139-142] The development of passive air breathing cathodes has greatly advanced dual-layered cathode designs for enhanced oxygen flow from air to the catalytic layer.[120, 140, 143, 144] The catalytic layer of the biocathode needs to be engineered to stabilize the enzymatic systems and to enhance ET and ionic/charge exchange between the active site of the enzymes, the electrode's surface, the electrolyte and molecular oxygen. Immobilization of the BOx can be achieved by utilizing silica-gel as an entrapment matrix to preserve the stability of the active 3D-structure of the enzymatic systems and to ensure the close proximity of the active site of the enzymes to the electrode surface while allowing particle and fluid exchange within the electrolytic solution. Furthermore, using the natural substrate of BOx, bilirubin, on the surface of the electrode would orient the active site of BOx towards the electro surface enhancing ET. Silica-gel[48, 129, 140] matrix has been studied in previous research resulting in improved performance and the prolonged life time of the enzymes in storage when compared to preliminary designs.

A contact lens-enzymatic fuel cell (CL-EFC) should be designed to use oxygen from air to avoid depleting oxygen from the cornea tissue, which would lead to vision impairment.[103, 145-149] For other extracorporeal applications such as EFC-patch designs, the cathode must allow oxygen transfer and be encapsulated within a biocompatible and bioinert material to avoid triggering an immune response from skin tissue. Thus, the state-of-the-art technology on air-breathing cathode and glucose-based anode designs should be transferred and adapted to the EFC for BMD applications for *ex-vivo* or extracorporeal use.

The material encapsulating the cathode and the anode should be biocompatible and avoid triggering the host's immune system. For this reason, we considered materials that have been widely tested for decades and fulfill the requirements of the Food and Drug Administration (FDA) for extracorporeal-BDM use, which is the case of contact lens polymers. The contact lenses' materials consist of biocompatible three-dimensional, amorphous, polymeric matrices. One of these polymers is polydimethylsiloxane (PDMS).[152-155] PDMS has been shown to be successfully used as a bioinert and biocompatible material in commercial contact lenses. It is a silicone-based hydrogel that confers the contact lens with efficient oxygen permeability, high wettability, resistance to biofilm formation (observed in non-silicon based hydrogels) while retaining eye comfort.[24]

From the electrode design perspective, the materials for electrodes should satisfy design criteria to enhance electrical conductivity, provide stabilizing interactions with the oxidoreductase enzymes, have a high surface-to-volume ratio to allow for high enzyme loading, and contain sufficiently large pore size to facilitate efficient mass transport of oxygen.[125, 126, 156] Multiwalled carbon nanotubes (MWNTs) are materials with attractive properties (high electrical conductivity, thermal and chemical stability, and mechanical strength) and demonstrate efficient

interactions with enzymes.[127, 157-160] Moreover, MWNTs-based "bucky" papers are commercially available [161, 162] and have shown enhanced ET due to high conductivity and porosity.[163, 164] Although carbon nanotube-based materials might not be biocompatible, the fuel cell can be designed to fulfill biocompatibility requirements for the intended biomedical application.

This research introduces both the design of an air-breathing biocathode and glucose-based bioanode. The biocathode utilizes high conductive "bucky" paper (HCBP) as an electrode material and BOx integrated into a PDMS-polymeric matrix. Entrapment procedures of BOx on silica gel and the orientation of the active site of BOx using its natural substrate (bilirubin) on the electrode surface were explored. The reagentless bioanode uses CMN-grade "bucky" paper and GDH with its tethered NAD^+/NADH- cofactor, also encapsulated in a PDMS matrix. The electrochemical performance of the design was analyzed utilizing a paper-based microfluidic system. The resulting technology could easily be transferred to CL-EFC and other EFC applications.

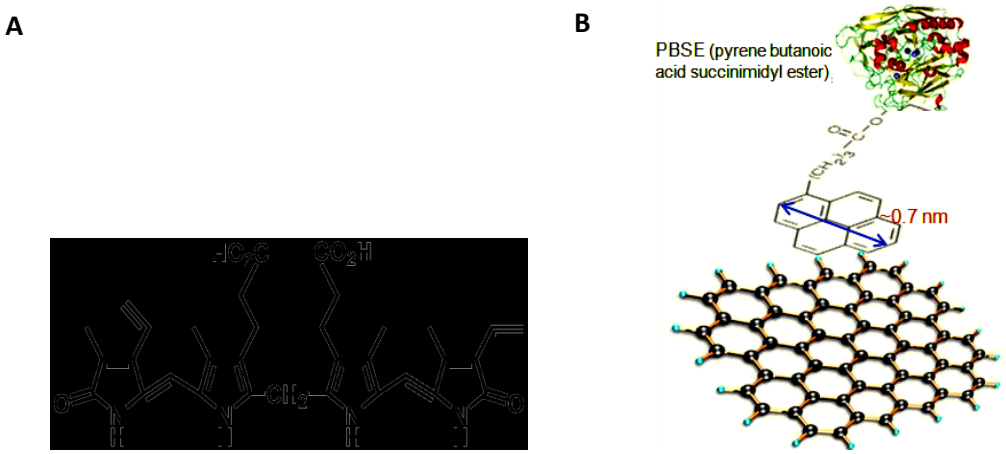

Figure 7.1. A) Bilirubin molecular structure, B) PBSE tether bonded to enzyme and interacting with the MWNTs wall by π-π interaction.

7.2. Experimental Methods

7.2.1. Apparatus

The electrochemical experiments were performed in a three-electrode cell by conventional potentiostats: Gamry Reference 600 Pontentiostat/Galvanostat/ZRA and Princeton Applied Research VersaSTAT 3 potentiostat / galvanostat. All potentials are reported vs. Ag/AgCl reference electrode. The material characterization was performed using a Scanning Electronic Hitachi Microscope (S-5200).

7.2.2. Materials

Bilirubin Oxidase (BOx) with enzyme unit 2.7 unit/mg and lyophilized Glucose Dehydrogenase (GDH, 272 U/mg activity) were obtained from Amano Enzyme USA Co., Ltd. (Elgin, IL). High conductivity-grade (15-80 μm) and CMN-grade (15-250 μm) bucky paper of purity of ~100% were obtained from Buckeye Composites Inc. (Kettering, OH). Isopropanol (purity >99%), potassium chloride (KCl), monobasic and dibasic potassium phosphates were obtained from EMD Chemicals Inc. Phosphates were used to prepare pH 7 and pH 7.5 buffer (KPB) stock solutions. Methylene Green (MG) Zinc Chloride double salt (purity >99%, from Fluka Cat. 66870) and KNO_3 from EMD Chemicals Inc. were used to make MG growing solution in PB of pH7. Nicotinamide adenine dinucleotide (NAD^+, purity ~98%, Fluka Cat. 43407), D(+)-Glucose (purity >99.5%, Cat. G7528), Pyrene butanoic acid succinimidyl ester (PBSE, Cat. 457078), Tetramethyl Orthosilicate (TMOS, purity >98%, Cat. 87682) and Dimethyl sulfoxide (DMSO) were obtained from Sigma-Aldrich (St. Louis, MO). Paper-based setup consisted of Filter Paper from VWR International (North American Cat. No.:28310-128) with a 15cm diameter. For the cathode, the circuitry of the cell was painted on the filter paper

with PELCO © Colloidal Graphite water-based, isopropanol-based, and Fast Drying Silver Paint (silver in iso-butyl methyl ketone) from TED PELLA, INC. (Redding, CA). Scotch (3M St. Paul, MN) packaging tape (clear) was used as a laminate to hold the electrode in place along with generic painted paper clips. For the anode, the carbon fiber was replaced by nickel mesh and no additional paint was used. Deionized water from Honeywell Burdick & Jackson (Muskegon, MI) was used to make all the electrolytic solutions. All chemicals were used with no further purification.

7.2.3. Bioanode Fabrication

First, CMN-based bioanodes for glucose oxidation were developed. MG was polymerized on the CMN-paper of 3.7 cm^2 (procedure described in previous work by cyclic voltammetry[133]), rinsed with water after polymerization and left to dry. Secondly, NAD^+ was tethered on the electrode surface. For this, separately, PBSE was dissolved in DMSO (2.9 mg/100 µl) and NAD^+ cofactor was dissolved in a phosphate buffer (PB) 0.1M at pH 7.5 (5 mg/100µl), and later both solutions were mixed. The amount of PBSE and NAD^+ used maintained the 1:1 molar ratio. The mixture was deposited on the MG-polymerized CNM electrode and left to rest for 2 hours. After, the electrode was rinsed with PB and left to dry. By then, 3 mg of GDH was dissolved in 150 µl of PB 0.1M, pH 7.5 and drop-casted on the electrode and left to rest for 2 hours. PDMS was drop-casted on the electrode and left to polymerize on the electrode surface following the procedure specified in previous work (10 parts PDMS: 1 part curing agent) and the curing process was at ~25ºC for 24 hours. The electrodes were assembled to a 2D-microfluidic system for testing as reported in previous studies, in a half-cell configuration, using platinum and Ag/AgCl as reference and counter electrode, respectively.

7.2.4. Biocathodes Fabrication

The cathode designs were developed to evaluate the influence of the electrode material, the effect of bilirubin as an orienting agent for BOx, the influence of silica gel as an enzyme entrapment matrix and the permeability of PDMS to passively flow oxygen to the catalytic layer. "Bucky" paper pieces were cleaned with oxygen plasma for 12 seconds prior to use. All electrodes ($2cm^2$) used 5 mg of BOx in 200 µl PB 0.1M, pH 7.5. Also, a rectangular section of the materials (2cm x 1cm) was treated to create a catalytic layer while an adjacent (0.5cm x 1 cm)-'tail' was used as a contact for electrode testing.

The firsts set of electrodes were made with CMN and HCBP, using bilirubin as an orienting agent for the enzyme and CVD of TMOS for 5 minutes. 1) The influence of the solvent of bilirubin was analyzed and PBSE was explored as a tether for BOx. PBSE and bilirubin were dissolved in the solvent (DMSO or ethanol) in the ratio 2mg bilirubin:1 mg PBSE:1 ml solvent. Later, 100 µl of the solution was deposited on the electrode and left for 2 hours. Then, the electrode was rinsed with PB 0.1M, pH 7.5 and left to dry. The enzyme was deposited on the dried electrode, and the electrode was stored at 4ºC overnight before evaluation. 2) The performance of BOx in silica-gel matrix was analyzed. For that, CMN and HCBP with bilirubin were exposed to CVD of TMOS as stated in previous research.

The second set of electrodes integrated the CMN and HCBP electrodes in a polymeric matrix of PDMS that was synthesized as stated above in a bioanode fabrication section.

1) BOx was deposited on the HCBP electrode kept at 4ºC overnight. On the second day, the HCBP-BOx electrode was entrapped between layers of PDMS (~200 µm) and kept at room temperature (22ºC) for 24 hours.

2) Similarly to the previous step, the enzyme deposition process was carried out. However, after storing the HCBP-BOx electrode overnight, TMOS was deposited by CVD for 5 minutes and the electrode was also stored overnight at 4ºC. After, PDMS layers were used to encapsulate the electrode. The biocathode was assembled in a half cell setup in a 2D-microfluidic system as well. For the cathode, the catalytic layer was exposed to air. The bioanode was fully covered. The fan-'leg' was introduced to the electrolytic solution which displaced through the cellulose paper-based microfluidic system, imbibing the catalytic layer.

7.2.5. Electrochemical Characterization

The electrodes were evaluated by chronoamperomeric measurements after determining the open circuit potential (OCP). The chronoamperometries were performed from OCP down to 0V for the cathode, and from OCP up to 0.35V for the anode. Cyclic voltammetry was employed in the characterization as well. The resulting data from the chronoamperometries were used to develop the respective polarization curves for performance analysis and comparison.

7.3. Results

Bucky papers are WMNTs-based papers fabricated employing different ranges of carbon nanotubes that give the Bucky papers different nanoarchitectural properties. Figure 7.2 shows how the CMN paper (thickness ~200 μm) is formed by a blend of nanotubes with diameter ~10 nm and 100-200 nm compared to HCBP paper, which is formed by MWNTs of more uniform diameter distribution (paper thickness ~40-60 μm).

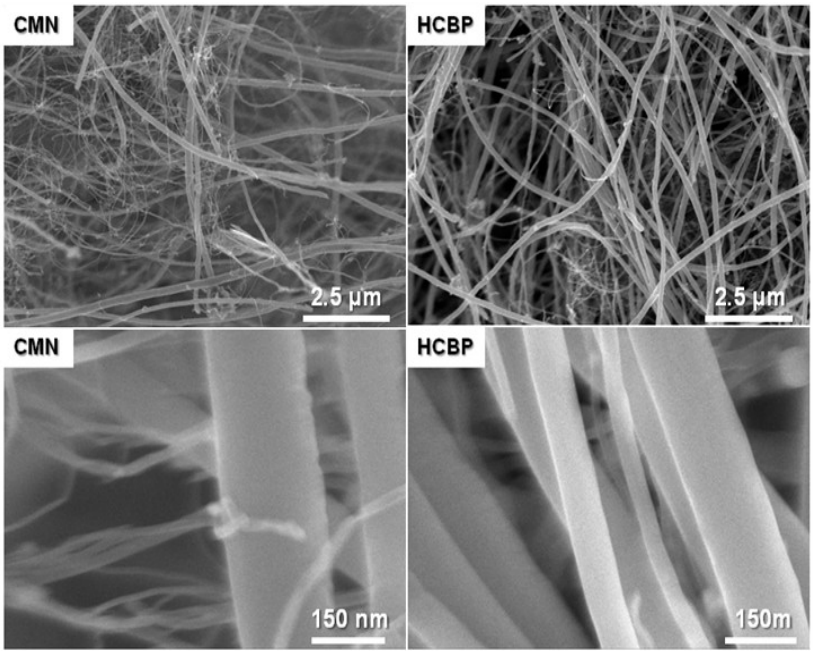

Figure 7.2. SEM images of CMN and HCBP. CMN present a higher content of MWNTs with a small diameter (~10nm) compared to HCBP which shows a larger distribution of MWNTs with a large diameter (~100-200nm).

7.3.1. Bioanode Evaluation

Reagentless CMN-based bioanodes for glucose oxidation were developed and electrochemically characterized in a half-cell configuration assembled to a 2D-microfluidic system. The enzyme employed in this step of the research was NAD^+/NADH-dependent GDH. Since the enzyme utilizes the NAD^+/NADH cofactor, MG was electrodeposited on the electrode surface and utilized as a mediator for the NADH regeneration to NAD^+, following a standard procedure. Later, the NAD^+ form of the cofactor was immobilized on the electrode employing PBSE as a tethering agent. The GDH enzyme was deposited on the electrode and entrapped between a PDMS matrix as indicated in the experimental section. After 24 hours of curing time at room temperature, the electrode was tested in the presence and absence of its substrate (glucose 0.1M, KCl 0.1M, PB 0.1M and Kl 0.1M in PB 0.1M, respectively, at pH 7.5).

The electrochemical characterization of the bioanodes was performed in both cell configurations: conventional electrolytic cell and fan-shape paper-based cell. When, the electrode was tested in absence of glucose, the cyclic voltammetries at 10 mVs^{-1}(figure 7.3.A) show that the $NADH/NAD^+$ cofactor undergoes oxidation and reduction processes depicted as anodic and cathodic peaks at ~-0.2V and -0.25V respectively. The current densities at these redox peaks are larger than when glucose substrate is present in the system, indicating the ET from the $NADH/NAD^+$ system is also involved in the redox process where the GDH enzyme is participating. ET between the enzyme and the cofactor increased due to the oxidation of the glucose. The oxidation peak of glucose is observed at 0.4V and 720$\mu A.cm^{-2}$; the peak is at a higher potential compared to previous systems where the cofactor is in solution (0.22 V with a current of approximately 3.3 mA for 3.7cm^2 for GDH in chitocan/CNTs polymeric matrix electrode in chapter 3).

Also, the curve in the blank solution shows participation of redox processes involving $NADH/NAD^+$ reflected as increased current generation for this system compared to the system where the cofactor is in solution. The GDH-enzyme surrounded by the new PDMS matrix has a slower kinetic activity, decreased ET; this is also observed in the polarization curve for the fan-shape paper-based setup in figure 7.3.B when compared to results seen in previous studies (chapter 4, Figure 4.6). However, the bioanode works in reagentless conditions surrounded in a PDMS biocompatible polymer (FDA approved), which improves the design for the intended biomedical applications.

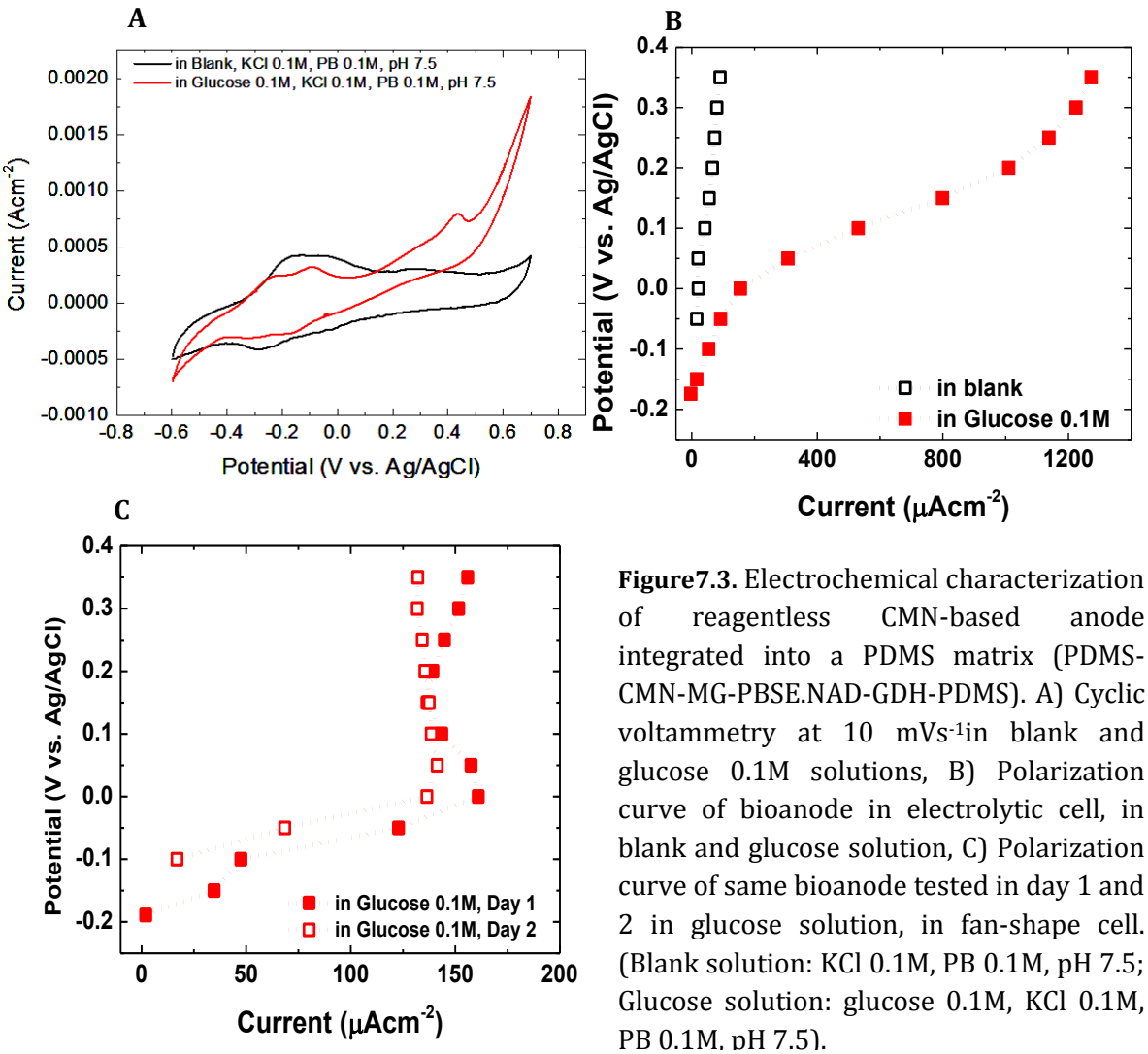

Figure7.3. Electrochemical characterization of reagentless CMN-based anode integrated into a PDMS matrix (PDMS-CMN-MG-PBSE.NAD-GDH-PDMS). A) Cyclic voltammetry at 10 mVs^{-1}in blank and glucose 0.1M solutions, B) Polarization curve of bioanode in electrolytic cell, in blank and glucose solution, C) Polarization curve of same bioanode tested in day 1 and 2 in glucose solution, in fan-shape cell. (Blank solution: KCl 0.1M, PB 0.1M, pH 7.5; Glucose solution: glucose 0.1M, KCl 0.1M, PB 0.1M, pH 7.5).

Even more significantly, a PDMS matrix helps to improve the stability of the tethered cofactor at the surface of the electrode without employing a chitosan/CNTs matrix as used previously (chapter 4). The integration of chitosan/CNTs matrix resulted in negligible current density generation which may be due to the larger thickness of the polymeric matrix (chitosan/CNTs + PDMS) that made the active site inaccessible for glucose in solution or ET (not shown). As a result, only the PDMS matrix was used in the design. This catalytic layer was effectively operating under reagentless conditions for 2 days (figure 7.3.C) in the conventional electrolytic cell setup.

7.3.2. Bilirubin as Orienting Agent for Bilirubin Oxidase

The use of a solvent for an analyte constituting the catalytic layer of the electrode is of relevance to ensure complete dissolution of the said compound, allowing ET enhancement. Even more, the solvent remaining on the electrode must not have a negative effect on the enzymatic system or other compound involved in the performance of the electrode. Because of this, the biocathodes were evaluated looking at the effect of the solvent for bilirubin and PBSE. CMN-PBSE-Bil-BOx and CMN-PBSE-Bil-BOx-TMOS were fabricated utilizing bilirubin dissolved in DMSO and ethanol (Eth) and evaluated for 4 days (Figure 7.4). Ethanol is used because it is expected to evaporate from the catalytic layer. Figure 7.4 shows the performance of the electrodes at 0.3V and their behavior during 4 days of analysis by chronomaperometric measurements (used to develop the respective polarization curve, not shown). The results show the best performance when ethanol is used as a solvent for bilirubin and PBSE, generating a higher current density when compared to electrodes using DMSO. Furthermore, the silica-gel formation on the biocathodes was shown to stabilize the current generated.

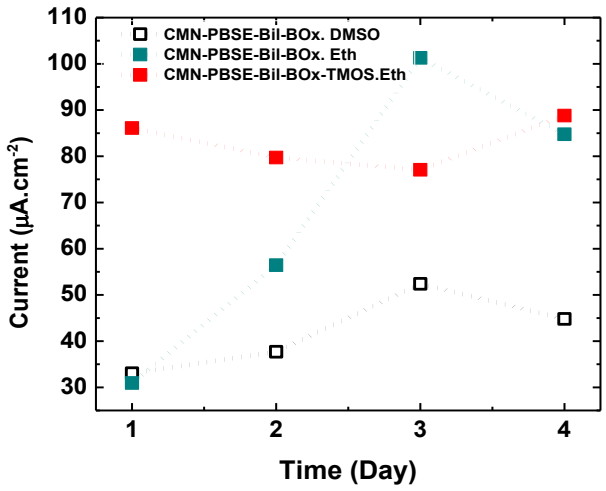

Figure 7.4. Current density at 0.3V as function of time for biocathodes utilizing DMSO and ethanol as solvents for bilirubin and PBSE. CMN-PBSE-Bil-TMOS shows more stability and higher current density generation.

7.3.3. Biocathode Material Evaluation. CMN and HCBP Electrodes

The effects of a) bilirubin as an orienting agent and b) the entrapment matrix of silica-gel on the performance of the CMN and HCBP-based biocathodes assembled to the fan-shape microfluidic system were analyzed. The electrodes were created under similar conditions and subject to similar characterization procedures.

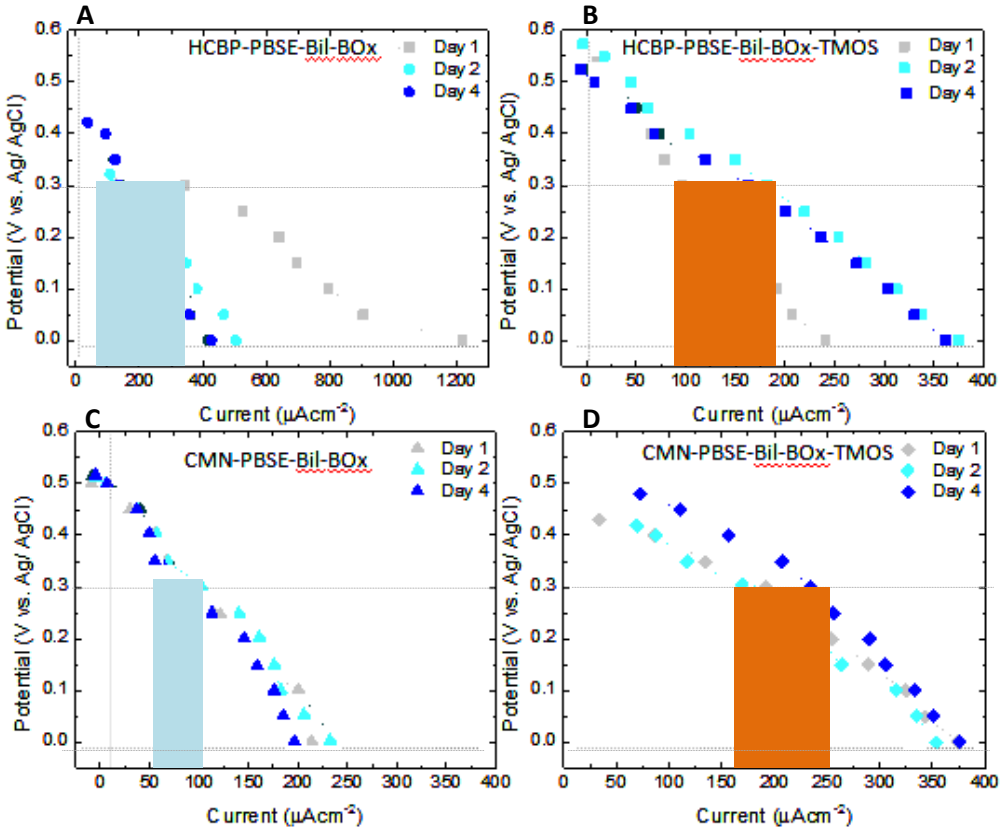

Figure 7.5. Polarization curves of HCBP and CMN-based biocathodes integrating bilirubin as an orienting agent for BOx enzyme and silica-gel formed by CVD. A) and C) Electrodes with no silica-gel on the surface show a decay in current density output, B) and D) biocathodes with silica gel show an increase in current density between the 1st and 4th day of testing (electrodes stored at 4ºC in humid conditions).

From the resulting polarization curves of biocathodes without silica-gel (HCBP-PBSE-Bil-BOx and CMN-PBSE-Bil-BOx) and with silica-gel (HCBP-PBSE-Bil-BOx-TMOS and CMN-PBSE-Bil-BOx-TMOS) in figure 7.5, we observe that for electrodes without silica-gel a

drop of current generation is produced. From day 1 to 4, a drop of current density from ~370 $\mu A.cm^{-2}$ to 120 $\mu A.cm^{-2}$ at 0.3V is observed for HCBP-based cathodes and from ~120 $\mu A.cm^{-2}$ to 65 $\mu A.cm^{-2}$ for CMN-based cathodes (figure 7.5.a and 7.5.c). Contrarily, biocathodes with silica-gel demonstrated an increase in current generation for day 4 compared to day 1, from ~80 $\mu A.cm^{-2}$ to 160 $\mu A.cm^{-2}$ for HCBP-based cathodes, and from ~160 $\mu A.cm^{-2}$ to 240 $\mu A.cm^{-2}$ for CMN-based biocathodes (figure 7.5.b and 7.5.d). This phenomenon may be related to the gellation process of silica gels, which was demonstrated to have higher kinetics at a low pH. As a consequence, the gellation of the hydrogel at pH 7.5 is slow and may take several days as shown by the polarization curves of CMN-PBSE-Bil-BOx-TMOS and CMN-PBSE-Bil-BOx-TMOS. Additionally, the cathodes made with HCBP show the highest and more reproducible OCP. From these results, the HCBP bucky paper was selected to continue the studies.

7.3.4. Performance of Biocathodes Encapsulated in Polymer

In order to successfully integrate EFCs to biomedical devices for extracorporeal applications, the EFCs must be assembled within biocompatible and bioinert materials. From those materials, as explained above, PDMS was chosen to conduct this research due to its widely proven biocompatible and bioinert properties. Moreover, EFCs integrated into PDMS, polymeric matrix utilized in the fabrication of contact lenses, could potentially be utilized to power drug delivery systems, biosensors and supervision enhancement devices that use contact lenses as a platform. Aiming to achieve the fabrication of a biocathode that allow the passive air-flow to the catalytic layer, PDMS was studied for the assembly of HCBP-based biocathodes, the subject of study in this section of our research.

HCBP-biocathodes were developed as described in the respective section above and assembled to a 2D-microfluidic system under passive air-flow conditions for electrochemical characterization. After the incorporation of the electrodes within the polymeric matrix of PDMS, the HCBP-based cathode utilizing bilirubin (not shown) demonstrated lower current density generation than cathodes that did not employ this substrate (Figure 7.6). Mass transfer limitations had a higher influence in biocathodes with only BOx, which demonstrate the rate of consumption of oxygen on the catalytic layer was faster than the rate of oxygen diffusion, decreasing the slope of the curve (blue curves in figure 7.6). The catalytic layer of cathodes utilizing only BOx on the surface had enhanced current density output at potentials ≥ 0.4 V (in region of the polarization curve where kinetic losses govern). These results show the increased kinetic activity of the catalytic layer for electrodes integrating BOx without silica-gel (PDMS-HCBP-BOx-PDMS). However, between the 1st and 2nd day of operation, the electrodes decreased the current generation by about 100µA.cm^{-2} at 0.3V.

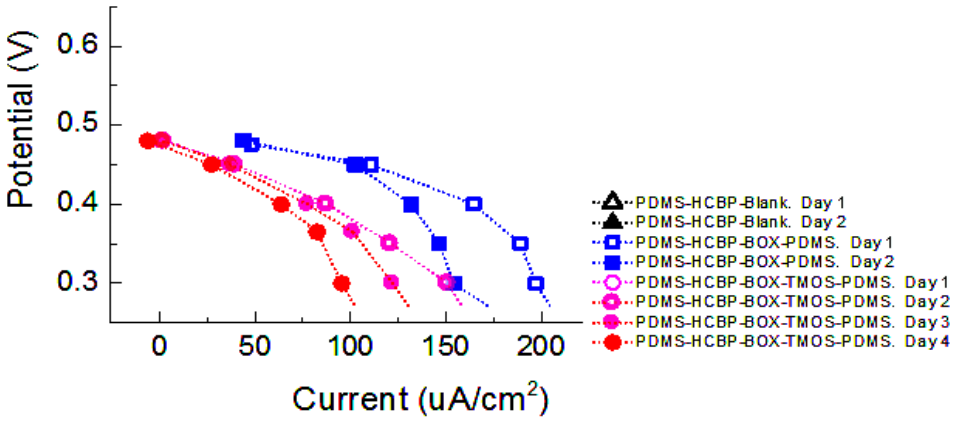

Figure 7.6. Polarization curves of HCBP-based biocathodes showing between 0.5 and 0.3V (left). Electrodes that did not utilize silica-gel (blue curves) and electrodes that utilized silica-gel (pink curves) as an entrapment matrix for the BOx enzyme for oxygen reduction were evaluated in a fan-shape gas-diffusional, half-cell configuration. Tests performed during 4 days of continuous operation demonstrate the biocathode integrating CVD of TMOS as enzyme entrapment procedure effectively stabilizes the active structure of the enzyme on the electrode, inset (right).

In the region of the polarization curve governed by resistivity losses (≥0.2V and ≤ 0.4V) , the biocathodes containing the silica-gel showed the lower performance up to the 2nd day of test. By the 3rd day of testing, the stability of the catalytic layer of PDMS-HCBP-BOx-PDMS significantly dropped to OCP < 0.3V (not shown) when compared to PDMS-HCBP-BOx-TMOS-PDMS (pink curves in figure 7.6). This drop in performance may be due to the loss in activity of the BOx enzyme in the PDMS matrix and/or due to the release of enzyme of BOx from the catalytic layer. On the other hand, biocathodes with silica-gel tested between day 1 and day 4 gave a smaller decrease of current generated of ~ 50 $\mu A.cm^{-2}$ at 0.3V (pink curve, figure 7.6). These results corroborate that the silica-gel matrix stabilizes the active catalytic layer on the biocathode which helps to maintain favorable interaction at the three phase interface.

7.5. Conclusion

This research explored the development of reagentless bioanode designs and passive air-flow in biocathodes integrated within a biocompatible PDMS matrix. The bioanode composed by CMN-grade "bucky" paper and GDH with its tethered NAD^+/NADH- cofactor was shown to work under physiological and reagentless conditions within the two days studied. For the biocathode, the participation of two "bucky" papers, the entrapment BOx in silica-gel by CVD of TMOS, and the use of bilirubin as an orienting agent for the enzyme was studied. In the end, the simplest HCBP-BOx design was selected to be introduced into the PDMS matrix for performance evaluation. The electrochemical performance of the bioelectrode designs were analyzed utilizing a paper-based microfluidic system. The designs can be further improved for increased ET, and subject to long-term stability for continuous operation and storage stability

studies. The resulting technology could be assembled into full cells and transferred to contact lens enzymatic fuel cell (CL-EFC) and other EFC designs for BMD applications.

Utilizing a reagentless bioanode that integrates nicotinamide adenine dinucleotide (NAD^+/NADH)-dependent glucose dehygrogenase (GDH), its tethered cofactor (NAD^+/NADH), and multiwalled carbon nanotubes (MWNTs)-based bucky papers could satisfy the demand of current generation of a micro or nano BMD.

Chapter 8. Outlook

Interdisciplinary research has combined the efforts of many scientists and engineers to gain an understanding of biotic and abiotic electrochemical processes, materials properties, biomedical, and engineering approaches for the development of alternative power-generating and/or energy-harvesting devices, aiming to solve health-related issues and to improve the quality of human life.[24] In the present research, the design of bioelectrodes introduced were envisioned for biomedical applications destined to power nano- and microelectronic medical devices, drug delivery systems and biosensors for extracorporeal and implantable applications.

8.1. Limitations of noble metal catalysts

Some studies suggested the use of noble metal catalyst for glucose oxidation in FC designs. However, the use of those catalysts are a major concern due to toxicity and the low power density generation within physiological conditions.[190] Platinum catalyst, for example, is deactivated by the formation of a film of platinum oxide. This reaction is coupled to the oxidation of glucose in presence of oxygen. [191] After deactivation, the glucose oxidation is no longer achieved.

Among many different types of FCs, BFCs are promising devices for *in vivo* applications.[154, 155, 190, 192] BFCs can operate under physiological conditions (neutral pH, temperatures between 25–50ºC, atmospheric pressure, etc.), converting naturally present substrates into products that are tolerable to the host. In order to design practical applicable BFCs for powering or for use as a medical device, several technologies must be investigated and developed.

8.2 Possible Applications

When considering the different applications for BFC designs, we must evaluate the environmental and physiological characteristics unique to each application. These BFCs can be assembled to BMDs to cover different needs including:

1) Micro- and nanoelectrodes to transfer a signal between nerves and muscles.

2) Implanted and extracorporeal sensors to monitor various parameters in the body.

3) Power sources for implants.

4) Data communication devices between implanted BMDs and a unit located externally.

5) Sensing systems to provide trigger mechanisms for other implants and drug-delivery systems.

6) Contact lens supervision devices and so forth.

Some medical products that could potentially benefit from the incorporation of EFCs are: cochlear and retina implants, functional electrical stimulation, intracranial pressure sensor implants, glaucoma and sphincter sensors, artificial sphincters, and drug-delivery systems in patch designs and contact lenses. Each of these applications imposes different demands on the BMD. For example, brain fluid has different characteristics (fuel concentration, pH, temperature, free O_2 content, etc.) compared to blood, saliva, tears, urine, and other physiological fluids. The enzymes chosen for a specific application must be determined by the biofuel and bio-oxidant available in the host organism, which then is combined with a suitable electrode material.[24]

8.3. Precedents of Implanted BFCs

In the 1960s, feasibility studies of a glucose/oxygen FC to power pacemakers and parametric studies on glucose anode for implantable applications were performed.[29, 193] In this area, the Artificial Heart Program of the United States National Heart, Lung and Blood Institute made the most significant contributions.[194] The conversion of glucose to gluconolactone with a

two-electron transfer process was demonstrated to be marginally feasible to power a prosthetic heart.[29] The extraction of O_2 required to power a 12.5 W implantable FC was found to be dependent on the diffusion coefficient of the bio-oxidant in blood.[193] Furthermore, the process was considered to be marginally feasible for implantable applications.[29] Later, lithium-battery technology was adopted and optimized to fulfill the energy demand for implanted pacemakers as an example.

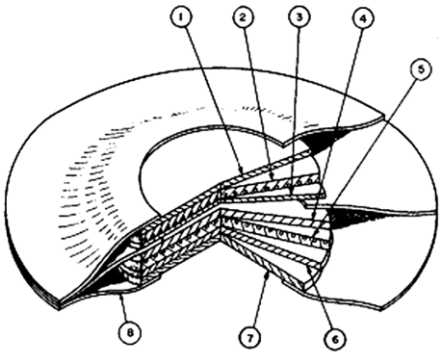

Figure 8.1. Schematic representation of the FC implanted and tested in a dog as early as in the late 60s. (*Image source : Drake et al Trans. Am. Soc. Artif. Intern. Organs 1970, 16, 199 –205*).

Currently, lithium batteries are the dominating technology to power medical devices and more specifically in implantable applications such as pacemakers. For this biomedical application, the battery technology has, however, a major drawback which is the need for replacement of the power source after 5 to 8 years of use. Replacing the battery involves surgical procedures that represent health risks and high costs. Complication in the replacement of pacemakers was present in 4% of a study group where 1,031 patients were involved. For replacement of cardioverter-defibrillator, complications related to battery replacement were present for 15.3% of the patients of a group of 713 individuals.[195] Although the complications

may not be strictly linked to the battery performance, the patients that needed battery replacement and had to undergo a second surgery showed the highest proclivity to complications when compared to patients that were implanted for the first time. Therefore a power source device for BMDs would have to overcome the limiting life-stability.

BFC technologies would have to comply with manufacturing criteria held for batteries utilized for implantable or other BM applications, and overcome life-time limitations. Implantable BFCs must meet the batteries' reliability criteria, such as having: 1) a continuous power supply, 2) low self-discharging time, 3) high reliability and efficiency, 4) biocompatibility, 5) miniature size, 6) light weight and 7) operation under physiological conditions.[194] Furthermore, EFCs need to be designed to achieve long-term stability in physiological conditions in order to satisfy energy demands of implantable medical devices to last the post-surgery life of the host individual. The long-term stability of BFCs are theoretically achievable, BFCs could operate over prolonged periods of time with no need to receive an external supply of biofuel since the substrates that fuel the system are present in the host organism. In recent years, several studies were performed looking to achieve this goal and harvest energy from several living organism.[50, 87, 192, 196] The concepts employed in these systems could later be transferred to implants in mammals and humans.

8.4. In vitro and In vivo Studies

Both *in vitro* and *in vivo* studies, showed the feasibility of the implantable power device to work utilizing glucose, which is naturally present in the blood. After the introduction of glucose and the oxidation of other carbohydrates for power generation by Bockris *et al*.,[197], Wolfson *et al*. proposed the idea of fueling catalytically active electrodes by carbohydrates and O_2 occurring in interstitial fluids.[198, 199] Together with his coworkers, Talaat demonstrated the

current output generation from electrodes immersed in the blood stream,[200] 6 months *in vitro* and 30 days in animal testing of their prototypes.[194] During animal testing, 6.4 $mWcm^{-2}$ maximum power output for a short period of time and 2.2 $mWcm^{-2}$ of power density for continuous operation were reported. Drake et al. introduced a design, utilizing a dialysis membrane to limit the flow of high-molecular-weight compounds to the BFC, an external biocompatible coating of the device to avoid unfavorable immunological responses by the host organism, and isolation of the cathode by O_2 and carbon dioxide phase separation within the BFC (Figure 1).[194] Recent advances showed the implantation of FCs in mammals, giving 161μWml^{-1} for a period of 9 days (figure 8.2). [190]

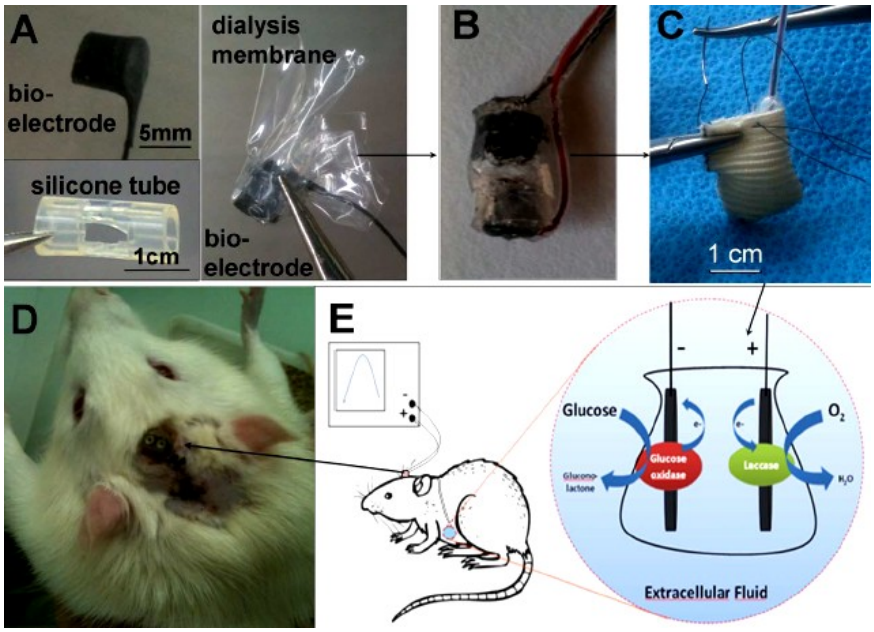

Figure 8.2 From bioelectrodes to a biocompatible biofuel cell implanted in the abdominal cavity of a rat. From A to D, sequence of cell assembly and implantation, E) schematic of cell location of an implant within the rat and bioelectrodes schematic. (*Zebda et al Scientific Reports 2013, 3, 1-5*).

In order for the biodevice to function, an electrical connection between the biocatalyst (redox enzyme) and the electrode surface needs to be achieved. Furthermore, systems for mass transport of a substrate from the body fluid to the electrodes, as well as size and shape of the

BFC, need to be considered based on the requirements of the intended BMDs, intravascular, extravascular, transcutaneous, and so forth.

For the successful design of glucose/oxygen FC, biocompatibility issues need to be addressed. For example, a problem with using GOx in implantable conditions is the fact that O_2 is the natural electron acceptor, and the enzyme produces hydrogen peroxide (H_2O_2) in the presence of O_2, which is toxic, and hence requires additional modifications of the biodevices for their operation *in vivo*. In addition to the undesired biocompatibility issues, hydrogen peroxide can be both reduced and oxidized, and thus can create parasitic (crossover) currents, particularly in the long-term, continuous operation of a biodevice. As stated in this research, to avoid the influence of O_2 on bioanodes, NADH-dependent glucose dehydrogenase (GDH) is used and reagentless bioanode designs were introduced (chapter 4 and 7) in order to overcome mass transfer and design limitations.

The early developed implantable abiotic FCs, researched in the 1970s and implanted in rats, sheep and dogs, [194, 201, 202] were all rather bulky devices. A restriction in the reduced size is also true even for modern batteries, all needing a casing to contain the electrolyte, which therefore excludes their use in truly miniature applications. One of the salient characteristics of EFCs is the capability for miniaturization, which was shown feasible by Adam Heller who demonstrated that an EFC can be made significantly smaller than batteries and other types of FCs (figure 8.3).

Figure 8.3. Experimental setup of a GOx/BOx microscale EFC implanted into a grape, the two electrodes are drawn with lines to highlight their positions (*N. Mano et J. Am. Chem. Soc. 2003, 125, 6588 –6594*)

Due to the high specificity of enzyme catalysts, no separator membranes are generally needed. By employing either mediators immobilized on the electrode surface or a DET-based approach and by having the enzymes immobilized on the electrodes, truly miniature devices for implantation can be created by excluding all membranes and compartments.[24] Several miniature BFCs reported in literature, were operated under both physiological conditions *in vitro*, as well as *in vivo*. However, a membrane is needed when an O_2-sensitive enzyme is used and when soluble species are utilized in the BFC construction.

8.5. Biocompatibility Criteria

First, *in vivo* conditions can be quite harsh, especially in vertebrates. Biocompatibility is a major issue for long-term implantation. Operation *in vivo* compared to *in vitro* poses many additional difficulties. These organisms have an aggressive immune system in which implanted BFCs will be subjected to a multitude of proteins and cells present in the blood that will interact with the implant.[116] An implant placed into a blood vessel or a tissue will be recognized by the body as a foreign element, which can trigger inflammation reactions. Also, physiological fluids are complex liquids containing a multitude of low-molecular-weight compounds, which can affect the performance of the BFC. For extracorporeal applications, the inflammatory and allergic reactions of the external tissue may appear as an immunological response of the host. In order to avoid these issues, the materials used in the BFC designs should be bio-inert and biocompatible to avoid triggering the host's immune system.

Second, the amount of sugar and O_2 available in the living organism is limited. Free O_2 is significantly lower inside organisms when compared to air-saturated solutions *in vitro*. The sugar of choice for many implantable applications is glucose, with about 5 mM being present in

humans.[189, 203] The problem with a limited amount of fuel available for the bioanode can be mitigated by designing bioanodes with better fuel efficiency. Glucose/O_2 EFCs use is inefficient since these use only 2 of 24 electrons from the glucose substrate. Consequentially, enzyme cascades should be developed in order to fully oxidize the biofuel; work currently in development by Minteer's group.[12, 19, 20] Immobilization of the enzymatic systems that oxidize the same substrate would improve the efficiency of the bioelectrodes. Gorton and his coworkers recently demonstrated a more efficient glucose bioanode, where, by means of co-immobilization of different glucose-oxidizing enzymes, 6 electrons per molecule of glucose could be harvested, significantly increasing the current density and Coulombic efficiency of the bioanode.[204] The approach of using multiple enzymes and enzyme cascades is powerful but it has yet to be demonstrated in any *in vivo* application.

8.6. Considering the Microfluidic Systems

Air-breathing devices can in theory be made very powerful (up to 100 $mAcm^{-2}$), where the porosity, thickness, hydrophobicity, and ionic conductivity of the liquid phase are all important factors, which should be taken into consideration when the biodevice is designed.[99] However, the limited amount of fuel and oxidant, as well as slow diffusion of these compounds in the tissue, can be resolved for some applications by shifting the implant site from the physiological or extravascular tissue to an intravascular implant. However, good biocompatibility is of utmost importance, since blood coagulation can lead to thrombosis in the host organism with lethal consequences in the worst case scenario. The rather low stability of enzymes and deactivation in the presence of different compounds available in physiological fluids are significant hurdles for the practical realization of implanted EFCs. When considering BMDs requiring surgery, long-term stability is required for the viability of the biodevice.

However, by utilizing different rational immobilization strategies, enhanced stability and efficiency of the created biodevices can be obtained. This is the case for silica-gel, nafion, and chitosan among others.[45, 140, 142, 151, 179]

8.7. Conclusion

During *in vitro* and *in vivo* biofuel-cell studies over the past decades, researchers have focused on: identifying different biocatalytic species and their mediators and cofactors; isolating redox enzymes; understanding their mechanism of action; stabilizing biocatalysts *ex vivo*; and developing new materials as well as feasible electrode designs. Besides investigations *in vitro*, designs also need to be evaluated *in vivo* in order to validate the biocompatibility of materials and the performance of the devices. Evaluation of BFCs, the materials from which they are constructed, and the products of bioelectrocatalytic reactions have to satisfy safety standards (chemical and mechanical stability and biocompatibility) and output energy requirements by controlled energy-release systems, according to their application.

Chapter 9. Conclusion

The focus of this research is the development of bioelectrodes with controlled chemistry designed to enhance electron transfer and to stabilize the biocatalytic systems that can be feasible used in EFCs. These electrodes, assembled into EFCs, are envisioned to power biomedical devices for extracorporeal and implantable applications.

9.1. Enhanced enzyme stability and decrease of limitations of the bioanodic systems – The development of a reagentless NAD^+/NADH-dependent GDH-based anode

This research developed a reagentless NAD^+/NADH-dependent enzymatic system. In chapter 3 and 4, the CNTs/ chitosan matrix is utilized to entrap and stabilize the 3D-active enzymatic system. When comparing the enzymatic systems on the same BEP-"bucky" paper, the GDH has shown the best performance against ADH and LDH, dehydrogenases with similar enzyme unit activity with their respective fuels. These results show the kinetic, ohmic and mass transport limitations inherent in the GDH-based anode have been minimized allowing high current outputs. These nanostructured bioanodes can be assembled to quasi-2D capillary driven flow systems for real fuel cell applications.[119, 121]

Michaelis-Menten analysis shows the enzymatic system with the cofactor in solution has an I_{Max}= 3.4 ±0.2mA.cm-^{2} and K_{Mapp}=17.5±3.1mM for GDH-based anodes, integrating, BEP-grade bucky papers at 25ºC. For bioanodes using CMN-based papers, I_{Max}=2.5±0.8 mA.cm^{-2} and K_{Mapp} =13.6 ± 1.8 mM at 25ºC and I_{Max}=3.2±1.3 mA at 4ºC. CMN-grade paper shows an increase in current generation, when evaluated in similar conditions than that of the BEP-grade paper. These results allow us to speculate that the nanostructural architecture of the CMN-

material helps to enhance ET and to stabilize the 3D-active structure of GDH in the 3D-CNTs/chitosan matrix.

Next, the use of a paper-based quasi-2D microfluidic system improved the biofuel feeding process with non-external energy supply due to a capillary driven flow maintained by liquid-vapor equilibrium. The integration of such a system to the half-cell, anode, was successfully achieved. This assembly presents an OCP of -0.225V and -0.275V for BEP and CMN-based anodes, respectively, and displays 200 $\mu A.cm^{-2}$ and 1.1 $mA.cm^{-2}$ at -0.15 V for BEP- and CMN, respectively. This bioanode satisfactorily exceeds the performance of recent MWNTs-based designs.[167]

Further studies on NAD^+/NADH cofactor tethering on the electrode surface of CMN-bucky paper were feasible. Data shows that the bioelectrodes are capable of performing under continuous operation for ~16 hours (chapter 5). The NAD^+-cofactor was tethered to the surface of the MWNTs-wall by employing a linker capable of interacting on the CNT-wall by π-π stacking interaction. The reagentless and non-reagentless NAD^+- dependent GDH-based bioanode integrating CMN-bucky paper presented in this research has been demonstrated to be reproducible and feasible to be used in half-electrolytic and paper-based fan cells. To the author's knowledge, the bioanodes introduced in this research have shown the best performance among previous NAD^+-dependent GDH-based bioanodes and other enzymatic systems used for glucose oxidation.

9.2. Enhanced biocathodic enzyme stability and mitigation of system limitations

In this study, we aimed to enhance the catalytic activity of BOx enzyme on the surface of carbon nanostructured electrodes. Immobilization techniques were applied to allow the preservation of the active 3D-structure of the enzyme for prolonged periods of time in storage at 4ºC, in humid conditions. The first approach was to tailor the nanoarchitecture of the electrode material; CNTs were grown on Toray paper utilized on the catalytic layer of gas-diffusional cathode designs. Catalytic behavior of the enzyme with respect to pH (5.5 to 8) and time were performed. The CNT growth increased the available surface area allowing increased enzyme loading and enzyme entrapment with enhanced stability. As the pH was increased from 5 to 8, performance varied due to conformational changes induced by the environment surrounding the enzymatic structure. Maximum current output was observed at pH 5.5 while the most consistent and reproducible current density was obtained at pH 7.5. At this pH, the cathode performed satisfactorily giving a current density of 205.37 ± 1.47 $\mu A.cm^{-2}$, at potential of 0.3 V. This biocathode design is suitable for extracorporeal biomedical applications. This enzymatic system achieved stability within the 3D CNTs-network/silica-gel matrix for 6 months (chapter 5) of test.

The second approach involved the use of commercially-available "bucky" papers and stabilization procedures aimed to increase enzyme life-time and performance of the biocathode. This research developed a biological catalytic layer for Oxygen reduction reaction (ORR) that maintained 65% of its initial performance for 150 days and ~50% of its performance within 360 days of evaluation (chapter 6). A 3D-CNTs network and the silica-gel matrix were used to tailor the catalytic layer for enhanced structural stability of the enzyme and ET.

9.3. Integration of the bio-electrodes into a biocompatible polymeric matrix

This research investigated the integration of GDH and BOx-based bioelectrodes in biocompatible polymers for potential biomedical applications. Herein, we explored the development of reagentless bioanode designs and gas-diffusion biocathodes integrated in a biocompatible PDMS matrix. At the anode, CMN-grade "bucky" paper was utilized to develop a reagentless NAD^+/NADH-dependent GDH-based bioanode. The bioanode was shown to work under physiological and reagentless conditions within a two-day study (chapter 7).

For the biocathode, two grades of "bucky" papers were investigated for the best performance for systems that involved 1) BOx entrapped in silica-gel, 2) use of bilirubin as orienting agent for the enzyme, 3) enzyme tether agent, and 4) CNTs additional integration to the catalytic layer (chapters 7 and 6). The final experiments introduced the simplest HCBP-BOx design into the PDMS matrix for performance evaluation, assembled to a 2D-paper based microfluidic system. The designs can be further improved for increased ET, for increased long-term stability during continuous operation and storage conditions, and to meet regulations pertaining biocompatibility and cito-toxicity for *in-vivo* applications. The technology developed in this research could be assembled into full cells and transferred to designs for BMD applications.

Although this manuscript did not describe full EFC systems, the bioelectrode designs shown were successfully assembled in full cells and the respective information is available in literature. An example of these full cells is reported by Narváez Villarrubia et al[119], where the generated current is utilized to power a digital clock and the cell was demonstrated capable of working during continuous operation for a 16-day time frame (figure 9.1). We are confident that

utilizing the bioelectrode designs presented herein can satisfy the demand of power generation of a micro-or nano biomedical device.

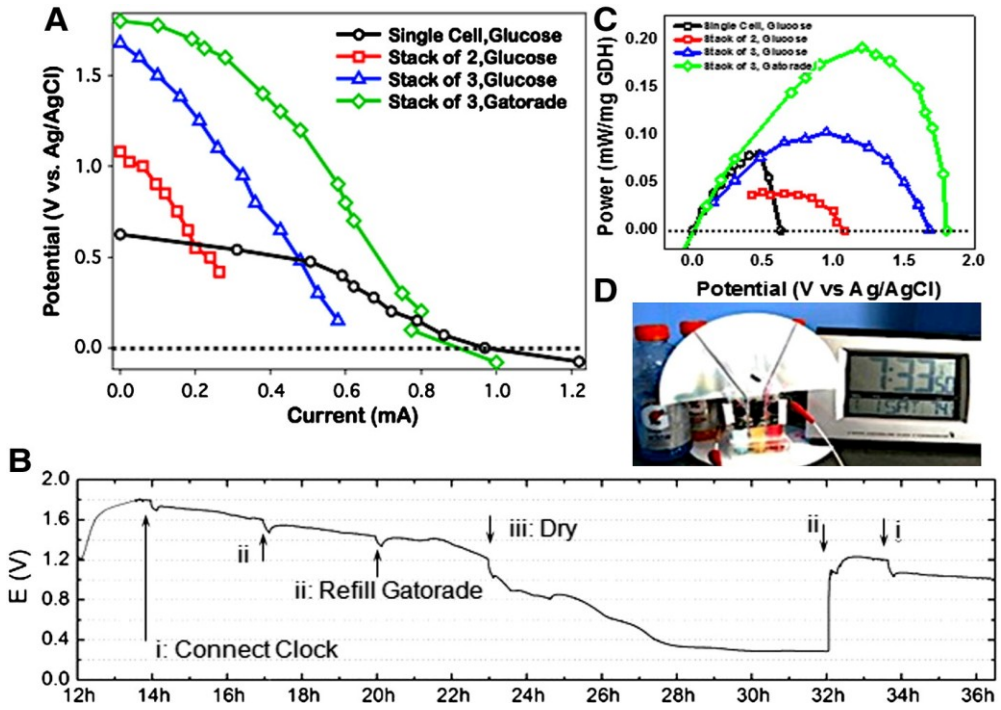

Figure 9.1. A) Polarization curves of a single cell, 2-cells, and 3-cells stack in series using 0.1M glucose in 0.1M PB, 50mM NAD+, 0.1 M KCl, pH 7. The green curves show a 3-leg stack cell in Gatorade (pH 7, 50mMNAD+); B) Corresponding power curves (similar legend); C) Time based test of a 3-leg stack in (i) glucose solution with applied load of 300mA and (ii) the connected digital clock in Gatorade; (D) Picture of 3-cells in series on a single piece of paper with Gatorade (pH 7, 50mMNAD+) powering a digital clock. (For interpretation of the references to color in this figure legend, the reader is referred to the web version of this article (*Image source: Narváez Villarrubia et al Electrochem.Comm. 2014, 45, 44-47*).

Future Outlook

The work presented in this document could serve as the foundation for the development of carbon nanocomposite-based bioanodes and biocathodes integrating GDH and BOx enzymatic systems, respectively, with the potential for biomedical applications. This research focused on:

1) Developing new nanoarchitectural structures and exploring carbon nanocomposite materials.
2) Identifying different scenarios for optimum biocatalytic performance of BOx and GDH enzymes.

3) The use of a tether agent to orient the active site of BOx and to immobilize the NAD^+/NADH cofactor.
4) Stabilizing the enzymes on the catalytic layer of the electrodes using chitosan and silica gel matrices.
5) Analyzing the use of 2D-paper based microfluidic system.
6) Analyzing the integration of bioelectrodes into a PDMS matrix.

Although this research successfully improved the current generation of the GDH and BOX systems, improved the stability of said systems on their respective catalytic layers, and integrated a microfluidic system that feeds the fuel cell without administration of external energy, opportunities were identified for improvements to the systems presented herein: designs must be improved to optimize ET, and long-term stability of the enzymatic systems must be achieved to satisfy requirements for implantable BMDs. Additionally, after improving stability, the bioelectrodes must be evaluated for biocompatibility of the materials.

References

1. S. Calabrese Barton, J. Gallaway, P. Atanassov, *Chemical Reviews* **2004,** *104*, 4867-4886.
2. P. Atanassov, C. Apblett , S. Banta, S. Brozik, S.C. Barton, M. J. Cooney, B.Y. Liaw, S. Mukerjee, S. Minteer, *Electrochemical Society Interface* **2007,** *16*, 28-31.
3. S. D. Minteer, P. Aatanassov, H.R. Luckarift, G.R. Johnson, *Mater. Today* **2012,** *15* (4), 166-173.
4. S.D. Minteer, B.Y. Liaw, M. J. Cooney, *Current Opinions in Biotechnology* **2007,** *18*, 228 - 234. .
5. I. Willner, Y.-M. Yan, B. Willner, R. Tel-Vered, *Fuel Cells* **2009,** *9* (1), 7-24.
6. G.T.R. Palmore, G.M. Whitesides, *ACS Symp. Ser.* **1994,** *566*, 271-290.
7. K. Nishio, A. Kouzuma, S. Kato, K. Watanabe, *Microbial Biofilm* **2012**, 175-191.
8. Y. Han, C. Yu, H. Liu, *Biosensors and Bioelectronics* **2010,** *25*, 2156-2160.
9. G.A. Justin, Y. Zhang, T. Cui, C. Bradberry, M. Sun, R. Sclabassi, *Journal of Biological Engineering* **2011,** *5* (5), 2-10.
10. M. Sun, G. A. Justin, P. A. Roche, J. Zhao, B. L. Wessel, Y. Zhang, R. L. Scalabassi, *IEEE Engineering in Medicine and Biology Magazine* **2006**.
11. D. Bhatnagar, S. Xu, C. Fischer, R. L. Arechederra, S. D. Minteer, *Physical Chemistry Chemical Physics* **2011,** *13*, 86-92.
12. R. Arechederra, S. D. Minteer., *Electrochimica Acta* **2008,** *53*, 6698-6703.
13. A. Zebda, C. Gondran, A. le Goff, M. Holzinger, P. Cinquin, S. Cosnier, *Nat. Commun.* **2011,** *2*, 1-6.
14. S. Calabrese Barton, J. Gallaway, P. Atanassov, *Chemical Reviews* **2004,** *104*, 4867-4886.
15. Heller, A., *Physical Chemistry Chemical Physics* **2004,** *6*, 209-216.
16. A.M. Kannan, V. Renugopalakrishnan, S. Filipek, P. Li, G.F. Audette, L. Munukutla, *Journal of Nanoscience and Nanotechnology* **2009,** *9* (3), 1665-78.
17. J. A. Cracknell, K. A. Vincent, F. A. Armstrong, *Chem. Rev.* **2008,** *108*, 2439-2461.
18. C. Wang, M. H. Nehrir, S. R. Shaw, *IEEE Transactions Energy Conversion* **2005,** *20*, 442-451.
19. D. Sokic-Lazic, S. D. Minteer, *Electrochemical and Solid-State Letters* **2009,** *12* (9), F26-F28.

20. D. Sokic-Lazic, S. D. Minteer, *Biosensensors and Bioelectronics* **2008,** *24*, 939-944.
21. G. N. Waite, L. R. Waite, *Applied Cell and Molecular Biology for Engineers* **2007**.
22. H. R. Luckarift, P. Atanassov, G. R. Joohnson, *Enzymatic Fuel Cells: From Fundamentas to Applications*. John Wiley and Sons, Inc: Hoboken, New Jersey, 2014.
23. M. J. Moehlenbrock , R. L. Arechederra, K. H. Sjöholm and S. D. Minteer, *Anal. Chem.* **2009** *81* (23), 9538-9545.
24. M. Falk, C. W. Narváez Villarrubia, S. Babanova, P. Atanassov, S. Shleev, *Chemphyschem* **2013**.
25. F. Stetten, S. Kerzenmache, R. Sumbharaju, R. Zengerle, J. Ducrée, *Proc. Eurosensors* **2006,** *XX*, 222-225.
26. S. Kerzenmacher, J. Ducreé, R. Zengerle, F. von Stetten, *Journal of Power Sources* **2008,** *182*, 1-17.
27. K. Habermuller, M. Mosback, W. Schuhmann, *Electron-transfer mechanisms in amperometric biosensors* **2000,** *366*, 560-568.
28. E. Katz, A. N. Shipway, I. Willner, *Encyclopedia of Electrochemistry* **2002,** *9*, Chap.17, 559-626.
29. A. J. Appleby, D. Y. C. N.G, H. Weinstein, *Journal of Applied Electrochemistry* **1971,** *1*, 79-90.
30. Heller, A., *J.Phys. Chem.* **1992,** *96*, 3579-3587.
31. Heller, A., *Curr. Opin. Chem. Biol.* **2006,** *10*, 664-672.
32. W. Schuhmann, T. J. Ohara, H. L. Schmidt, A. Heller, *J. Am. Chem. Soc.* **1991,** *113*, 1394-1397.
33. A. Heller, B. J. Feldman, J. Say, M. S. Vreeke, M. F. Tomasco, *In Small Volume in Vitro Analyte Sensor, 1998-US2652 (E. Heller & Company, USA),* **1998**, 83.
34. Z. Gao, G. Binyamin, H. H. Kim, S. C. Barton, Y. Zhang, A. Heller, *Angew. Chem. Int. Ed. Engl.* **2002,** *41* (5), 810-813.
35. F. Mao, N. Mano, A. Heller, *Journal of the American Chemical Society* **2003,** *125*, 4951-4957.

36. A. Heller, Z. Gao, M. Dequaire, *in Electrodepostition of Redox Polymers and Co-Electrodeposition of Enzymes by Coordinative Crosslinking, 2002-US30105 (Therasense, Inc. USA)* **2003**, 65.
37. T. Chen, S. C. Barton, G. Binyamin, Z. Gao, Y. Zhang, H. H. KIm, A. Heller, *J. Am. Chem. Soc.* **2001,** *123*, 8630-8631.
38. Z. Liu, B. J. Feldman, F. Mao, A. Heller, *In Redox Polymers for Use in Analyte Monitoring, 2008-51835 (Abbott Diabetes Care Inc., USA)* **2012**, 34.
39. Heller, A., *in Fabrication and Use of Biological Fuel Cell, 1998-203227 (Therasense, Inc., USA)* **2001**, 10.
40. M. Falk, Z. Blum, S. Shleev, *Electrochim. Acta* **2012,** *82*, 191-202.
41. A. Ramanavicius, A. Ramanaviciene, *Fuel Cells* **2009,** *9*, 25-36.
42. E. H. Yu and K. Scott, *Energies* **2010,** *3*, 23.
43. M. R. Tarasevich, V. A. Bogdanovskaya, N. M. Zagudaeva, and A. V. Kapustin, *Russian Journal of Electrochemistry* **2002,** *38* (3), 335.
44. A. Guiseppi-Elie, C. Lei, R.H. Baughman, *Nanotechnology* **2002,** *13*, 559- 64.
45. A. Ghanem and A. Ghaly, *Journal of Applied Polymer Science* **2003,** *91* (2), 861-866.
46. D. Ivnitski, B. Branch, P. Atanassov, C. Apblett, *Electrochemistry Communications* **2006,** *8*, 1204-1210.
47. Z. Zhu, C. Momeu, M. Zakhartsev , U. Schwaneberg, *Biosen. and Bioelec.* **2006,** *21* (11), 2046-2051.
48. D. Ivnitski, K. Artyushkova, R.A. Rincón, H.R. Luckarift, G.R. Johnson, *Small* **2008,** *4*, 357-364.
49. C.-H. Kuo, W.-H. Huang, C.-K. Lee, Y.-C. Liu, C.-M. J. Chang, H. Yang , C.-J. Shieh *Int. J. Electrochem. Sci.* **2013,** *8*, 9242 - 9255.
50. P. Cinquin, C. Gondran, F. Giroud, S. Mazabrard, A. Pellissier, F. Boucher, J.-P. Alcaraz, K. Gorgy, F. Lenouvel, S. Mathe´ , P. Porcu, S. Cosnier, *Plos One* **2010,** *5* (5), 1-7.
51. C. Tanne, G. Gobel, F. Lisdat *Biosensors and Bioelectronics* **2010,** *26* (2), 530-535.
52. V. Scherbahn, M. T. Putze, B. Dietzel, T. Heinlein, J. J. Schneider, F. Lisdat, *Biosens Bioelectron.* **2014,** *61*, 631-638.

53. F. Tasca , L. Gorton, W. Harreither, D. Haltrich, R. Ludwig, G. No¨ll, *Journal of Physical Chemistry C* **2008,** *112* (35), 13668-13673.
54. R. Ludwig, W. Harreither, F. Tasca, L. Gorton, *Chemical Physics and Physical Chemistry* **2010,** *11*, 2674-2697.
55. F. Tasca, W. Harreither, R Ludwig, J. Justin Gooding, L. Gorton, *Analytical Chemistry* **2011,** *83*, 3042-3049.
56. S. Ferri, K. Kojima, K. Sode, *J. Diabetes Sci. Technology* **2011,** *5* (5), 1068-76.
57. I.Katakis, E. Dominguez, *Microchimica Acta* **1997,** *126* (1-2), 11-32.
58. V. Svoboda, C. Rippolz, M. J. Cooney, B. Y. Liaw, *The Journal of Electrochemical Society* **2007,** *154* (3), D113 - D116.
59. D. Zhou, H.-Q. Fang, H-Y. Chen, H.D. Zhou, H-Q. Fang, H-Y. Chen, H-X. Ju, Y. Wang, *Analytica Chimica Acta* **1996,** *329* (1-2), 41-48.
60. A.A. Karyakin, E. E. Karyakin, H. L. Schimidt *Electroanalysis* **1999,** *11* (3), 149-155.
61. A.A. Karyakin, E. E. Karyakin, W. Schuhmann, H. L.Schmidt, *Electroanalysis* **1999,** *11* (8), 553-557.
62. W.J. Blaedel, R. G. Haas, *Anal.Chem.* **1970,** *42* (8), 918-927.
63. P. Leduc, D. Thévenot, *Bioelectrochem. Bioenerg.* **1974,** *1*, 96-107.
64. P. Leduc, D. Thévenot and R. Buvet, *Bioelectrochem. and Bioenerg.* **1976,** *3*, 491-508.
65. J. Moiroux and P. J. Elving, *J. Am.Chem. Soc.* **1980,** *102*, 6533-6538.
66. C. O. Schmakel, K. S. V. Santhanam, P.J. Elving, *J. Am.Chem. Soc.* **1975,** *97* (18), 5083-5092.
67. P. J. Elving, W. T. Bersnaham, J. Moiroux, Z. Samec, *Bioelectrochem. and Bioenerg.* **1982,** *9*, 365-378.
68. R. L. Blankespoor, L. L. Miller, *J. Electroanal. Chem.* **1984,** *171*, 231-241.
69. J. Ludvik and J. Volke, *Anal. Chim. Acta* **1988** *209*, 69-78.
70. P. N. Barlet, *Bioenergetics and Biological Electron Transport* John Wiley & Sons: Chichester, 2008.
71. L. Gorton, P. N. Bartlett, NAD(P)-Based Biosensors. In *Bioelectrochemistry: fundamentals,experimental techniques, and applications*, Bartlett, P. N., Ed. John Wiley & Sons, Inc.: West Sussex, 2008.

72. P.N. Bartlett, *Bioenergetics and Biological Electron Transport,* John Wiley & Sons, Inc.: West Sussex, 2008.
73. L. Gorton, *J. Chem. Soc., Faraday Trans., 1* **1986,** *82*, 1245-1258.
74. L. Gorton, P. D. Hale, B. Persson, L.I. Boguslavsky, H. I. Karan, H.S. Lee, T.A. Skotheim, H.L. Lan, Y. Okamoto, *ACS Symp. Ser* **1992,** *487*, 56-83.
75. M. J. Lobo, A. J. Miranda, P. Tuñón, *Electroanal.* **1997,** *9*, 191-202.
76. E. Lorenzo, F. Pariente, L. Hernáandez, F. Tobalina, M, Darder, Q. Wu, M, Maskus, H. D. Abruña, *Biosens. Bioelectron.* **1998,** *13*, 319-332.
77. L. Gorton, E. Dominguez, *Rev. Molec. Biotechnol.* **2002,** *82*, 371-392.
78. Z. H. Dai, F. X. Liu, G. F. Lu, J. C. Bao, *J. Solid State Electrochem.* **2008,** *12* (2), 175-180.
79. D. C. Tse, T. Kawana, *Anal. Chem.* **1978,** *50*, 1315.
80. E. S. Ribeiro, S. S. Rossatto, Y. Gushikem, L. T. Kubota, , *J. Solid State Electrochem.* **2003,** *6*, 665.
81. C. A. Pessoa, Y. Gushiken, L. T. Kubota, L. Gorton, *J. Electroanal. Chem.* **1997,** *431*, 23.
82. R. A. Rincón, C. Lau, Kristen E. Garcia, Plamen Atanassov, *Electrochimica Acta* **2011,** *56*, 2503-2509.
83. R. A. Rincón, K. Artyuskova, M. Mojica, M. N. Germain, S. D. Minteer, P. Atanassov, *Electroanal.* **2010,** *22*, 799-806.
84. C. W. Narváez Villarrubia, R. A. Rincón, V. K. Radhakrishnan, V. Davis, P. Atanassov, *ACS Applied Materials and Interfaces* **2011,** *3* (7), 2402-2409
85. S. Shleev, J. Tkac, A. Christenson, T. Ruzgas, A. I. Yaropolov, J. W. Whittaker, L. Gorton, *Biosensors and Bioelectronics* **2005,** *20*, 2517-2554.
86. V. Pardo-Yissar, E. Katz, I. Willner, A.B. Kotlar, C. Sandersand H. Lill, *Faraday Discussion* **2000,** *116*, 119-134.
87. N. Mano, F. Mao, A. Heller, *Journal of the American Chemical Society* **2003,** *125*, 6588-6594.
88. J. L. Cole, G. O. Tan, E. K. Yang, K. O. Hodson and E. I. Solomon, *J. Am. Chem. Soc.* **1990,** *112* (6), 2243-2249.
89. J.L. Cole, P. A. Clark, E. I. Solomon, *J. Am. Chem. Soc.* **1990,** *112*, 26.

90. D. M. Ivnitski, C. K Khripin, H.R. Luckarift, G.D. M. Ivnitski, C. Khripin, H.R. Luckaift, G.R. Johnson and P. Atanassov *Electrochimica Acta* **2010,** *55* (4), 7385-7393.
91. D. M. Ivnitski, H. R. Luckarift, R. Ramasamy, K. Artyushkova, P. de la Iglesia, C. Khripin, C. Apblet, G. R. Johnson and P. Atanassov, *Preparation Paper-.Am. Chem. Soc. Fuel. Chem.* **2009,** *54*, xx.
92. C. Fernandez-Sanchez, T. Tzanov, G. M. Gubitz, A. Cavaco-Paulo, *Bioelectrochemistry* **2002,** *58* (2), 149-156.
93. R. J. Lopez, S. Babanova, Y. Ulyanova, S. Singhal, P. Atanassov, *Chem. Electro. Chem.* **2014,** *1*, 241 - 248.
94. S. Tsujimura, A. Kuriyama, N. Fujieda, K. Kano, T. Ikeda, *Anal. Biochem.* **2005,** *337* (2), 325-331.
95. A. Christenson, S. Shleev, N. Mano, A. Heller, L. Gorton, *Biochim. Biophys. Acta* **2006,** *1757*, 1634-1641.
96. C. Kang, H. Shing, A. Heller, *Bioelectrochemistry* **2006,** *68* (1), 22-26.
97. H. Shin , C. Kang, A. Heller, *Electroanalysis* **2007,** *19* (6), 638-643.
98. S. Ha, Y. Wee, J. Kim, *Top Catal.* **2012,** *55*, 1181-1200.
99. S.D. Minteer, *Top Catal.* **2012,** *55*, 1157-1161.
100. G. Fei, G.-H. Ma, P. Wang, Z.-G. Su, *Encycl. Ind. Biotechnol.* **2010,** *3*, 2086-2094.
101. R. J. Chen, Y. Zang, D. Wang, H. Dai, *Journal of the American Chemical Society* **2001,** *123* (16), 3838-3839.
102. H. Jaegfeldt, T. Kuwana, G. Johansson, *J. Am. Chem. Soc.* **1983,** *105*, 1805-1814.
103. M. Falk, V. Andoralov, Z. Blum, J. Sotres, D. B. Suyatin, T. Ruzgas, T. Arnebrant, S. Shleev, *Biosensors and Bioelectronics* **2012,** *37*, 38-45.
104. T. Miyake, M. Oike, S. Yoshino, Y. Yatagawa, K. Haneda, H. Kaji, M. Nishizawa, *Chem. Phys. Letters* **2009,** *480* (1-3), 123-126.
105. B. Chandra, J. T. Kace, Y. Sun, S. Calabrese Barton, J. Hone, *Proceedings of 2nd Energy Nanotechnology International Conference* **2007,** *ENIC2007*, 1-3.
106. Y. Yan, W. Yan, W. Zheng, L. Su, L. Mao, *Advanced Materials* **2006,** *18* (19), 2639-2643.

107. P. P. Joshi, S. A. Merchant, Y. Wang, D. W. Schmidtke, *Analytical Chemistry* **2005,** *77* (3183-3188).

108. A. L. Goff, F. Moggia, N. Debou, P. Jegou, V. Artero, *Journal of Analytical Electroanalytical Chemistry* **2010,** *641*, 57-63.

109. R. L. D. Whitby, T. Fukuda, T. Maekawa, S. L. James, S. V. Mikhalovsky, *Carbon* **2008,** *46*, 949-956.

110. D. Wang, P. Song, C. Liu, W. Wu, S. Fan, *Nanotechnology* **2008,** *19*, 1-6.

111. S. C. Barton, H. H. Kim, G. Binyamin, Y. Zhang, A. Heller, *Journal of the American Chemical Society* **2001,** *123*, 5802-5803.

112. Dai, H., *Accounts of Chemical Research* **2002,** *35*, 1035-1044.

113. H. Dai, J. Kong, C. Zhou, N. Franklin, T. Tombler, A. Cassell, S. Fan, M. Chapline, *Journal of Physical Chemistry B* **1999,** *103* (51), 11246-11255.

114. H. Seunghun, S. Myung, *Nature Nanotech.* **2007,** *2*, 207-208.

115. Toray Industries, I., *Toray Carbon Fiber Paper. Specifications "TPG-H"*.

116. B. D. Ratner, A. S. Hoffman, F. J. Schoen, J. E. Lemons, *An Introduction to Materials in Medicine* **2004,** *Elsevier, Sna Diego*.

117. S. Mendez, E. M. Fenton, G. R. Gallegos, D. N. Petsev, S. S. Sibbett, H. A. Stone, Y, Zhang,G. P. Lopez, *Langmuir* **2010,** *26*, 1380.

118. E. M. Benner, D.N. Petsev, *Phys. Review E* **2013,** *87* (033008), 1-10.

119. C. W. Narváez Villarrubia, C. Lau, G. P.M.K. Ciniciato, S. O. Garcia, S. S. Sibbett, D. N. Petsev, S. Babanova, G. Gupta, P. Atanassov, *Electrochem.Comm.* **2014,** *45*, 44-47.

120. G.P.M.K. Ciniciato , C. Lau, A. Cochrane , S.S. Sibbett , E.R. Gonzalez , P. Atanassov, *Electroc. Acta* **2012,** *82*, 208-213.

121. P. Atanassov, C. Lau, C. W. Narváez Villarrubia, G. Ciniciato, S. O. Garcia, R. Rincón, S. Sibbett, D. Petsev, S. Minteer, M. Moehlenbrock, R. Arechederra, S. Banta, Y. H. Kim, E. Campbell, H.Luckarift, G. Johnson, *221st ECS Meeting, The Electrochemical Society* **2012,** *Abstract #1452*.

122. M.X. Chu, T. Shirai, D. Takahashi, T. Arakawa, H. Kudo, K. Sano, S-I. Sawada, K. Yano, Y. Iwasaki, K. Akiyoshi, M. Mochizuki, K. Mitsubayashi, *Biomed Microdevices* **2011,** *13*, 603-611.

123. E.R. Berman, *Biochemistry on the eye,* pp 476, Plenum Press, New York, 1991.
124. H. Yao, C. Marcheselli, A. Afanasiev, I. Lähdesmäki, and B.A. Parviz , *MEMS 2012, Paris, FRANCE, 29 January - 2 February* **2012,** (769-772).
125. P. Atanassov, C. Apblett, S. Banta, S. Brozik, S. C. Barton, M. Cooney, B. Y. Liaw, S. Mukerjee, S. D. Minteer, *Electrochem. Soc. Interface* **2007,** *16* (2), 28-31.
126. S. C. Barton, J. Gallaway, P. Atanassov, *Chem. Rev.* **2004,** *104* (10), 4867-4886.
127. D. Ivnitski, B. Branch, P. Atanassov, C. Apblett, *Electrochem. Commun.* **2006,** *8* (8), 1204-1210.
128. T. Sugiyama, Y. Goto, R. Matsumoto, H. Sakai, Y. Tokita, T. Hatazawa, *Biosen. and Bioelec.* **2010,** *26*, 452-457.
129. Z. Wang, M. Etienne, V. Urbanova, G.-W. Kohring, A. Walcarius, *Anal. Bioanal. Chem.* **2013,** *405*, 3899-3906.
130. H. Zheng, J. Zhou, J. Zhang, R. Huang, H. Jia, S.-I. Suye, *Microchim Acta* **2009,** *165*, 109-115.
131. Z. Wang, F. Quiles, G.-W. Kohring, A. Walcarius, *Biosens. and Bioelect.* **2012,** *32* (1), 111-117.
132. C. W. Narváez Villarrubia, R. A. Rincón, V. K. Radhakrishnan, V. Davis, P. Atanassov, *ACS App. Mater. Interfaces* **2011,** *3*, 2402-2409.
133. C. W. Narváez Villarrubia, S. O. Garcia, C. Lau, P. Atanassov, *ECS J. Sol. State Sci. and Tech.* **2013,** *2* (10), M3156-M3159.
134. M. Montagné, J.-L. Marty, *Analyt. Chim. Acta* **1995,** *315* (3), 297-302.
135. S-I. Suye, H. Zheng, H. Okada, T. Hori, *Sens. Actuat B-Chem.* **2005,** *108* (1-2), 671-675.
136. K. K.W. Maka, U. W Wollenbergerb, F. W. Schellerb, R. Renneberga, *Biosen. and Bioelect.* **2003,** *18* (9), 1095-1100.
137. M. Zhang, C. Mullens, W. Gorski, *Anal. Chem.* **2007,** *79* (6), 2446-2450.
138. B. L. Hassler, N. Kohli, J. G. Zeikus, I. Lee, and R. M. Worden, *Langmuir* **2007,** *23*, 7127-7133.
139. D. Ivnitski, K. Artyushkova, *Bioelectrochemistry* **2008** *74*, 101-110.
140. G. Gupta, C. L., V. Rajendran, F. Colon, B. Branch, D. Ivnitski, P. Atanassov, *Electrochemistry Communications* **2011,** *13*, 247-249.

141. S. Brocato, C. Lau, P. Atanassov, *Electrochimica Acta* **2012,** *61*, 44-49.

142. R. P. Ramasamy, H. R. Luckarift, D. M. Ivnitski, P. B. Atanassov, G. R. Johnson, *Chemical Communications* **2010,** *46*, 6045-6047.

143. H. Warner, B. W. Robinson, *Digest of the Seventh International Conference on Medical and Biological Engineering*. Stockholm, Sweden, 1967; p 520.

144. W. Gellett, J. Schumacher, M. Kesmez, D. Le, S. D. Minteer, *J. Elec. Soc.* **2010,** *157* (4), B557-B562.

145. K.Veena, *The anatomy and physiology of cornea*, AMC, Aug. 27, 2011. Web. Feb. 2, 2014. <http://www.authorstream.com/Presentation/vsk256-1164740-anatomy-of-cornea>.

146. L. E. Weene, *Ann Ophthalmol* **1985,** *17* (9), 521-2, 524.

147. S.D. Klyce, R.W. Beuerman Structure end Function of the cornea. In *The Cornea*.2nd ed; H.E. Kaufman, B. A. Baron, M. B. McDonald (Eds.), Butterworth-Heinemann: Boston,**1998**; p 3-50.

148. K. Inoue, S. Kato, C. Ohara,J. Numaga, S. Amano,T. Oshika, *Cornea* **2001** *20* (8), 798-801.

149. J. Kopecek, *J. Polym. Sci.Part A:Polym. Chem* **2009,** *47*, 5929-5946.

150. C. Lau, M. J. Cooney, P. Atanassov, *Langmuir* **2008,** *24* (13), 7004-7010.

151. M.J. Cooney, M. Windmesier, C. Lau, B. Y. Liaw, T. Klotzbach, S. Minteer., *J.Mater Chem* **2008,** *6*, 667-674.

152. M.X. Chu, T. Shirai, D. Takahashi, T. Arakawa, H. Kudo, K. Sano, S-I. Sawada, K. Yano, Y. Iwasaki, K. Akiyoshi, M. Mochizuki, K. Mitsubayashi, *Biomed Microdevices* **2011,** *13*, 603-611.

153. H. Yao, C. Marcheselli, A. Afanasiev, I. Lähdesmäki, and B.A. Parviz . , *MEMS 2012, Paris, FRANCE, 29 January - 2 February* **2012,** (769-772).

154. M. X. Chu, K. Miyajima, D. Takahashi, T. Arakawa, K. Sano, S.-i. Sawada, H. Kudo, Y. Iwasaki, K. Akiyoshi, M. Mochizuki and K. Mitsubayashi, *Talanta* **2011,** *83*, 960-965.

155. M. X. Chu, T. Shirai, D. Takahashi, T. Arakawa, H. Kudo, K. Sano, S.-i. Sawada, K. Yano, Y. Iwasaki, K. Akiyoshi, M. Mochizuki and K. Mitsubayashi, *Biomed. Microdevices* **2011,** *13*, 603-6011.

156. C. W. Narváez Villarrubia, R.A. Rincón, V.K. Radhakrishnan, V. Davis, P. Atanassov, *ACS Appl. Mater. Interfaces* **2011,** *3* (7), 2402-2409.
157. Y. Yan, W. Zheng, L. Su, L. Mao, *Adv. Mater.* **2006,** *18* (19), 2639-2643.
158. P. P. Joshi, S. A. Merchant, Y. Wang, D. W. Schmidtke, *Anal. Chem.* **2005,** *77* (10), 3183-3188.
159. A. L. Goff, F. Moggia, N. Debou, P. Jegou, V. Artero, M. Fontecave, B. Jousselme, S. Palacin, *J. Electroanal. Chem.* **2010,** *641* (1-2), 57-63.
160. A. Guiseppi-Elie, C. Lei, R. H. Baughman, *Nanotechnology* **2002,** *13* (5), 559-564.
161. R. L. D.Whitby, T. Fukuda, T. Maekawa, S. L. James, S. V. Mikhalovsky, *Carbon* **2008,** *46* (6), 949-956.
162. D. Wang, P. Song, C. Liu, W. Wu, S. Fan, *Nanotechnology* **2008,** *19* (7), 1-6.
163. D. Ivnitski, K. Artyushkova, R. A. Rincon, P. Atanassov, H. R. Luckarift, G. R. Johnson, *Small* **2008,** *4* (3), 357-364.
164. S. C. Barton, H. H. Kim, G. Binyamin, Y. Zhang, A. Heller, *J. Am. Chem. Soc.* **2001,** *123* (24), 5802-5803.
165. N. Mano, F. Mao, W. Shin,T. Chen, A. Heller, *Chemical Comunications* **2003,** (4), 518-519.
166. Y-M. Yan, O. Y., I. Willner, *Chem. Eur. J.* **2007,** *13* (36), 10168-10175.
167. R. C. Reid, F. G., S. D. Minteer, and B. K. Galea, *J. Electrochem. Soc.* **2013,** *160* (9), H612.
168. K. Fisher, E. W., P. P. Laenen, M. Collins *Battery Waste Management Life Cycle Assessment*; Environmental Resources Management, DEFRA: 2006.
169. Scott Calabrese Barton, P. A., *Preprint Papers - American Chemical Society, Division of Fuel Chemistry* **2004,** *49* (2), 476.
170. Frank Davis, S. e. P. J. H., *Biosensors and Bioelectronics* **2007,** *22*, 224-1235.
171. M. Togo, Y. Yehezkeli, M. Oike, H. Kaji, T. Abe, M. Nishizawa, *Proceedings of PowerMEMS 2008+ microEMS 2008.* **2008,** *Sendai, Japan* (November 9-12).
172. V. Coman, R. Ludwig, W. Harreither, D. Haltrich, L. Gorton, T. Ruzgas, S. Shleev, *Fuel Cells* **2010,** *10* (1), 9-16.
173. P. K. Addo, R. L. Arechederra, S. D. Minteer, *Electroanalysis* **2010,** *22* (807-812).

174. T. Miyake, K. Haneda, N. Nagai, Y. Yatagawa, H. Onami, S. Yoshino, T. Abec, M. Nishizawa, *Energy and Environmental Science* **2011,** *4*, 5008-5012.
175. D. Bhatnagar, S. Xu, C. Fischer, R. L. Arechederra, S. D. Minteer, *Physical Chemistry Chemical Physics* **2011,** *13*, 86-92.
176. K. Artyushkova, P. Atanassov, *Chemphyschem* **2013,** *14* (10), 2071-2080.
177. M. Bogner, M. Schnaithmann, J. Saegebarth, H. Sandmaier, *Publication in Conference paper: Proceedings of PowerMEMS 2008+ microEMS2008, Sendai, Japan, November 9-12, (2008)* **2011,** *2* (4), 357-360.
178. P. Tonda-Mikiela, A. Habrioux, S. Boland, K. Servat, S. Tingry, P. Kavanagh, T. W. Napporn, D. Leech, K. B. Kokoh, *Electrocatalysis* **2011,** *2* (4), 268-272.
179. G. Gupta, S. B. Rathod, K. W. Staggs, L.K. Ista, K. A. Oucherif, P. Atanassov, M. S. Tartis, G. A. Montaño, G. P. López, *Langmuir* **2009,** *25*, 13322.
180. V. Svoboda, C. Lau, P. Atanassov, S. Singhal, Abstract#394, *217th ECS Meeting* **2009**.
181. S. Calabrese Barton, Y. Sun, B. Chandra, S. White, J. Hone, *Electrochemical and Solid-State Letters* **2007,** *10* (5), B96-B100.
182. M. Kumar, Y. Ando, *Journal of Nanoscience and Nanotechnology* **2010,** *10* (6), 3739-3758.
183. B. Kim, H. Chung, W. Kim, *Journal of Physical Chemistry C* **2010,** *114* (35), 15223-15227.
184. D. Grujicic, B. Pesic, *Electrochimica Acta* **2006,** *51* (13), 2678-2690.
185. C. J. Brinker, *Journal of Non-Crystalline Solids* **1988,** *100*, 31-50.
186. H. Bornschein, O. Wichterle, L. Wundsch, *Vision Res.* **1966,** *6*, 733-734.
187. A. Ludwig, *Adv. Drug. Deliv. Rev.* **2005,** *57*, 1595-1639.
188. H. Yao, Y. Liao, A. R. Lingley, A. A. Afanasiev, I. Lahdesmaki, B. P. Otis and B. A. Parviz, *J. Micromech. Microeng.* **2012,** *22*, 1-10.
189. N. Thomas, I. Lahdesmaki, B. A. Parviz, *NEMS 2012* **2012**, 398-402.
190. A. Zebda, S. Cosnier, J.-P. Alcaraz, M. Holzinger, A. Le Goff, C. Gondran, F. Boucher, F. Giroud, K. Gorgy, H. Lamraoui, P. Cinquin, *Scientific Reports* **2013,** *3*, 1-5.
191. J. M. H. Dirk, H. S. van der Baan, *Journal of Catalysis* **1981,** *67* (1), 1-13.

192. L. Halámková, J. Halámek, V. Bocharova, A. Szczupak, L. Alfonta, E. Katz *Journal of Chemical Society* **2012,** *134*, 5040-5043.
193. P. Malachesky, G. Holleck, F. McGovern, R. Devarakonda, *Proceedings of the Seventh Intersociety Energy Conversion Engineering Conference* **1972**, 727-732.
194. R. F. Drake, B. K. Kusserov, S. Messinger, S. Matsuda, *Transaction of American Society for Artificial Internal Organs* **1970,** *16*, 199-205.
195. J. E. Poole, M. J. Gleva, T. Mela, M. K. Chung, D. Z. Uslan, R. Borge, V. Gottipaty, T. Shinn, D. Dan, L. A. Feldman, H. Seide, S. A. Winston, J. J. Gallagher, J.J. Langberg, K. Mitchell, R. Holcomb, *Circulation* **2010**, 1553-1561.
196. A. Szczupak, J. Halámek, L. Halámková, V. Bocharova, L. Alfonta, E. Katz, *Energy and Environmental Science* **2012,** *5*, 8891-8895.
197. J.O'M. Bockris, B. J. Piersma, E. Gileadi, *Electrochimica Acta* **1964,** *9* (10), 1329-1332.
198. S. K. Wolfson, S. L. Gofberg, P. Prusiner, L. Nanis, *Transanctions- American Society for Artificial Internal Organs* **1968,** *14*, 198-203.
199. S.K. Wolfson, S. J. Yao, A. Geisel, H.R. Cash, *Transactions - American Society for Artificial Internal Organs* **1970,** *16*, 193-198.
200. M.E. Talaat, J. H. Kraft, R.A. Cowley, A.H. Khazei, *IEEE Transactions on Biomedical Engineering* **1967,** *14* (4), 263-265.
201. P. Malachesky, G. Holleck, F. McGovern, R. Devarakonda, *Proc. 7th Intersoc.Energy Convers. Eng. Conf. 1972*, 727-732.
202. E. Weidlich, G. Richter, F. Von Sturm, J. R. Rao, A. Thoren, H. Lagergren, *Biomater. Med. Devices Artif. Organs 1976 4*, 277-306.
203. A. C. Guyton, J. E. Hall, *Textbook of Medical Physiology,* Elsevier Saunders: Philadelphia, 2006.
204. M. Shao, M. Nadeem Zafar, C. Sygmund, D. A. Guschin, R. Ludwig, C. K. Peterbauer, W. Schuhmann, L. Gorton, *Biosens. Bioelectron.* **2013,** *40*, 308 -314.